STARS

University of Central Florida
STARS

Electronic Theses and Dissertations, 2020-

2020

Rotational and Shower Head Cooling Hole Effects on Leading-Edge Jet Impingement Heat Transfer

Weston Olson
University of Central Florida

Part of the Heat Transfer, Combustion Commons

Find similar works at: https://stars.library.ucf.edu/etd2020

University of Central Florida Libraries http://library.ucf.edu

This Masters Thesis (Open Access) is brought to you for free and open access by STARS. It has been accepted for inclusion in Electronic Theses and Dissertations, 2020- by an authorized administrator of STARS. For more information, please contact STARS@ucf.edu.

STARS Citation

Olson, Weston, "Rotational and Shower Head Cooling Hole Effects on Leading-Edge Jet Impingement Heat Transfer" (2020). *Electronic Theses and Dissertations, 2020-*. 111.
https://stars.library.ucf.edu/etd2020/111

Showcase of Text, Archives, Research & Scholarship

ROTATIONAL AND SHOWER HEAD COOLING HOLE EFFECTS ON
LEADING-EDGE JET IMPINGEMENT HEAT TRANSFER

by

WESTON OLSON
B.S.M.E. Department of Mechanical and Aerospace Engineering, 2010

A thesis submitted in partial fulfillment of the requirements
for the degree of Master of Science in the
Department of Mechanical and Aerospace Engineering
in the College of Engineering and Computer Science
at the University of Central Florida
Orlando, Florida

Spring Term
2020

ABSTRACT

Jet Impingement and shower head cooling are critical cooling techniques used to maintain turbine blades at operational temperatures. Jet impingement is extremely effective at removing large amounts of heat flux from the target surface, the inner blade wall, through stagnation point heat transfer. Shower head cooling produces a cooling film around the exterior of the blade, in return reducing external heat flux.

The current work consisted of investigating the jet impingement effectiveness with rotational effects for two different cooling schemes. The analysis was conducted numerically using STAR CCM+ with two different turbulence models, the three equation Lag Elliptic Blending K Epsilon model and the seven equation Elliptic Blending Reynolds Stress Transport (EB RST) model. The EB RST model incorporated the Generalized Gradient Diffusion method. The blade used was NASA/General Electrics E^3 row 1 blade. Two conjugate heat transfer models were developed for just the leading-edge portion of the blade, one with and one without shower head holes. The models consisted of a quarter of the blade-span to reduce computational expense and only one jet was analyzed.

A flow field analysis was performed on the free jet region to analyze the potential core velocity and turbulent kinetic energy profiles. Nusselt Number spanwise distribution and external blade temperature profiles were also evaluated. The investigation showed, for both turbulence models, that rotational effects produce turbulent kinetic energy within the jet's potential core, reducing the incoming jet velocity and hence reducing impingement effectiveness. While both

turbulence models illustrated an increase in turbulent kinetic energy throughout the structure of the impinging jet, the magnitudes and locations varied significantly. This is due to the well-known underprediction of turbulent dissipation in the K-Epsilon family of turbulence models, as well as the location of applications of the vorticity tensor to the transport equations.

ACKNOWLEDGMENTS

I would like to thank Dr. Jose Rodriguez, Dr. Samik Bhattacharya, Dr. Erik Fernandez and Dr. Jayanta Kapat. Dr. Rodriguez helped me establish the meshing scheme which produced optimal Wall Y+ values. Dr. Bhattacharya assisted with providing knowledge of turbulent theory. Dr. Fernandez aided in the procedure required to post process the EB RST solution. He also assisted with the manner and order of presenting the data for the case studies. Dr. Kapat provided guidance in the direction, and the details which required attention, of the investigation. He also provided support in analyzing and interpreting the results of the study.

TABLE OF CONTENTS

LIST OF FIGURES

LIST OF TABLES

NOMENCLATURE

$z \ (mm)$ – Nozzle to Target Distance

$d \ (mm)$ – Nozzle Diameter

$x \ (mm)$ – Nozzle to Nozzle Spanwise Pitch

$h \ (mm)$ – Distance from Nozzle Exit

$\nu \ (m^2/s)$ – Molecular Kinematic Viscosity

$\nu_t \ (m^2/s)$ – Turbulent Kinematic Viscosity

$\rho \ (kg/m^3)$ – Density

$\vec{g} \ (m/s^2)$ – Acceleration of Gravity

$P \ (N/m^2)$ – Pressure

$\mu \ (kg \cdot m/s)$ – Dynamic Viscosity

$\vec{V} \ (m/s)$ – Relative Velocity

$\vec{V}_{imp} \ (m/s)$ – Relative Impingement Velocity

$\Omega \ (rad/s)$ – Rotational Velocity

$\vec{r} \ (m)$ – Radius from Engine Centerline

$b \ (mm)$ – Grid Size (Base Size for Surface and Volume Meshers)

rf – Refinement Factor

ϕ – Critical Variable

p – Apparent Order

ϕ_{ext} – Extrapolated Critical Variable

e_a – Approximate Relative Error

e_{ext} – Extrapolated Relative Error

GCI – Grid Convergence Index

CHAPTER – 1: INTRODUCTION

Jet impingement heat transfer has been thoroughly studied for its ability to transfer relatively large amounts of heat. Several different aspects to jet impingement cooling are critical for designing the most effective cooling scheme. For leading-edge turbine blades these aspects include impingement surface distance to jet diameter ratios, crossflow effects on stagnation point heat transfer, rotational effects on impingement heat transfer, impingement on curved surfaces, impingement onto textured surfaces, and the interaction of jet impingement with shower head cooling holes.

The structure of an impinging jet consists of three main regions. These regions are the free jet region, the stagnation region and the wall jet region, Figure 1. The free jet region is composed of a potential core with a uniform velocity profile which is encompassed by a turbulent shear layer. The shear layer is created by the exchange of momentum between the potential core and the surrounding stagnant fluid. As the jet travels in the axial direction of the nozzle, the exchange in momentum continues and the shear layer grows linearly and simultaneously the potential core shrinks. The stagnation region is where the majority of heat transfer takes place. Heat transfer coefficient is inversely proportional to boundary layer thickness. Therefore, the smaller the boundary layer the greater the heat transfer. In the stagnation region the vertical acceleration is transformed into a horizontal acceleration which creates the wall jets. The wall jets consist of a boundary layer over the wall and a shear layer between the boundary layer's maximum velocity and the stagnant fluid surrounding it. Martin

[1] investigated the hydrodynamics at these three regions. Some of the conclusions that Martin [1] found from the study were that potential core length is around four jet diameters and stagnation boundary layer thickness is around one-hundredth of the jet diameter.
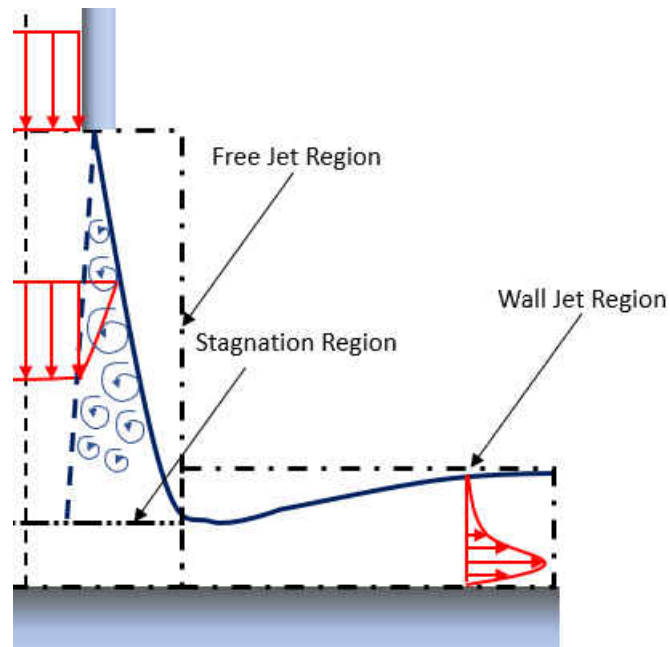
Figure 1: Impinging Jet Structure

Goldstein et al. [1] studied the local heat transfer coefficient of a circular impinging jet with varying impingement plate spacing to jet diameter ratios. The study concluded that maximum stagnation point heat transfer occurred at an impingement plate spacing to jet diameter ratio of 8. Florschuetz and Metzger [2] investigated an array of impinging jets with crossflow. The results of the investigation showed that for a fixed jet Reynolds number and geometric parameters, an increase in the ratio of crossflow mass flux to jet flow mass flux resulted in a monotonically decrease in heat transfer coefficient.

Lamont et al. [3] researched the effects of rotation on heat transfer for a row of impinging jets with crossflow. The study revealed that the Coriolis force may influence the developing length of jet potential core. Iacovides et al. [4] experimentally studied the flow and thermal development of a row of impinging jets on a rotating concave surface. The experiment illustrated that under rotation the primary heat transfer peaks, stagnation points, are reduced and the secondary heat transfer peaks, interaction between wall jets, are diminished. Chiang and Li [5] investigated jet impingement and forced convection in rotating turbine blades. They also concluded that under rotation stagnation point heat transfer decreases, but this effect could be counter-acted by increasing the jet Reynolds number. Mattern and Hennecke [6] studied the effects of impingement axis angle with axis of rotation. The conclusion to their investigation was that Coriolis forces mostly impacted parallel and perpendicular axes, while a $45°$ angle was least affected. Gau and Lee [7] performed investigations for impingement on rib roughened surfaces. Their analysis showed that with proper control over geometry, a 100% increase in heat flux can be achieved.

Yang et al. [8] studied the effect of film cooling arrangement for impingement on a leading-edge. The study consisted of varying the array angle and spanwise location of film cooling holes. The investigation showed that heat transfer decreased for an increase in array angle and that heat transfer was maximized when jet axis was located at the midpoint distance between two spanwise adjacent film holes. Taslim and Khanicheh [9] performed investigations on leading-edge impingement with and without shower head and gill film holes. The study

revealed that heat transfer coefficients were higher for the cases with showerhead holes, in comparison to the ones without.

Studies on the turbulent shear layer encompassing the potential core of turbulent free jets are also important for aspects regarding jet spread and potential core length. An investigation conducted by Hussain [10] studied coherent structures and the toroidal vortex breakdown into smaller scale motions, in return increasing turbulence intensity. Winant and Broward [11] investigated the growth of turbulent mixing layers and vortex pairing. The study found that turbulent vortices interact with one another by rolling up and forming larger structures, resulting in a growth of turbulent mixing layer.

There has also been an extensive amount of studies conducted on the numerical calculations used to predict turbulent flow. The numerical models of turbulence can be classified under two categories which are the Scale Resolving Simulations and the Reynolds Average Navier-Stokes (RANS) turbulence models. In STAR-CCM+ the Scale Resolving Simulations are composed of Large Eddy Simulations (LES) and Detached Eddy Simulations.

The RANS turbulence models consist of Eddy Viscosity Models and Reynolds Stress Transport Models. The most popular Eddy Viscosity Models are two equation models which are the K-Epsilon and the K-Omega turbulence models. The Reynolds Stress Transport Models consist of the Linear Pressure-Strain, Quadratic Pressure-Strain and the Elliptic Blending Models. The current study consisted of one model from each type of the RANS turbulence models.

The Eddy Viscosity Model used was the three equation Lag EB K-Epsilon turbulence model. The model incorporates the turbulent kinetic energy and turbulent dissipation rate

transport equations derived by Billard and Laurence [12] in combination with the stress-strain lag concept developed by Revell et al. [13]. Additional terms are embedded within the reduced stress function of the model to capture the effects of anisotropy. These terms also serve to capture the effects of rotation. The reduced stress function was developed by Lardeau and Billard [14]

The Reynolds Stress Transport Model used was the Elliptic Blending Reynolds Stress Model. The Elliptic Blending model used was developed by Lardeau and Manceau [15]. The model uses a blending factor which blends the pressure-strain term from the viscous sub-layer to the log layer. The Reynolds Stress Model used also incorporated the Generalized Gradient Diffusion Method developed by Daly and Harlow [16]. The Generalized Gradient Diffusion Method is known as the Anisotropic Eddy-Diffusivity model and points to the fact that heat transfer is produced by anisotropic thermal diffusion.

In the present study the focus will primarily be on the effects that rotation play on impingement heat transfer and on the development of the jets potential core. The investigation is comprised of eight case studies consisting of two cooling schemes, one with and another without shower head holes, for both turbulence models on stationary and rotating reference frames. For each case study the flow field analysis was composed of a spanwise cross-section and five axial jet cross-sections in increments of one-sixth of nozzle exit to target surface. The axial jet cross-sections were used to analyze the potential core velocity profile of the jet, as well as the turbulent shear layer encompassing the potential core.

The heat transfer analysis consisted of Nusselt Number contour plots and spanwise distributions through maximum Nusselt Number values. Because of the geometry of the system, the acute inlet angle of the shower head holes will produce highly anisotropic turbulent values. These anisotropic values will result in inaccurate calculations. For this reason, the impingement section analyzed was set just inside the inlets of the shower head holes. The external blade temperature analysis consisted of temperature profiles. It is expected that the model with shower head holes will have a significantly less external blade temperature, regardless of impingement effectiveness, due to film cooling.

The geometry of the model and boundary conditions for conjugate heat transfer model were defined by values given by Timko [17] and Halila et al. [18]. There was a grid study on the uncertainty due to discretization for both meshes, of each turbulence model, by a procedure established by Celik, I.B. et al. [19].

CHAPTER – 2: CAD AND CONJUGATE HEAT TRANSFER MODELS

CAD Models

The CAD geometry was developed through details given by Timko [17] and Halila et al. [18]. The shower head hole diameters and outer airfoil geometry were given by Timko [17]. The cooling components were stated by Halila et al. [18]. The details were given for number of impinging jets (12), number of shower head hole rows (10) and the angle with respect to the radial vector (25°) for shower head holes. No dimensions were given for impinging jet or any internal cooling channels. Therefore, these dimensions were assumed with a nozzle to target distance of $z = 2.54\ mm$ and a nozzle diameter of $d = 0.635\ mm$. The CAD model also had an equivalent spanwise pitch for impinging jets and shower head cooling holes. This was done for the purpose of obtaining a symmetrical analysis of the effects of the pressure gradient induced by the application of shower head holes. The nozzle to nozzle spanwise pitch was $x = 3.28\ mm$. The midspan radius of the models was located halfway between the top and center nozzles. The midspan radius for the E^3 row 1 blade is $344.703\ mm$. The radius from engine centerline to the center nozzle axis is $343.062\ mm$. Figures 2 and 3 illustrate these dimensions with respect to the CAD model.
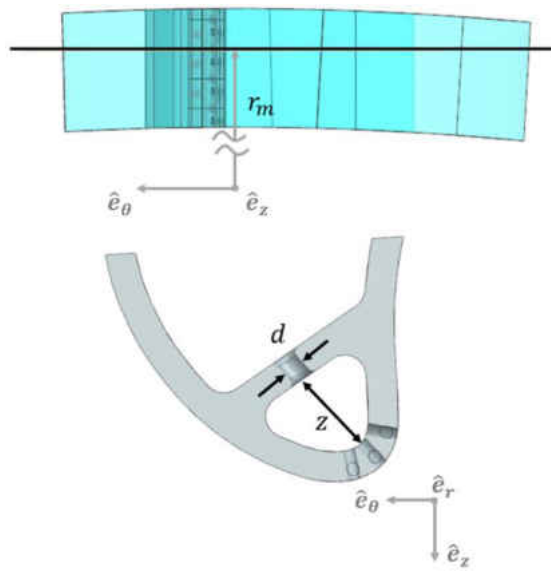
Figure 2: Geometric Dimensions for CAD
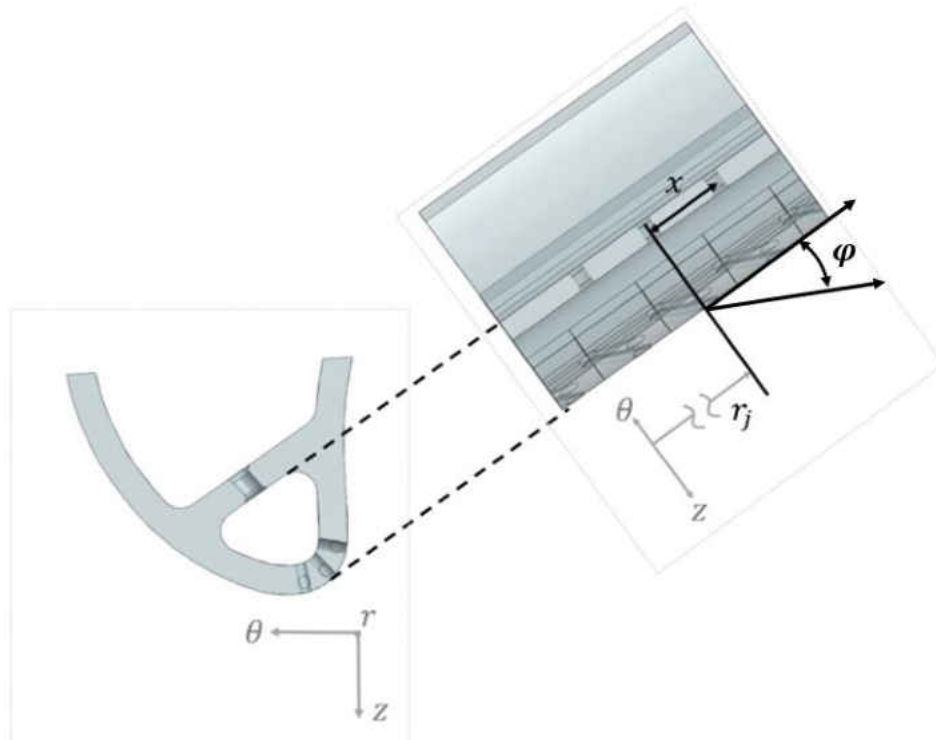
Figure 3: Geometric Dimensions for CAD

The domain for the model with shower head holes is illustrated in Figure 4. The cooling scheme consisted of three impingement nozzles with five rows of three shower head holes per row. The top and bottom row of shower head holes were split for the purpose of applying periodic contact interfaces, within the conjugate heat transfer model, at the split ends. The periodic contact interfaces were applied so that all three jets would be exposed to the pressure gradient of inner and outer shower head holes. The domain of analysis was for the middle jet only, because the inner and outer jets were exposed to unsymmetrical pressure gradients from their corresponding shower head holes. The CAD Model consists of two bodies including the geometry of the metal and that of the fluid, coolant and gas together. The purpose of the simplified model is to perform a detailed analysis of the impinging jet. The section blade span model, one-quarter of total blade span, is of constant cross-section with the assumption that the radial twist has negligible effects on heat transfer.

The no shower head hole model is illustrated in Figure 5. Because of the absence of shower head holes the model is composed of three bodies: metal, coolant and gas. Both models are identical in all aspects besides the shower head holes
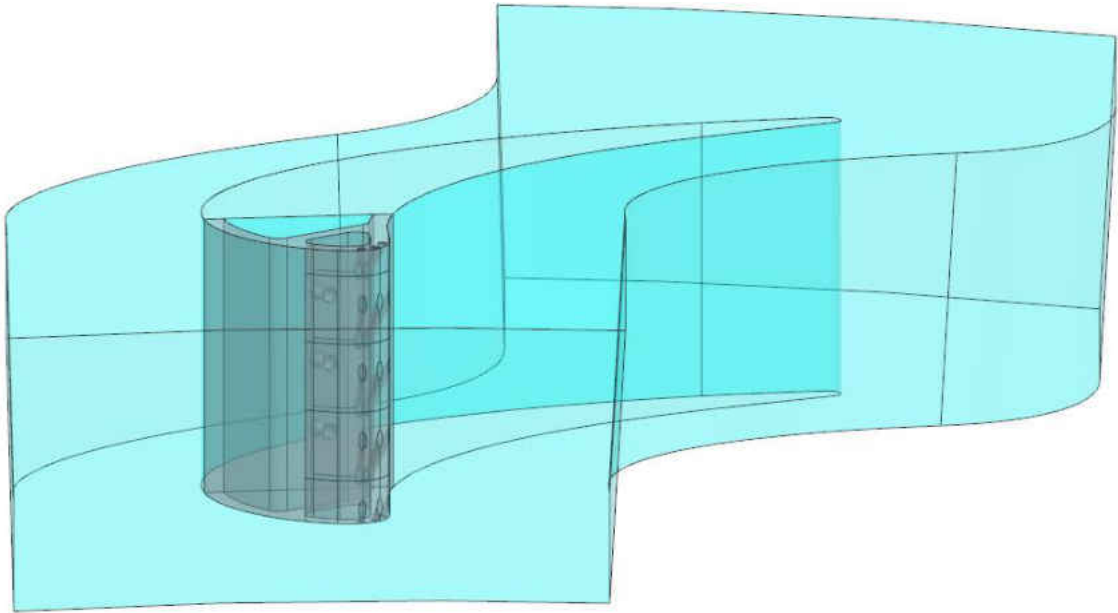
Figure 4: 2-Body CAD Model of Fluid and Metal
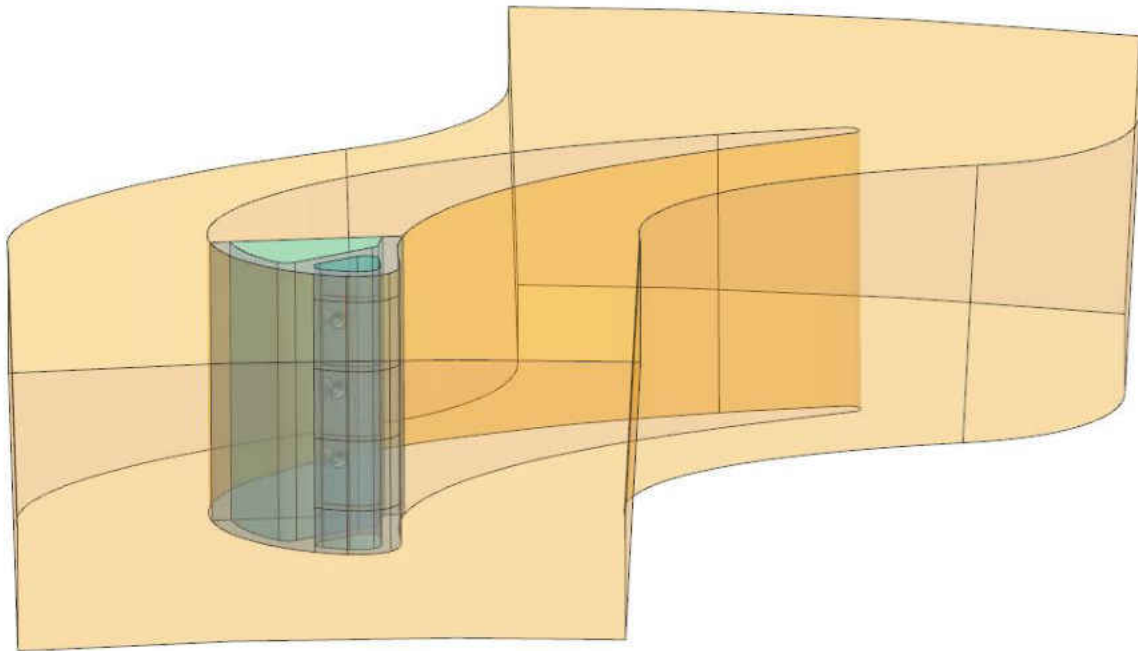
Figure 5: 3-Body CAD Model of Coolant, Gas and Metal

Conjugate Heat Transfer Models

The conjugate heat transfer models used a fine-tuned mesh to optimize Wall Y+ values for both turbulence models selected. The transport equations of each turbulence model were analyzed to explain any discrepancies in the results. The boundary conditions were derived by a calorifically perfect ideal gas analysis with Mach numbers and total properties given by Timko [16] and Halila et al. [17]. The coolant boundary conditions were assumed since full modeling of the entire cooling system was required for actual values. Periodic contact interfaces were used to create the simplified system. A procedure for convergence of the Elliptic Blending Reynolds Stress Transport model was required, which was due to the unsteadiness of the solution. A study on the grid uncertainty due to discretization was then performed for each set of meshes, corresponding to their respective turbulence model.

Mesh

In order to produce a mesh without poor quality cells at the transition from one wall thickness prism layer to the other, the fill holes extract volume procedure was used, for the shower head hole meshes. The fill holes operation consisted of the fluid body and the inlet and exit edges of the shower head holes. The extract volume operation generated eighteen volumes consisting of the coolant, metal, gas, and fifteen shower head hole channels. This procedure allows for independent control of prism layer structure over each of the volumes.

The surface mesher incorporated the enhanced quality triangle method with automatic surface repair. Custom controls were applied to impingement surface, shower head holes, and external leading-edge blade surface, as illustrated in Figure 6. The volume mesher consisted of polyhedral and advanced layer meshers. The mesh optimizers consisted of core mesh optimization and post mesh optimization. The core mesh optimizer, for the Lag EB K-Epsilon model, entailed one optimization cycle with a cell quality of 1.0. Due to the sensitivity of cell quality for the EB RST model, eight optimization cycles with a cell quality threshold of 1.0 was required. The post mesh optimizers consisted of boundary vertex optimization and cell topology optimization. The boundary vertex optimizer reduces the number of cells with small volume changes and the cell topology optimizer helps prevent formation of cells that cause the solution to diverge. Custom controls included volume controls and surface controls. Volume control was applied to the coolant supply channel, impingement channel and the jets, Figure 7. The jets were embodied by cones.

The surface controls were used to define the prism layer structure along the surfaces of each extracted volume. The coolant volume had twenty-two prism layers with wall prism layer thickness emphasis placed on the impingement and fill holes surfaces. The metal consisted of one prism layer, for conformal contact interface with the fluid volumes. The gas had fifteen prism layers with wall prism layer thickness emphasis placed on the leading-edge and fill holes surfaces. The shower head hole channels consisted of twenty prism layers with importance placed on the inner and outer holes of the middle section, along with their corresponding fill holes surfaces. Figures 8 and 9 illustrate a chordwise cross-section and spanwise cross-section of

the mesh, respectively. Figure 10 illustrates the prism layer structure for the surfaces were wall

bounded turbulence is important. Independent control over prism layer structure of the three

turbulent regions allowed for optimization of Wall Y+ values without compromising cell quality.
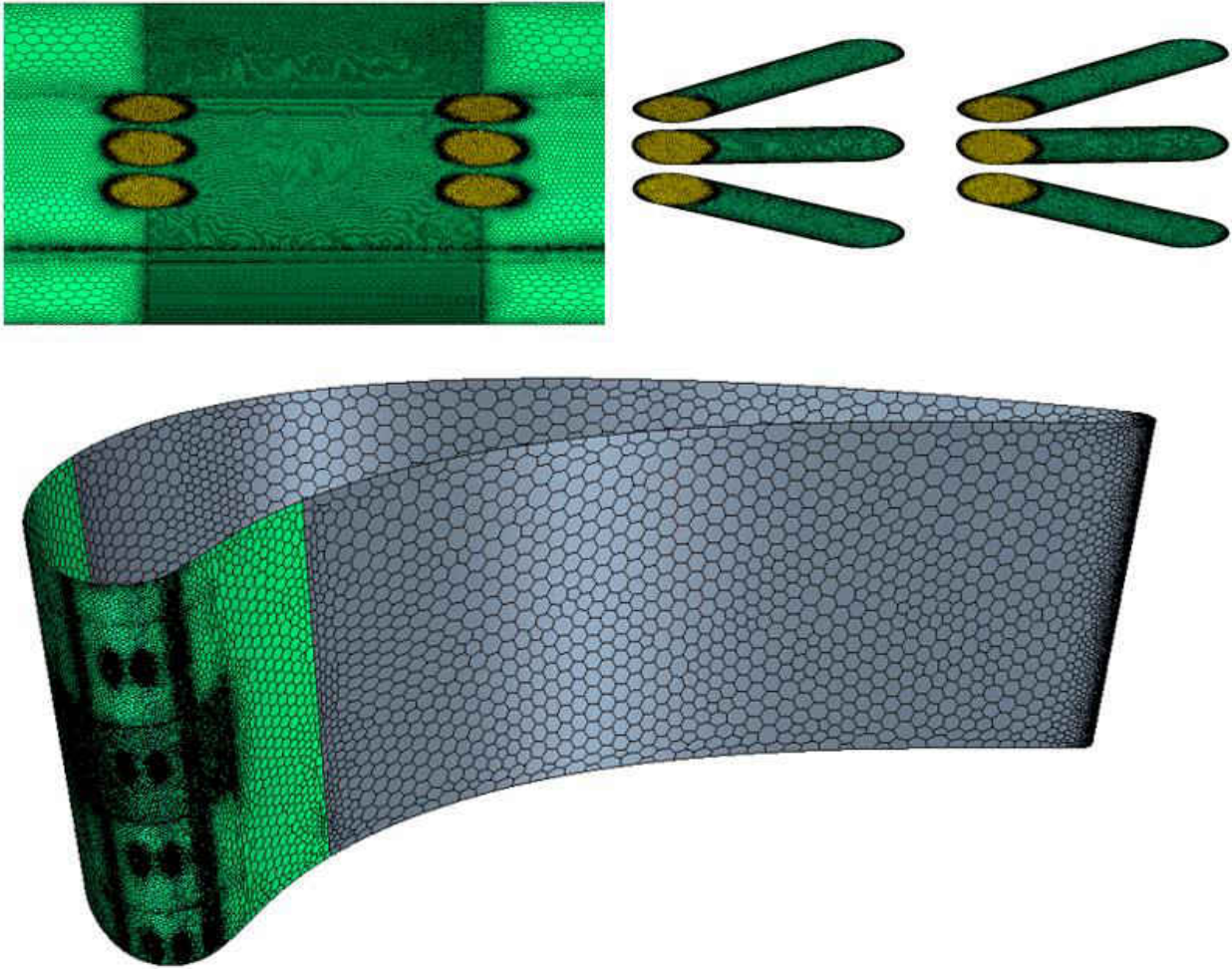
Figure 6: Surface Mesh
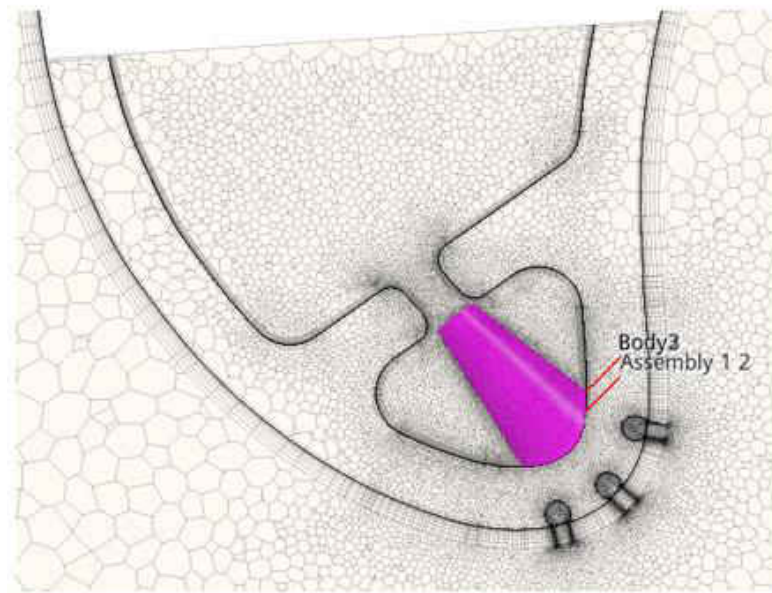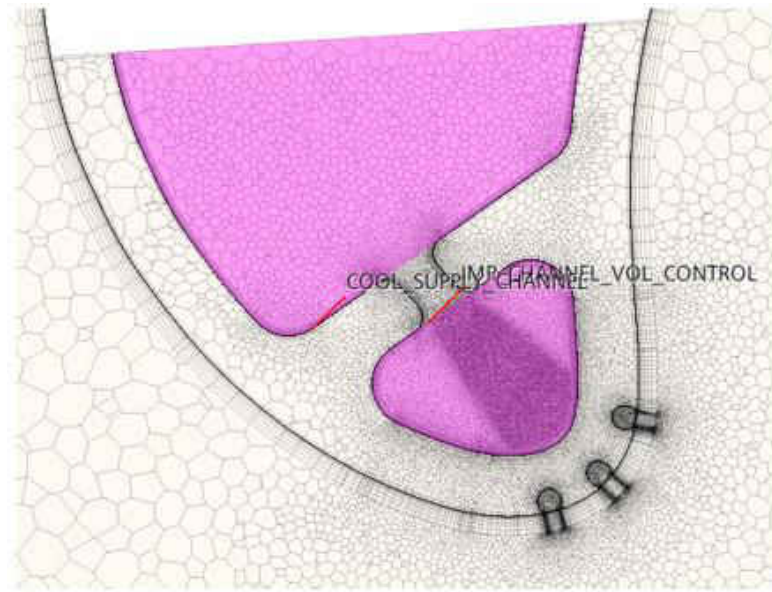
Figure 7: Custom Volume Controls
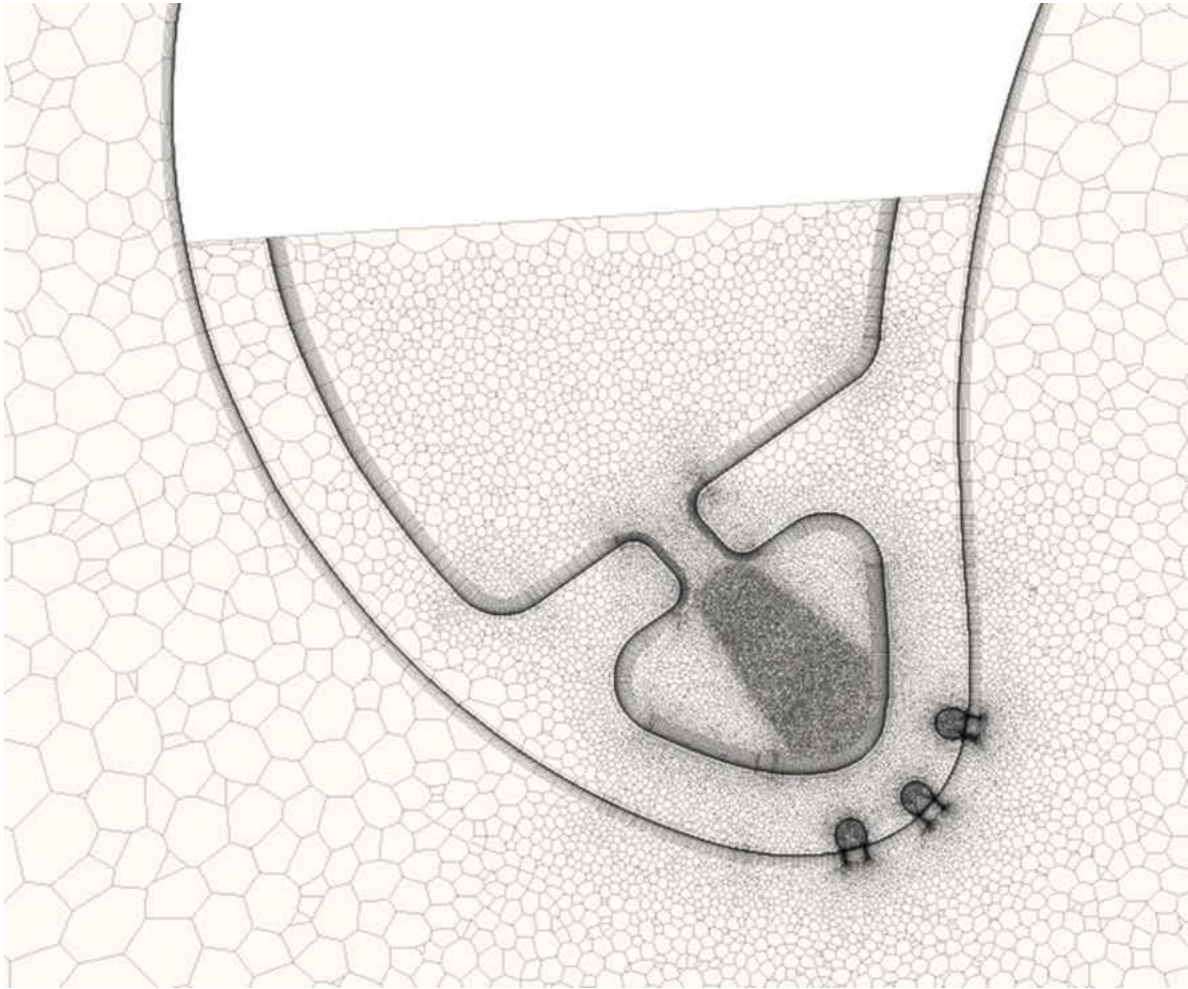
Figure 8: Chordwise Cross-Section of Mesh
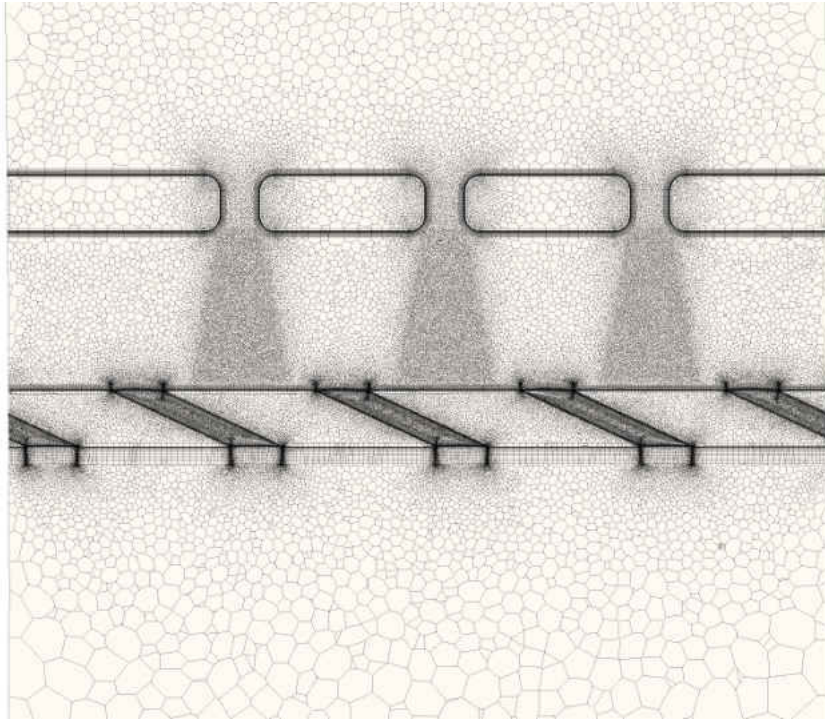
Figure 9: Spanwise Cross-Section of Mesh
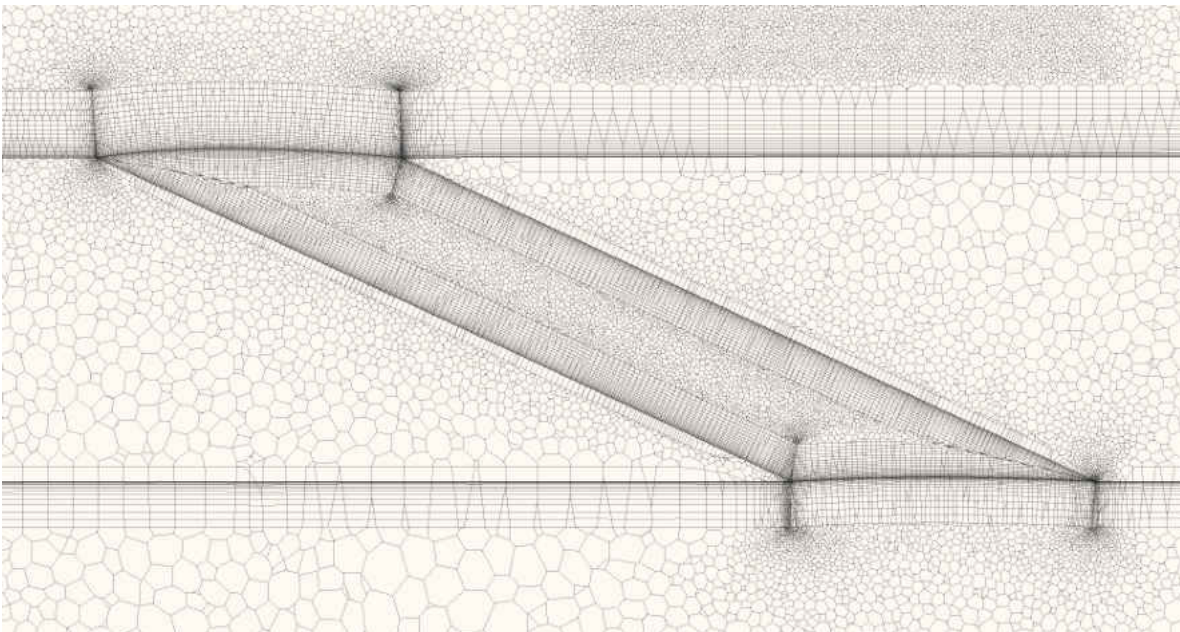
Figure 10: Prism Layer Structure for Surfaces with Important Wall Bounded Turbulence

16

Physics Continua

Physics continua were defined for the fluid and the metal. The fluid incorporated two different turbulence models, Lag EB K-Epsilon and Elliptic Blending Reynolds Stress Transport, with material properties of air. Dynamic viscosity was defined by table values as a function of temperature. Specific heat and thermal conductivity were polynomial functions of temperature. Molecular weight, standard state temperature, and turbulent Prandtl number were constant values. The reference pressure was set to $10.4\ bar$. The initial conditions were set to the conditions of the coolant which were a gauge pressure of $7\ bar$, static temperature of $870\ K$, and velocity of $0\ m/s$. The metal used material properties of Inconel 718 with density and specific heat as constants, and thermal conductivity as a polynomial function of temperature. The initial condition of static temperature was set to $750\ K$.

The Lag EB K-Epsilon model uses the traditional two transport equations for turbulent kinetic energy, turbulent dissipation rate, along with an additional transport equation for the lag between the strain rate and Reynolds Stress tensors (or alternatively the reduced stress function). The derivation of the model was based on the Elliptic Blending Reynolds Stress Transport (EB RST) model. The current turbulence model incorporates the angle between principle components of the stress and strain rate tensors. In return reducing the overprediction of turbulent kinetic energy production by linear Eddy Viscosity Models, which assume that these tensors are aligned. All the constants in the current model are directly related to the constants in the EB RST model. The model also incorporates a $y+$ all wall treatment.

The following transport equations and their terms were derived by Lardeau and Billard [14]. The complete derivation of these transport equations will not be presented here, but some key features will be discussed. The three transport equations and the blending factor, α, are given by Equations 1, 2, 3 and 4, respectively. Where k is the turbulent kinetic energy, ε is the turbulent dissipation rate, φ is the reduced stress (or alternatively the lag effect on eddy viscosity)

$$\frac{Dk}{Dt} = P - \varepsilon + \frac{\partial}{\partial x_j}\left[\left(\frac{\nu}{2} + \frac{\nu_t}{\sigma_k}\right)\frac{\partial k}{\partial x_j}\right] \tag{1}$$

$$\frac{D\varepsilon}{Dt} = C_{\varepsilon_1}\frac{P\varepsilon}{k} - E - C_{\varepsilon_2}^*\frac{\varepsilon^2}{k} + \frac{\partial}{\partial x_j}\left[\left(\frac{\nu}{2} + \frac{\nu_t}{\sigma_\varepsilon}\right)\frac{\partial \varepsilon}{\partial x_j}\right] \tag{2}$$

$$\frac{D\varphi}{Dt} = (1 - \alpha^3)f_w + \alpha^3 f_h - C_{P_1}\frac{P}{k}\varphi + \frac{\partial}{\partial x_j}\left[\left(\frac{\nu}{2} + \frac{\nu_t}{\sigma_\varphi}\right)\frac{\partial \varphi}{\partial x_j}\right] \tag{3}$$

$$L^2\nabla^2\alpha = \alpha - 1 \tag{4}$$

and the following terms are defined by:

$$E = -2C_k\nu\nu_t(1 - \alpha)^3\left(\frac{\partial\|2S_{ij}n_j\|n_k}{\partial x_k}\right)^2 \tag{5}$$

$$f_w = C_w^*\varphi\frac{\varepsilon}{k} \tag{6}$$

$$f_h = \left(\tilde{C}_1 + C_1^*\frac{P}{\varepsilon}\right)\frac{\varphi}{\tau} + C_{P_2}\varphi S + C_{P_3}\frac{1}{\tau} + \tau_s M_{ij}S_{ij} \tag{7}$$

$$M_{ij} = C_4^*a_{ij}S_{jk} + C_5^*a_{ik}W_{jk} \tag{8}$$

$$\tau_s = \frac{\tau}{max(\eta^2, 1)} \tag{9}$$

$$\tau = \sqrt{\left(\frac{k}{\varepsilon}\right)^2 + C_t \frac{\nu}{\varepsilon}} \tag{5}$$

$$L = C_L \sqrt{\left(\frac{k}{\varepsilon}\right)^3 + C_\eta^2 \sqrt{\frac{\nu^3}{\varepsilon}}} \tag{6}$$

Where P is the production, a_{ij} is the anisotropy tensor, E is the rate of deformation, S is defined as $\sqrt{2S_{ij}S_{ij}}$, W_{ij} is the vorticity tensor, L is the turbulent length scale, η is the ratio of mean velocity strain to turbulence time scales, and f_h and f_w are functions far-away-from the wall and near the wall regions, respectively. The derivation of the reduced stress transport equation, Equation 3, comes from solving the transport equation for the degree of alignment between strain and stress tensors, Equation 12, and is represented by ξ.

$$\frac{D\xi}{Dt} = -\frac{S_{ij}}{kS}\left[P_{ij} - \varepsilon_{ij} + \phi_{ij}^* - a_{ij}(P - \varepsilon)\right] - \frac{1}{S}\frac{DS_{ij}}{Dt}\left(a_{ij} + \frac{2S_{ij}\xi}{S}\right) \tag{7}$$

With the first four terms of this equation coming directly from the EB RST model. These terms are defined as:

$$P_{ij} = -k(1 - \alpha^3)\frac{4}{3}S_{ij} - k\alpha^3\left(\frac{4}{3}S_{ij} + a_{ij}S_{kj} + S_{ik}a_{kj} + a_{ik}W_{kj} + W_{ik}a_{jk}\right) \tag{8}$$

$$\varepsilon_{ij} = (1 - \alpha^3)\overline{u_\iota u_j}\frac{\varepsilon}{k} + \alpha^3\frac{2}{3}\varepsilon\delta_{ij} \tag{9}$$

$$\phi_{ij}^* = (1 - \alpha^3)C_w\varepsilon a_{ij} - \alpha^3\left(C_1 + C_1^*\frac{P}{\varepsilon}\right)\varepsilon a_{ij} + \alpha^3\left(C_3 - C_3^*\sqrt{a_{kl}a_{kl}}\right)kS_{ij}$$
$$+ \alpha^3 C_4 k\left(a_{ik}S_{jk} + a_{jk}S_{ik} - \frac{2}{3}a_{lm}S_{lm}\delta_{ij}\right) \tag{10}$$
$$+ \alpha^3 C_5 k\left(a_{ik}W_{jk} + a_{jk}W_{ik}\right)$$

19

The last term in Equation 7 is assumed zero, which will produce inaccurate calculations for flows involving curvature or rotation, therefore a correction for this assumption will be presented shortly. After making substitutions and rearranging terms, the transport equation for the reduced stress term is obtained, Equation 3. The anisotropy tensor, a_{ij}, is given by the Quadratic Constitutive Relationship, Equation 16

$$a_{ij} = -2\frac{v_t}{k}\left[S_{ij} - C_{cr_1}\left(O_{ik}S_{jk} + O_{jk}S_{ik}\right)\right] \tag{11}$$

where

$$O_{ij} = \frac{\widetilde{W}_{ij}}{\sqrt{S^2 - \widetilde{W}^2}} \tag{12}$$

with $\widetilde{W}_{ij}$ being the Absolute Vorticity tensor. The correction for the neglected term in Equation 7 comes by replacing the vorticity tensor with the absolute vorticity tensor for the calculation of the transport equations. The Absolute Vorticity tensor is given by Equation 18,

$$\widetilde{W}_{ij} = \frac{1}{2}\left(\frac{\partial U_i}{\partial x_j} - \frac{\partial U_j}{\partial x_i}\right) + \epsilon_{kij}\omega_k - W_{ij}^S \tag{13}$$

where ω_k is the rotation rate of the local reference frame and W_{ij}^S is the $Spalart - Shur$ tensor and is given by Equation 19.

$$W_{ij}^S = \frac{1}{S^2}\left(S_{ik}\frac{DS_{jk}}{Dt} - \frac{DS_{ik}}{Dt}S_{kj}\right) \tag{19}$$

The Absolute Vorticity tensor is directly applied to the reduced stress transport equation and indirectly applied to the turbulent kinetic energy and turbulent dissipation rate transport equations through iterative calculations. All other terms are coefficients and their values can be found in [14].

20

The Elliptic Blending Reynolds Stress Transport (EB RST) model solves seven transport

equations, the six Reynolds Stress transport equations and the turbulent dissipation rate

transport equation. The model blends the pressure-strain and dissipation tensors between the

viscous sub-layer and the log layer through the same elliptic blending function, α, used in the Lag

EB K-Epsilon turbulence model, Equation 4. As with the Lag EB K-Epsilon turbulence model,

complete derivation of the EB RST model will not be presented here, but some key

characteristics will be noted. Complete derivation can be found in [15]. The Reynolds Stresses

and turbulent dissipation rate transport equations are given by Equations 20 and 21,

respectively.

$$\frac{D\overline{u_i u_j}}{Dt} = P_{ij} + \phi_{ij}^* - \varepsilon_{ij} + D_{ij}^t + \frac{\partial}{\partial x_k}\left(v\frac{\partial \overline{u_i u_j}}{\partial x_k}\right) \tag{20}$$

$$\frac{D\varepsilon}{Dt} = \frac{1}{\tau}\left(C_{\varepsilon_1}P - C_{\varepsilon_2}^*\varepsilon\right) + E + D_{ij}^t + \frac{\partial}{\partial x_k}\left(v\frac{\partial \varepsilon}{\partial x_k}\right) \tag{21}$$

Where P_{ij} is the production tensor, ϕ_{ij}^* is the pressure-strain tensor, ε_{ij} is the dissipation

rate tensor and D_{ij}^t is the turbulent diffusion tensor. All these terms, besides the production

term, were modified from the original RST framework. The pressure-strain and dissipation rate

tensors are solved by Equation 22

$$\phi_{ij}^* - \varepsilon_{ij} = (1 - \alpha^3)\left(\phi_{ij}^w - \varepsilon_{ij}^w\right) + \alpha^3\left(\phi_{ij}^h - \varepsilon_{ij}^h\right) \tag{22}$$

with

$$\phi_{ij}^w = -5\frac{\varepsilon}{k}\left[\overline{u_i u_k}n_j n_k + \overline{u_j u_k}n_i n_k - \frac{1}{2}\overline{u_k u_l}n_k n_l\left(n_i n_j - \delta_{ij}\right)\right] \tag{23}$$

$$\phi_{ij}^h = -\left(C_1 + C_1^* \frac{P}{\varepsilon}\right)\varepsilon a_{ij} + \left(C_3 - C_3^*\sqrt{a_{kl}a_{kl}}\right)kS_{ij}$$

$$+ C_4 k\left(a_{ik}S_{jk} + a_{jk}S_{ik} - \frac{2}{3}a_{lm}S_{lm}\delta_{ij}\right) + C_5 k\left(a_{ik}W_{jk} + a_{jk}W_{ik}\right)$$

(24)

$$\varepsilon_{ij}^w = \frac{\overline{u_\iota u_J}}{k}\varepsilon$$

(25)

$$\varepsilon_{ij}^h = \frac{2}{3}\varepsilon\delta_{ij}$$

(26)

The turbulent diffusion term, D_{ij}^t, is the Generalized Gradient Diffusion Hypothesis which was developed by Daly and Harlow [16], Equation 27. The hypothesis is based on the fact that heat transfer is fueled by anisotropic thermal diffusion.

$$D_{ij}^t = \nu \frac{\partial \overline{u_\iota u_J}}{\partial x_i} + C_s \frac{k}{\varepsilon}\overline{u_\iota u_J}\frac{\partial \overline{u_\iota u_J}}{\partial x_i}$$

(27)

The terms for the solution of the pressure-strain and dissipation rate tensors are defined as follows:

$$P = \frac{1}{2}P_{ii}$$

(27)

$$a_{ij} = \frac{\overline{u_\iota u_J}}{k} - \frac{2}{3}\delta_{ij}$$

(28)

$$S_{ij} = \frac{1}{2}\left(\frac{\partial U_i}{\partial x_j} + \frac{\partial U_j}{\partial x_i}\right)$$

(29)

$$W_{ij} = \frac{1}{2}\left(\frac{\partial U_i}{\partial x_j} - \frac{\partial U_j}{\partial x_i}\right) + \epsilon_{mji}\omega_m$$

(30)

The terms used to solve the turbulent dissipation rate transport equation are given as follows:

$$\tau = max\left(\frac{k}{\varepsilon}, C_t\sqrt{\frac{v}{\varepsilon}}\right) \tag{31}$$

$$C_{\varepsilon_2}^* = C_{\varepsilon_2}\left[1 - \alpha^3\left(1 - \frac{1 + 90|X|}{1 + 100|X|}\right)\right] \tag{32}$$

$$E = A_1 v\overline{u_k u_l} n_k n_l \frac{k}{\varepsilon}(1 - \alpha^3)\left(\frac{\partial \|S_{ij}n_i\|n_k}{\partial x_k}\right)^2 \tag{33}$$

The $C_{\varepsilon_2}^*$ term has been modified to account for the round-jet/plane-jet anomaly and was tested on free and rotating impinging jets. The term X is referred to as a measure of the vortex stretching and is given by Equation 34.

$$X = \tau^3 W_{ik} W_{kj} S_{ij} \tag{34}$$

Both turbulence models use the same elliptic blending function α, which are applied to their corresponding stress transport equations, φ for Lag EB K-Epsilon and $\overline{u_i u_j}$ for EB RST. The models vary in several ways, but only the turbulent diffusion, anisotropy tensor, the vorticity tensor, turbulent dissipation rate transport equations and the near-the-wall formulation will be discussed. The turbulent diffusion term is explicitly calculated for the EB RST model and is a function of the Reynolds Stresses, and is applied to all seven transport equations. Where for the Lag EB K-Epsilon model the turbulent diffusion is not explicitly calculated anywhere.

The anisotropy tensor for the Lag EB K-Epsilon model is defined by the Quadratic Constitutive Relationship and is directly embedded into the transport equation of the reduced stress term φ through f_w by M_{ij}. The Constitutive Relationship implies that anisotropy is a

23

function of turbulent kinetic energy, strain tensor and the absolute vorticity tensor. The anisotropy tensor is indirectly applied to the other two transport equations through iterative calculations. For the EB RST model the anisotropy tensor and the Reynolds Stresses are interdependently related. For this reason, it is assumed that the EB RST model will predict the effects of anisotropy more accurately then the Lag EB K-Epsilon model.

The vorticity tensors only differ in the sense that the Lag EB K-Epsilon model applies the $Spalart - Shur$ tensor, which is a function of the strain tensor, to its formulation. The location of application for the vorticity tensors of each model is also different. For the EB RST model, at the wall where $\alpha = 0$ the vorticity tensor is not applied anywhere in the transport equations, since it is only applied in the far-away-from wall pressure-strain term ϕ_{ij}^h and the dissipation rate transport equation through $C_{\varepsilon_2}^*$ by X. On the contrary for the Lag EB K-Epsilon model the vorticity tensor is directly applied to the near-the-wall function f_w, which is used to calculate the reduced stress transport equation. For this reason, it is assumed that the Lag EB K-Epsilon model will predict the effects of rotation in the near-the-wall region more accurately.

The turbulent dissipation rate transport equation, for the Lag EB K-Epsilon model, is only directly related to the turbulent kinetic energy transport equation. The dependency of dissipation rate on turbulent kinetic energy is known to cause overpredictions in the calculation of turbulent kinetic energy. Which is a well-known short coming to the two equation turbulence models. Even though the Lag EB K-Epsilon turbulence model solves for an additional transport equation, it is expected that turbulent kinetic energy may be overpredicted. For the EB RST model the turbulent dissipation rate transport equation and the Reynolds Stress transport

equations are independently related. For this reason, it is assumed that the EB RST model will calculate the dissipation rate more accurately and the Lag EB K-Epsilon model may underpredict dissipation, resulting in an overprediction of turbulent kinetic energy.

The near-the-wall formulations vary in several ways, but only a discussion with respect to turbulent dissipation rate will be presented. For the Lag EB K-Epsilon model the dissipation is only applied to f_w in the first and fourth terms through τ. For the EB RST model the ϕ_{ij}^w and ε_{ij}^w functions are both directly proportional to the dissipation rate. With this relationship it is assumed that turbulent kinetic energy may be overpredicted for the Lag EB K-Epsilon model, with respect to the EB RST model, in the near-the-wall region.

Boundary Conditions

The boundary conditions remained the same for all case studies. All the fluid regions had the motion specification established on a rotating reference frame. For the nonrotating cases the rotational speed was set to $0\ rpm$ and for rotating cases rotational speed was set to $13287\ rpm$. For the shower head hole model, the inner and outer surfaces of the impingement channel as well as the inner and outer diameter of the gas path were defined as symmetry planes. Figure 11 illustrates these surfaces. The coolant inlet was set to a mass flow inlet type, the gas inlet was set to stagnation inlet type and the gas outlet was set to a pressure outlet type, Figure 12. The no shower head holes model had an outlet boundary type on the outer surface of impingement channel, symmetry plane on inner impingement channel surface with the same

boundary types for the gas region, Figure 13. The boundary conditions for both models are illustrated in Tables 1 and 2. The physics values for the region boundaries were derived from a calorifically perfect ideal gas analysis with no loss assumption. The Mach numbers and flow angles were given by Timko [16] and the total properties were given by Halilah [17].

Table 1: Model with SH Hole Boundary Conditions

Region Boundaries	Coolant Inlet	Gas Inlet	Gas Outlet
Physics Conditions			
Reference Frame Specification	Rotating	Rotating	N/A
Relative Flow Direction	Boundary Normal	Components	N/A
Backflow Specification	N/A	N/A	Extrapolated (Static)
Physics Values			
Relative Mass Flow Rate	0.0005 kg/s	N/A	N/A
Relative Flow Direction	N/A	[-170.879, 180.968, 0]	N/A
Relative Total Pressure	N/A	6.393 bar	N/A
Relative Total Temperature	870 K	1616 K	N/A
Supersonic Static Pressure	7 bar	5.292 bar	N/A
Pressure	N/A	N/A	0 bar
Static Temperature	N/A	N/A	1447.2 K

Table 2: Model without SH Hole Boundary Conditions

Region Boundaries	Coolant Inlet	Coolant Outlet	Gas Inlet	Gas Outlet
Physics Conditions				
Reference Frame Specification	Rotating	N/A	Rotating	N/A
Relative Flow Direction	Boundary Normal	N/A	Components	N/A
Backflow Specification	N/A	N/A	N/A	Extrapolated (Static)
Mass Flux Specification	N/A	Specified Mass Fluxes	N/A	N/A
Physics Values				
Relative Mass Flow Rate	0.0005 kg/s	N/A	N/A	N/A
Relative Flow Direction	N/A	N/A	[-170.879, 180.968, 0]	N/A
Relative Total Pressure	N/A	N/A	6.393 bar	N/A
Relative Total Temperature	870 K	N/A	1616 K	N/A
Supersonic Static Pressure	7 bar	N/A	5.292 bar	N/A
Pressure	N/A	N/A	N/A	0 bar
Static Temperature	N/A	N/A	N/A	1447.2 K
Mass Flow Rate	N/A	0.0005 kg/s	N/A	N/A
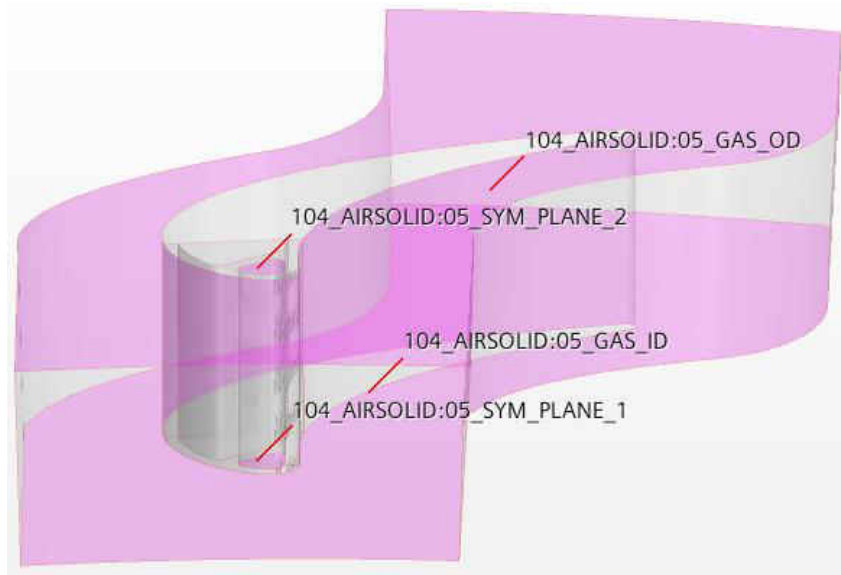
Figure 11: Symmetry Plane Boundary Condition Types of System
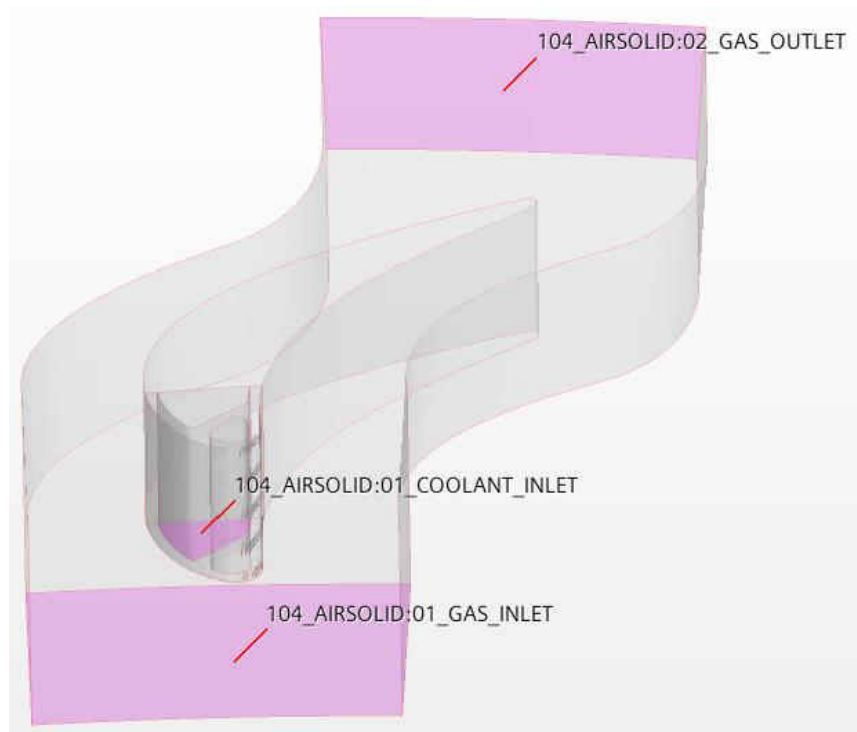
Figure 12: Coolant Inlet, Gas Inlet and Gas Outlet Boundary Surfaces
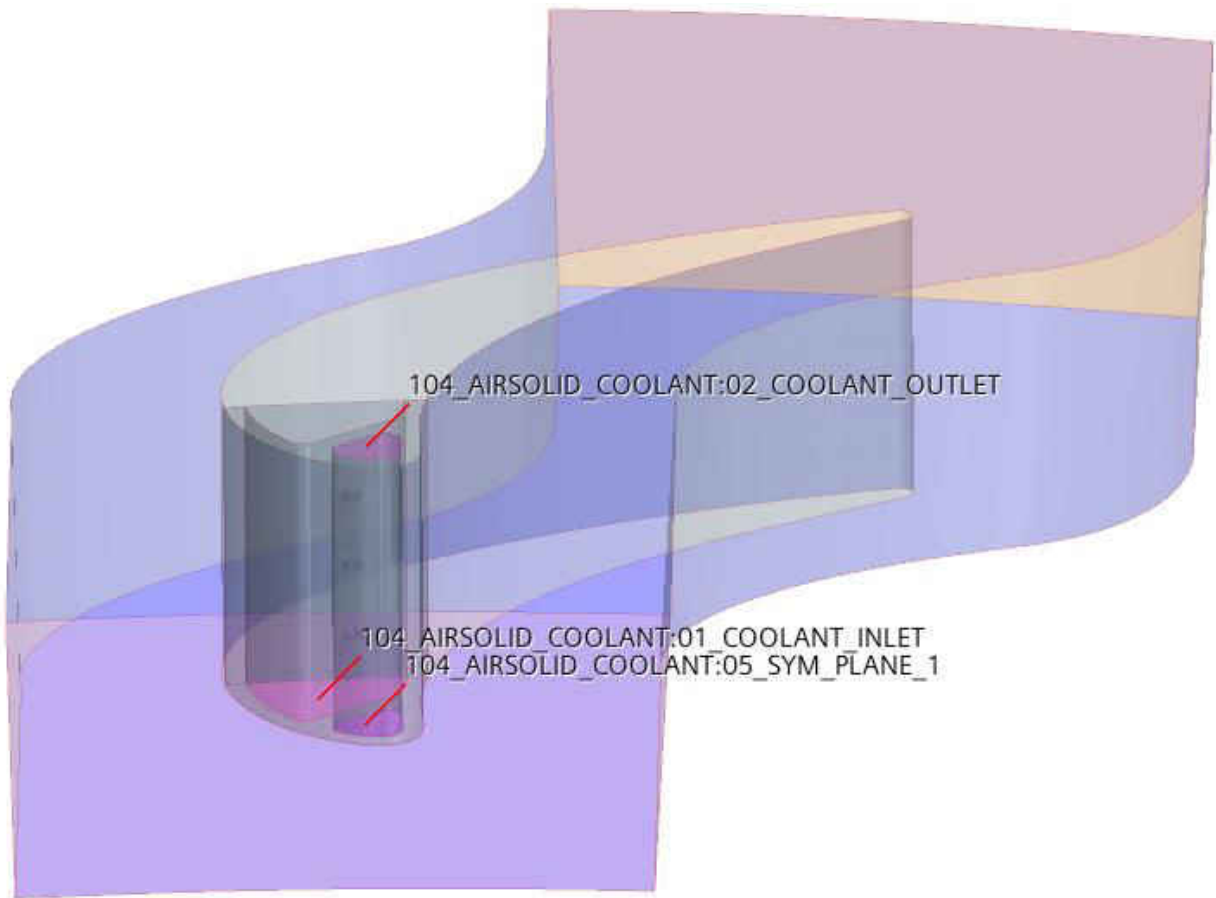
Figure 13: No SH Hole Model Boundary Types

Contact Interfaces

The interfaces consisted of contact resistance and periodic. Contact resistances were placed along all surfaces of external metal for the purpose of simulating a thermal barrier coating. The contact resistance value was set to $0.0001 \; m^2 K/W$. A periodic contact was placed on the outer tangential surfaces of the gas path with rotational transformation about the engine centerline, Figure 14. Periodic contacts were also placed on the exit and inlet of the inner and outer most shower head holes of the system domain with translational transformation, Figure 15. The periodic contacts on the split shower head holes were necessary for creating a uniform pressure gradient for the middle jet.
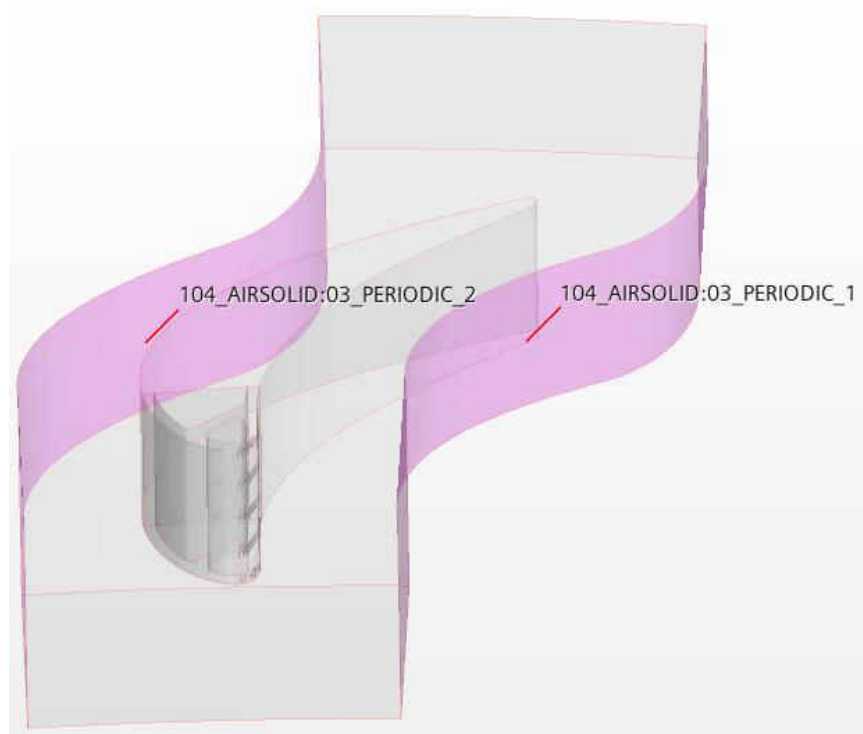
Figure 14: Gas Flow Path Rotational Periodic Contacts
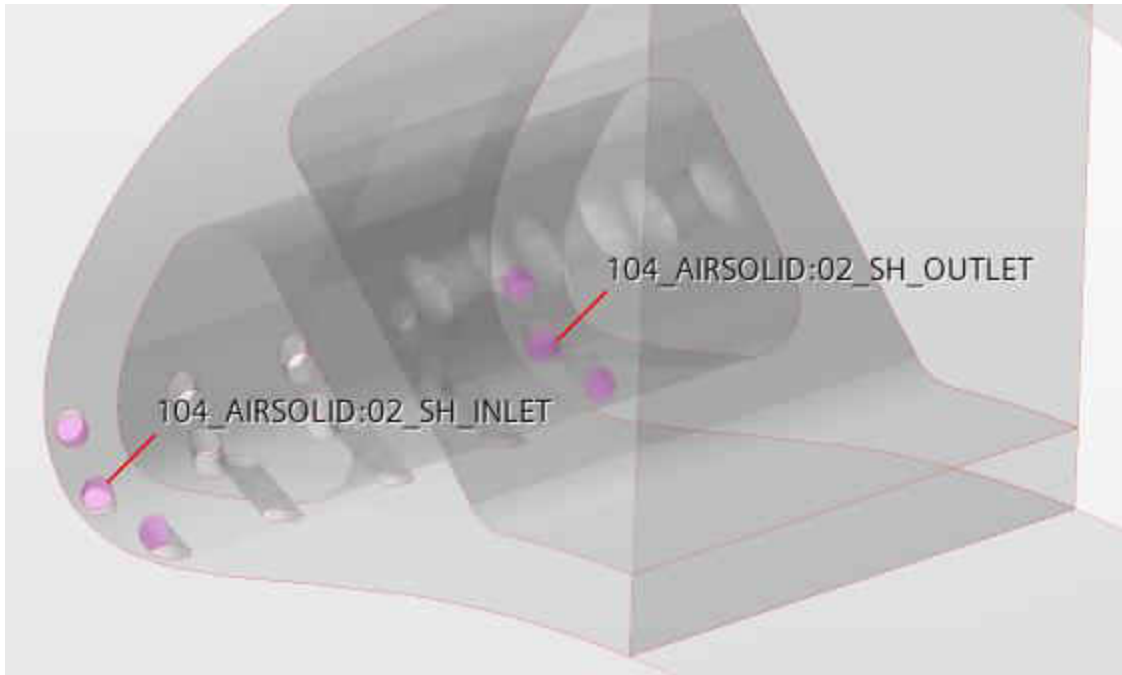
Figure 15: Shower Head Hole Translational Periodic Contact

Convergence Procedure

The solution to the EB RST model was highly unstable. The flow fields continuously oscillated about a mean value. In order to achieve an accurate converged solution probes were placed within the flow field to monitor levels of TKE and velocity, Figure 16. Once it was validated that the solution oscillated about a mean value, iteration averages were conducted on the probe monitors and on the flow field, Figures 17 and 18.
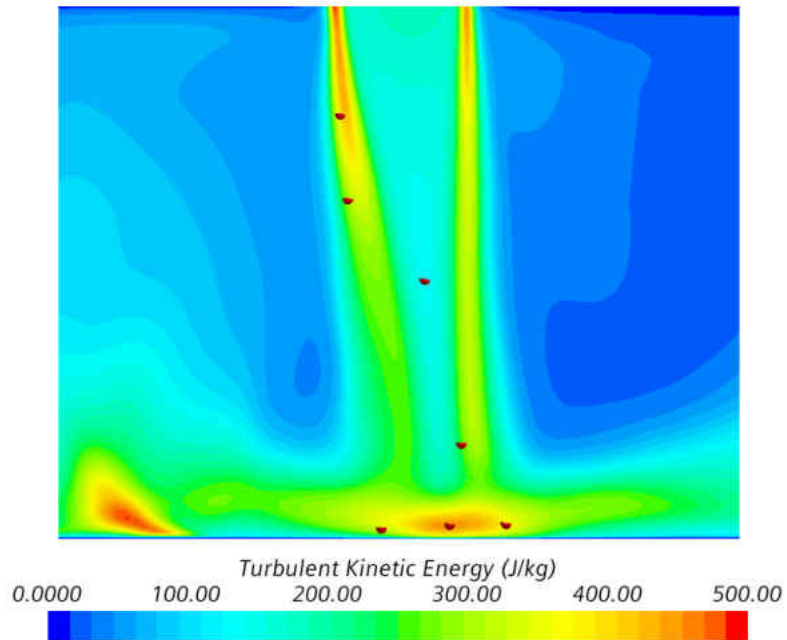
Figure 16: Flow Field Monitor Probes
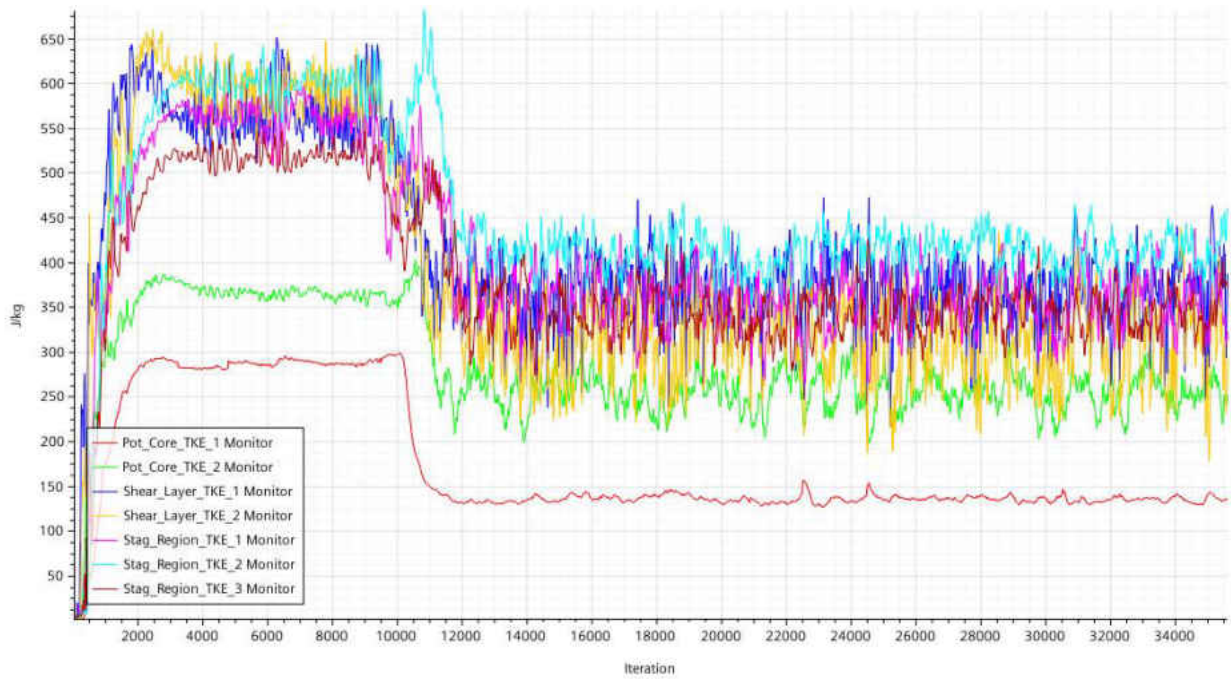
Figure 17: Oscillating Solution
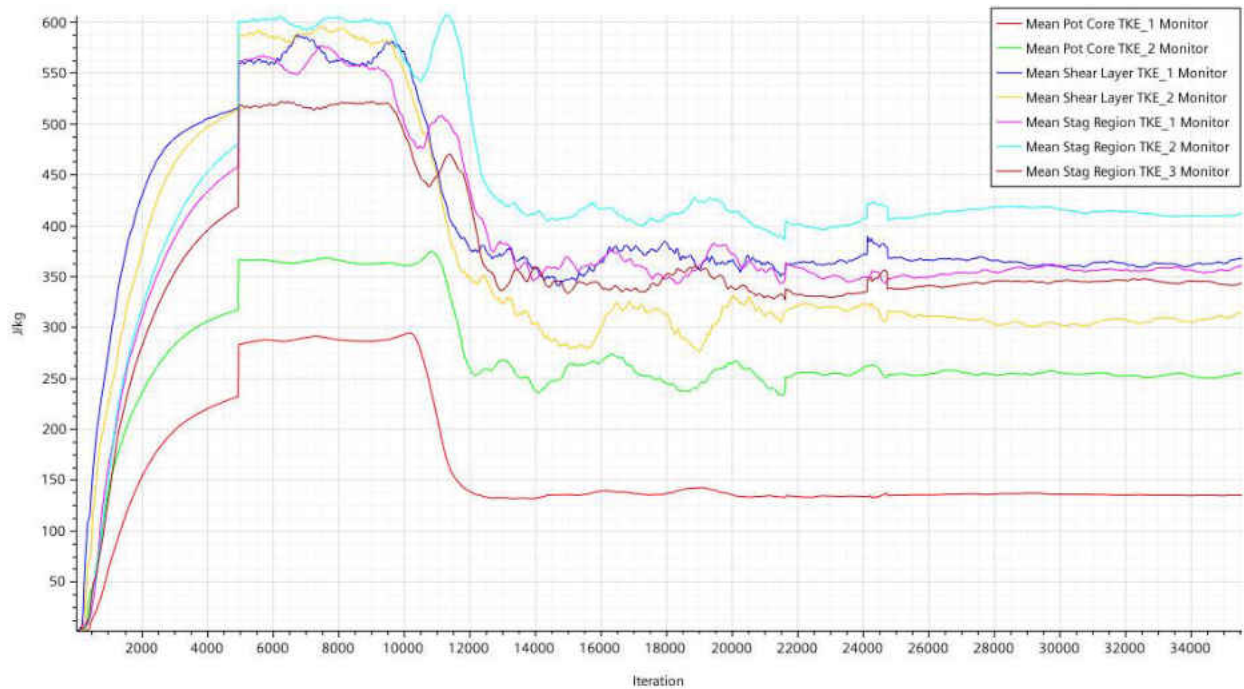
Figure 18: Iteration Averaged Oscillating Solution

Grid Uncertainty Study

Details for the procedure are given by Celik, I.B. et al. [19]. The critical value used for the analysis was the section area average Nusselt Number on impingement surface. Results of the study for both meshes of each turbulence model are illustrated in Table 3 and Table 4.

For the Lag EB K-Epsilon turbulence model the mesh with shower head holes had an approximate relative error of **1.459%**, an extrapolated relative error of **1.260%** and an oscillating fine-grid convergence index of **4.603 %**. The mesh without shower head holes had an approximate relative error of **2.499%,** an extrapolated relative error of **6.975%** and an oscillating fine grid convergence of **9.373 %**.

33

Table 3: Grid Uncertainty Results for Lag EB K-Epsilon

	Shower Head Hole Mesh	**No Shower Head Hole Mesh**
rf	1.333	1.333
$b_1 (mm)$	0.703125	0.703125
$b_2 (mm)$	0.9375	0.9375
$b_3 (mm)$	1.250	1.250
ϕ_1	51.41	38.41
ϕ_2	50.66	37.45
ϕ_3	51.01	38.73
p	2.649	1
ϕ^{21}_{ext}	52.066	41.29
e^{21}_a	1.459%	2.499%
e^{21}_{ext}	1.260%	6.975%
GCI^{21}_{fine}	1.596%	9.373%

For the EB RST model the mesh with shower head holes had an approximate relative error of 0.996%, an extrapolated relative error of 0.752% and a fine grid convergence index of 0.947%. The mesh without shower head holes had an approximate relative error of 0.960%, an extrapolated relative error of 2.404% and a fine grid convergence index of 2.934%.

Table 4: Grid Uncertainty Results for EB RST

	Shower Head Hole Mesh	No Shower Head Hole Mesh
rf	1.333	1.333
$b_1(mm)$	0.703125	0.703125
$b_2(mm)$	0.9375	0.9375
$b_3(mm)$	1.250	1.250
ϕ_1	54.23	32.28
ϕ_2	53.69	32.59
ϕ_3	52.44	32.81
p	2.918	1.192
ϕ^{21}_{ext}	54.641	31.522
e^{21}_a	0.996%	0.960%
e^{21}_{ext}	0.752%	2.404%
GCI^{21}_{fine}	0.957%	2.934%

CHAPTER – 3: THEORETICAL ANALYSIS

The theoretical analysis consists of evaluation of the momentum equation. The momentum equation was used to analyze the forces, and their directions, that influence the motion of the fluid for both stationary and rotating reference frames. The rotational forces for relative fluid velocities were derived.

Momentum Equation

Stationary Reference Frame

For a stationary reference frame, the momentum equation is given by Equation 35. The body force is gravity and the surface forces are pressure and shear. The force of gravity is considered negligible in comparison to the pressure forces. Therefore, the forces driving the fluid motion are the pressure forces. The fluid is pushed through the impingement holes and out through the shower head cooling holes or radially outward through the impingement channel, depending on the cooling scheme.

$$\rho \frac{D\vec{V}}{Dt} = \rho \vec{g} - \nabla P + \mu \nabla^2 \vec{V} \tag{35}$$

Rotating Reference Frame

For a rotating reference frame, the momentum equation is given by Equation 36. The only difference between Equation 35 and Equation 36 is the body force term. For a rotating reference frame, the body forces are Coriolis and centrifugal. Depending on the rotational speed, relative velocity and radius these forces can significantly alter the behavior of the fluid. Therefore, these forces should never be ignored for a rotating system. Figure 19 illustrates a rotating reference frame with relative jet velocity.

$$\rho \frac{D\vec{V}}{Dt} = -2\rho(\vec{\Omega} \times \vec{V}) - \rho[\vec{\Omega} \times (\vec{\Omega} \times \vec{r})] - \nabla P + \mu\nabla^2\vec{V} \tag{36}$$
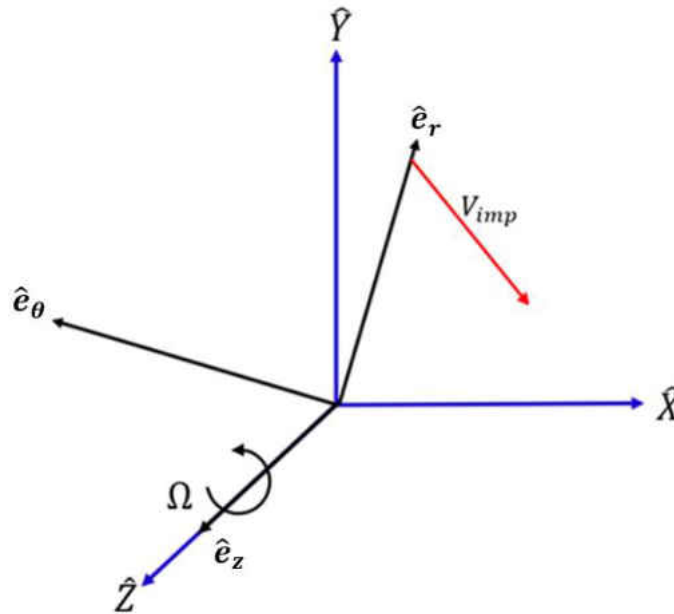
Figure 19: Rotating Reference Frame with Relative Jet Velocity

Coriolis on Impinging Jet

The relative velocity of impinging jet has a negative $\hat{e}_\theta$ component and a positive $\hat{e}_z$ component. Solving the cross-product gives a negative term in the $\hat{e}_r$ direction, Equation 37. For high jet speeds the Coriolis force will influence the jet in the negative radial direction. Figure 20 illustrates the Coriolis force vector diagram with respect to the impinging jet velocity and the rotational velocity.

$$-2\rho(\vec{\Omega} \times \vec{V}_{imp}) = -2\rho[\Omega\hat{e}_z \times (-v\hat{e}_\theta + w\hat{e}_z)] = -2\rho\Omega v\hat{e}_r \qquad (37)$$
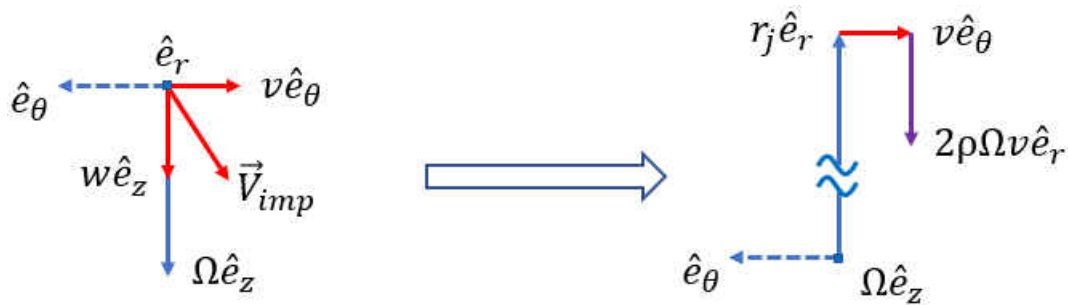
Figure 20: Coriolis Force Vector Diagram

Centrifugal Force

The result of the cross-products for the centrifugal force is a positive radial force, Equation 38. The vector diagram for the centrifugal force is shown in Figure 21.

$$-\rho\left[\vec{\Omega} \times (\vec{\Omega} \times \vec{r}_j)\right] = -\rho\Omega\hat{e}_z \times \Omega r_j\hat{e}_\theta = \rho\Omega^2 r_j\hat{e}_r \tag{38}$$
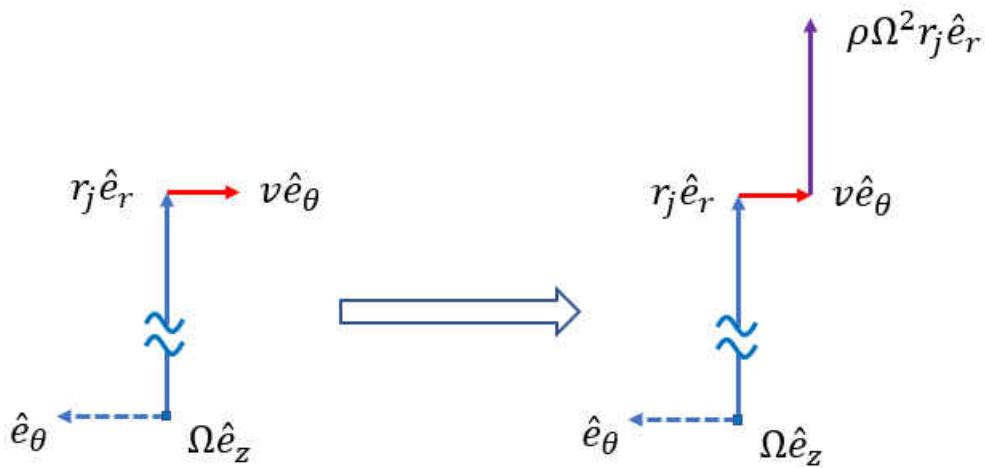
Figure 21: Centrifugal Force Vector Diagram

From the theoretical analysis it may be concluded that for higher impingement jet velocities, the Coriolis force will dominate and influence the jet in the radially inwards direction. For higher rotation speeds and larger radii, the centrifugal force will dominate and influence the jet radially outwards.

CHAPTER – 4: RESULTS AND DISCUSSION

The results are composed of a flow field study, internal heat transfer characteristics, and external blade temperatures. The flow field study consists of spanwise contour plots along with potential core velocity and turbulent kinetic energy (TKE) profile plots at increments of $1/6$ from the nozzle exit to the target surface. Figure 22 illustrates the spanwise view orientation with respect to the leading-edge top view, with h representing the distance from nozzle exit.
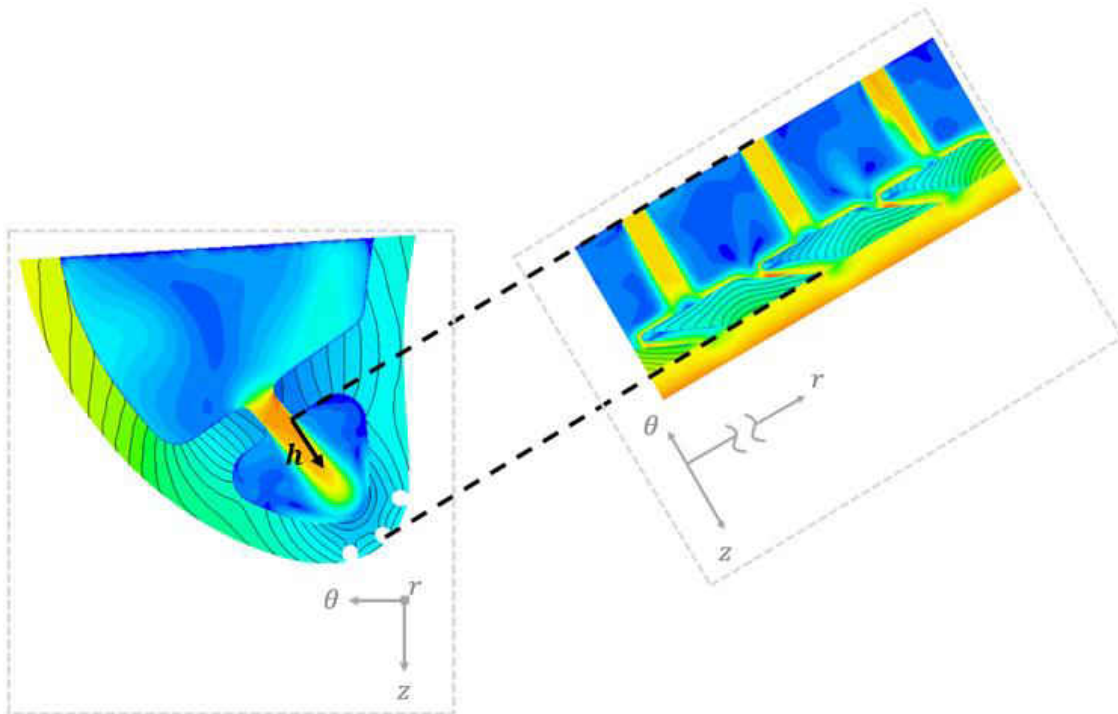
Figure 22: Spanwise View Orientation

The internal heat transfer analysis consists of contour plots for Nusselt Number and a spanwise Nusselt Number distribution through maximum Nusselt Number on the impingement surface. For the no shower head hole case studies this location was towards the suction side of

the impingement surface, dashed line in Figure 23. For the nonrotating shower head hole case studies this location was also towards the suction side of the impingement surface. For the rotating shower head hole case studies, the location was directly in line with the axis of the nozzle, dashed line in Figure 24.
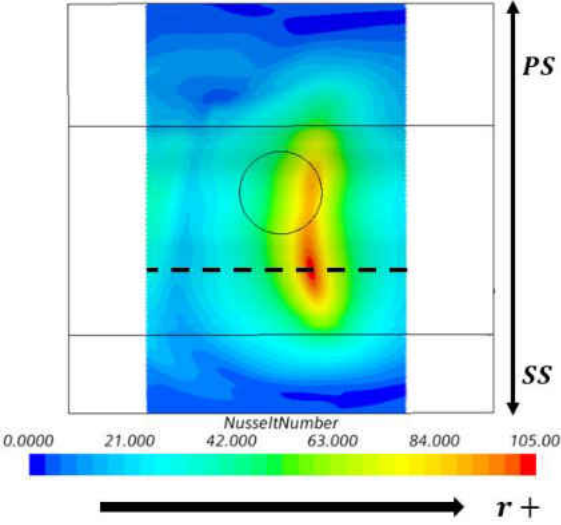
Figure 23: Location of Spanwise Nusselt Number Distribution for No SH Hole Case Studies
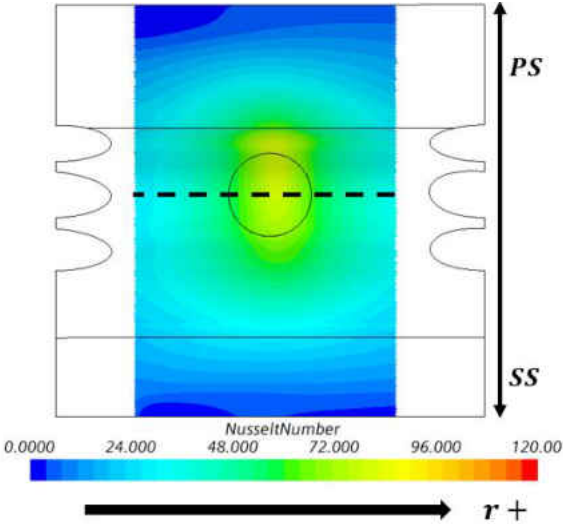
Figure 24: Location of Spanwise Nusselt Number Distribution for Rotating SH Hole Case Studies

The external blade temperature for each case study is presented as a temperature profile plot. The curves of the plots are polynomial fit curves through all the data points along the middle section of the external surface of the blade. Figure 25 highlights the surfaces used for the temperature analysis.
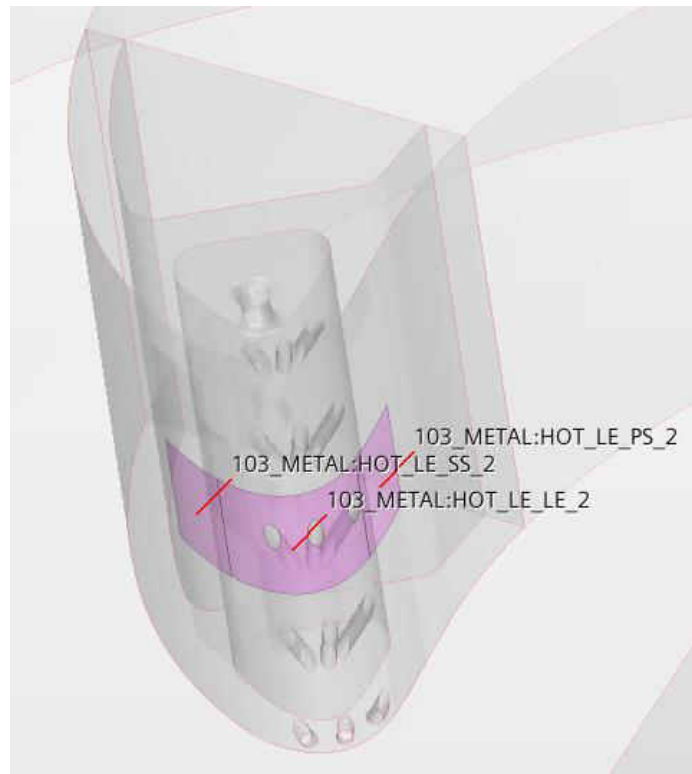
Figure 25: External Surfaces for Temperature Profile Analysis

Flow Field Analysis: Velocity

The three impinging jet flow field for the nonrotating, no shower head holes, Lag EB K-Epsilon and EB RST models is illustrated in Figures 26 and 27, respectively. Inspection of the domain flow field, for both turbulence models, shows some jet bending which is due to the jet interacting with the upstream fountain caused by the colliding wall jets. This phenomenon can be explained by comparison to the flow field of flat plate impingement.

The flow field for flat plate impingement in a rectangular channel is shown in Figure 28. The region boundary types, and physics values, were the same as that of the leading-edge case. The geometry for the flat plate impingement had the same nozzle diameter, nozzle length, nozzle to target surface distance, nozzle spanwise pitch and impingement channel length. The orientation of the nozzles was the same as well. The only difference being the cross-sectional area of the impingement channel, were the ratio of flat plate to leading edge cross-sectional areas was 4.08. Figure 29 illustrates the comparison of cross-sectional areas for impingement channels. The curved enclosed geometry of the leading-edge impingement channel prevents the crossflow of the upstream jets from moving around the downstream jets. Therefore, the upstream fountain is forced into the free jet region, resulting in jet bending seen in the flow field.
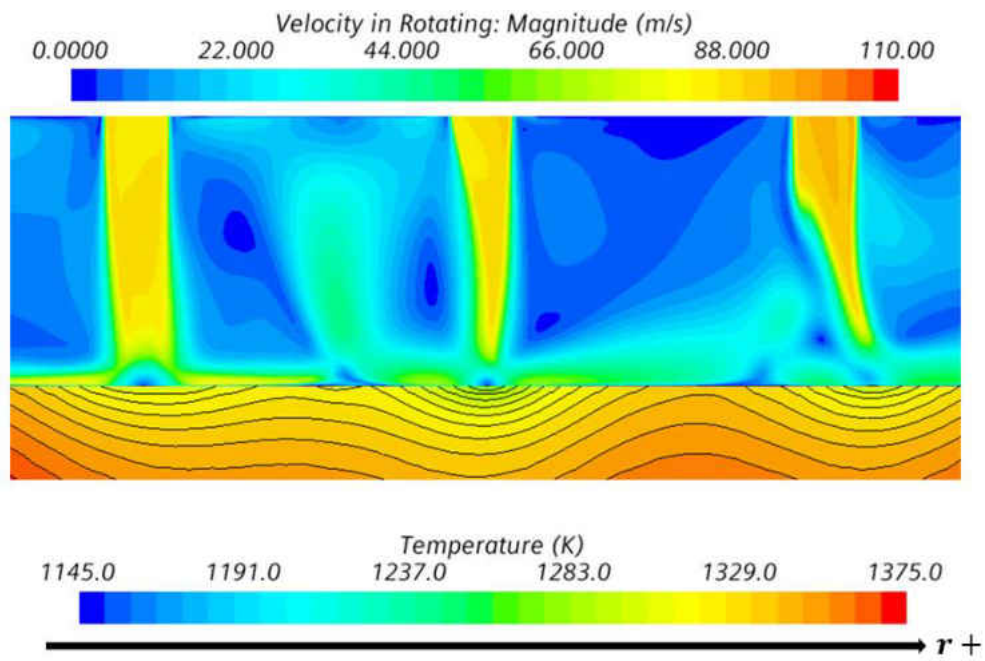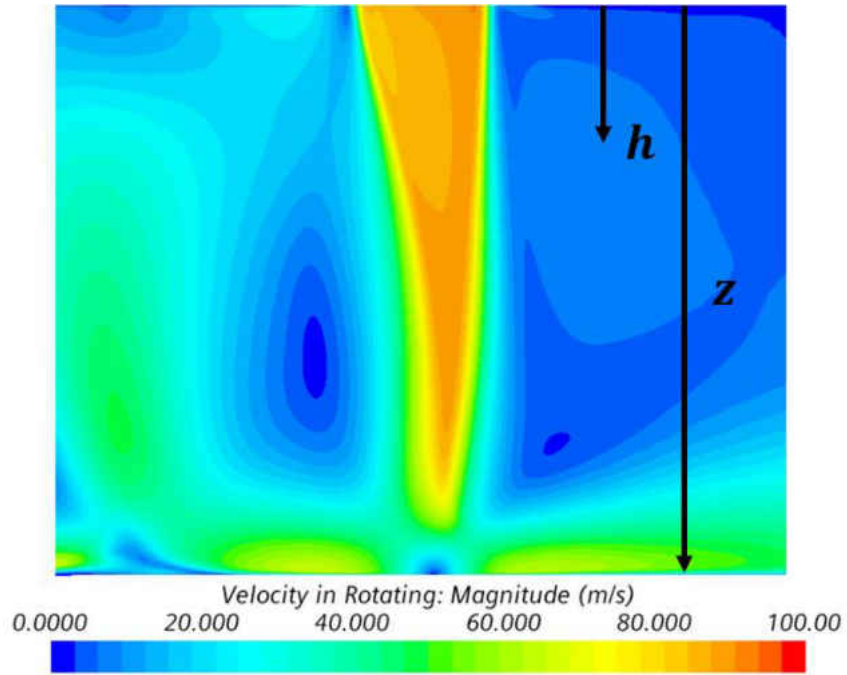
Figure 26: Nonrotating No SH Hole Domain Flow Field (Lag EB K-Epsilon)
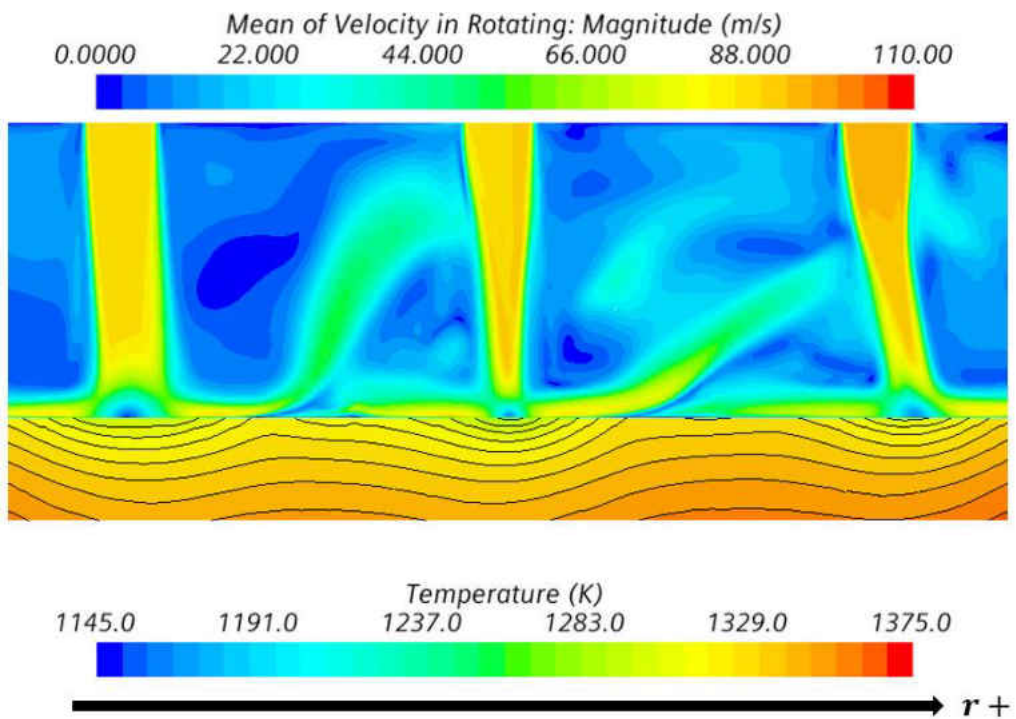
Figure 27: Nonrotating No SH Hole Domain Flow Field (EB RST)
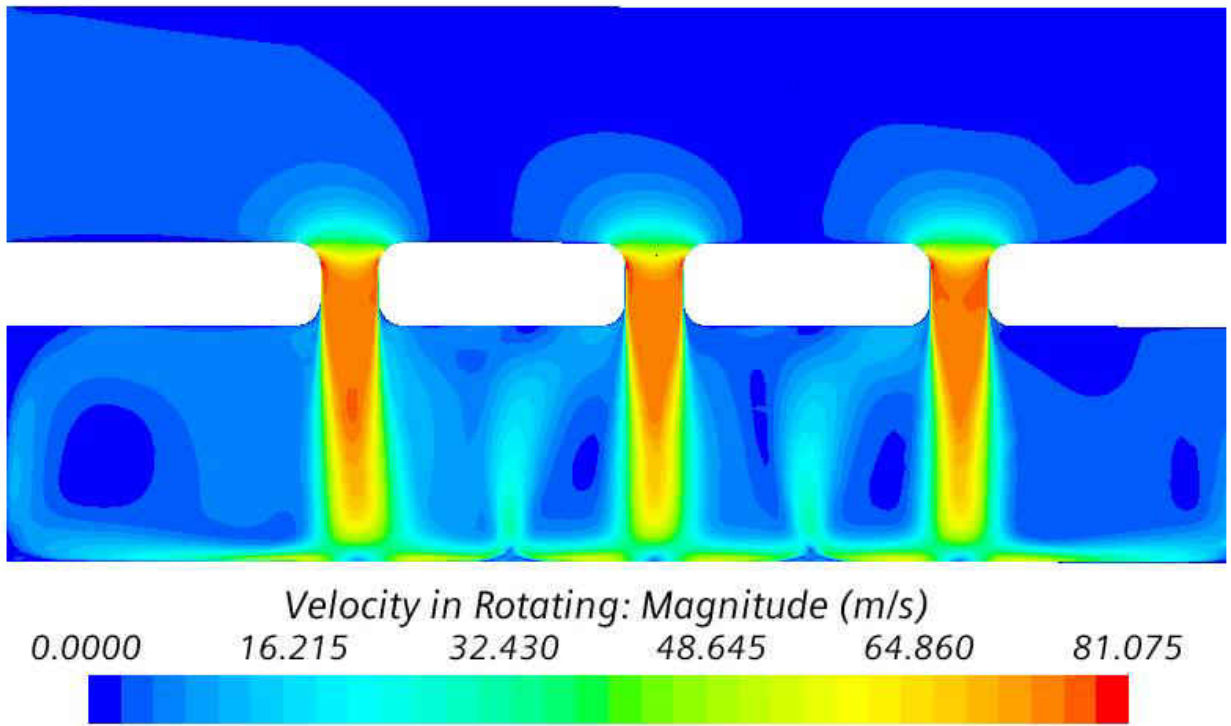
Figure 28: Flat Plate Impingement Flow Field
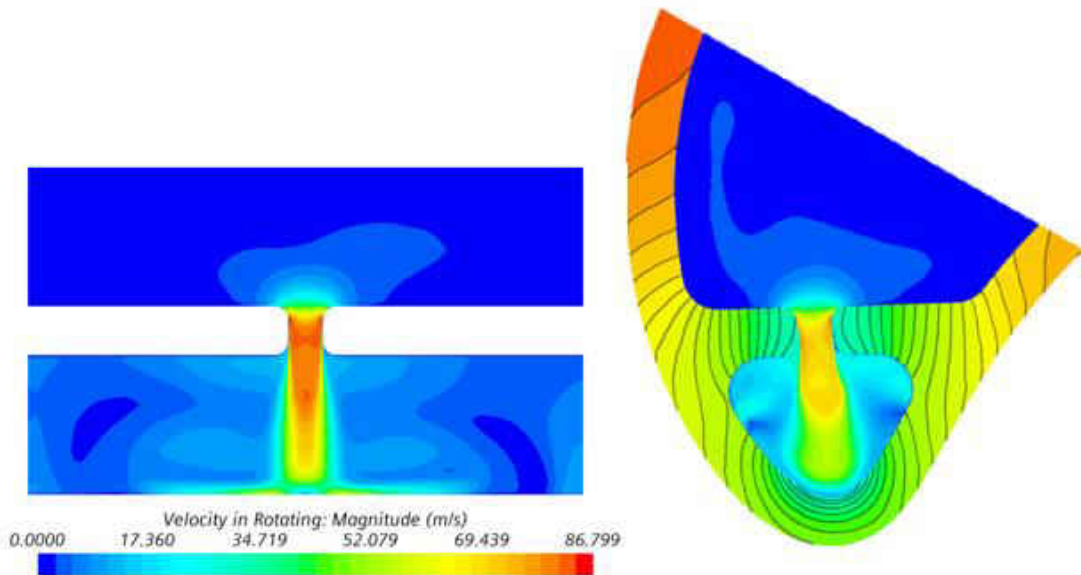
Figure 29: Impingement Channel Cross-sectional Area Comparison

45

The individual jet flow fields, for each turbulence model, are shown in Figures 30 and 31. With z representing the distance from nozzle exit to target surface and h representing the distance from nozzle exit. Figures 32 and 33 illustrate the potential core velocity profiles. The Lag EB K-Epsilon model shows a somewhat uniform velocity profile with constant magnitude up until $h/z = 5/6$ where the profile is parabolic and has decreased in magnitude. The EB RST model shows a similar velocity profile but maintains constant magnitude throughout the free jet region. Both turbulence models show a decrease in potential core thickness and a shift in the downstream direction. The Lag EB K-Epsilon models shows more of a drastic shift.
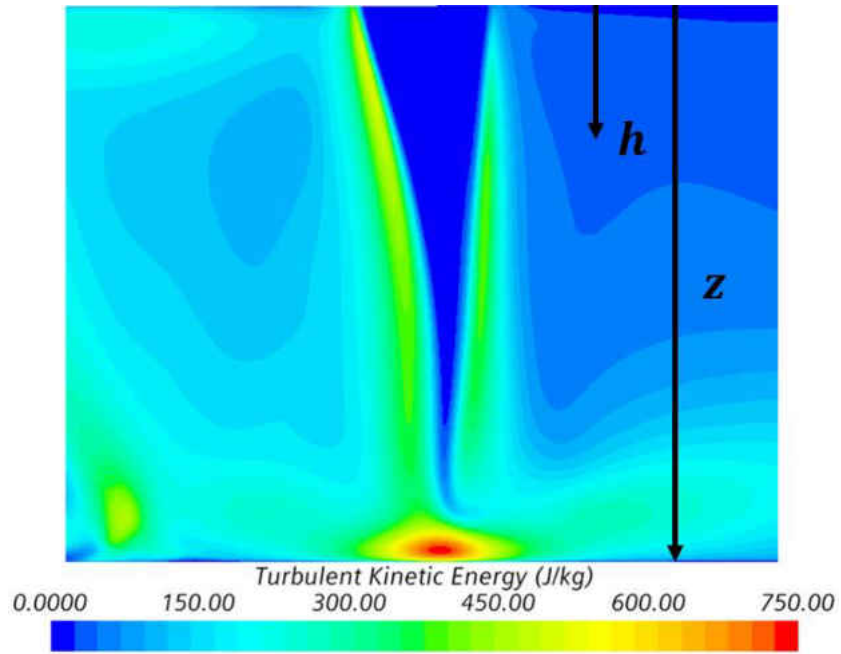
Figure 30: Nonrotating No SH Hole Jet Velocity Flow Field (Lag EB K-Epsilon)
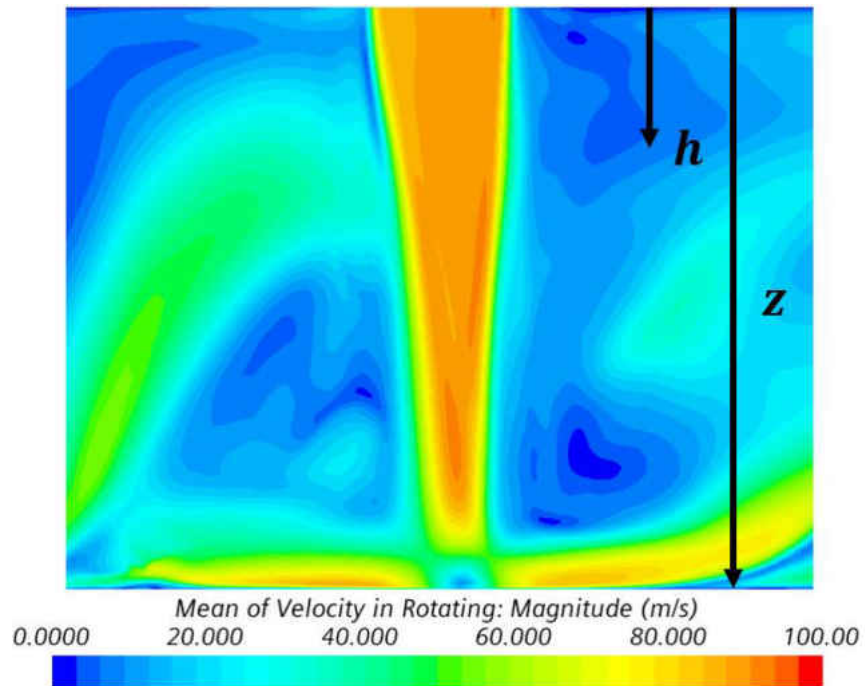
Figure 31: Nonrotating No SH Hole Jet Velocity Flow Field (EB RST)
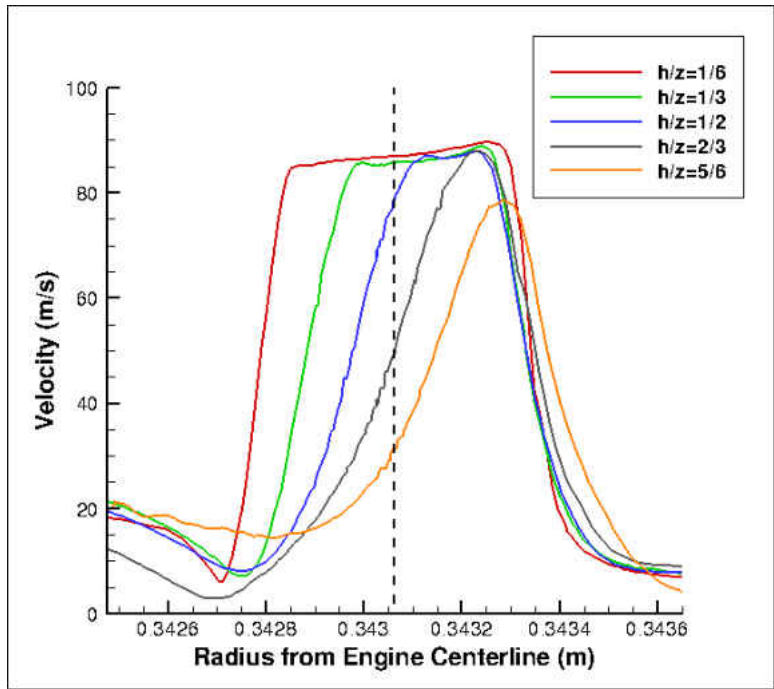
Figure 32: Nonrotating No SH Hole Potential Core Velocity Profiles (Lag EB K-Epsilon)
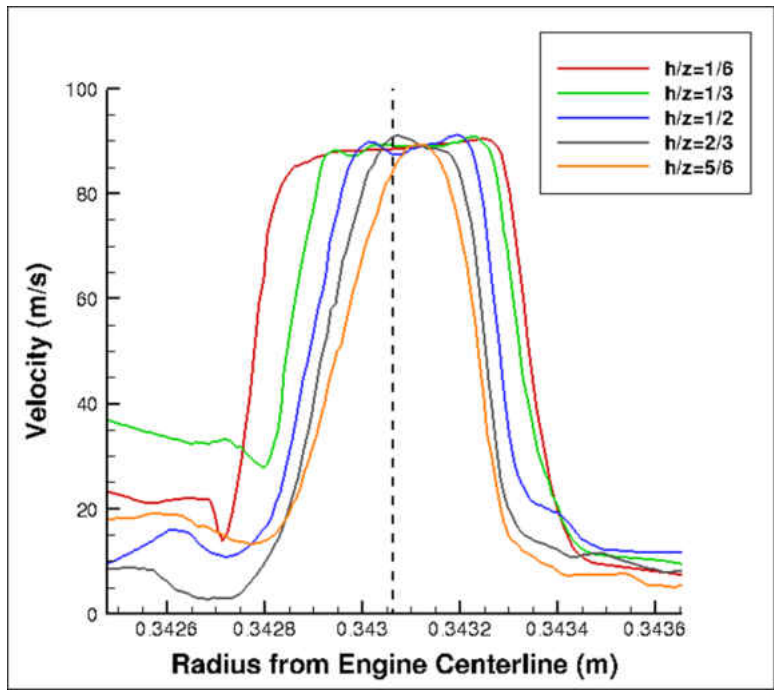
Figure 33: Nonrotating No SH Hole Potential Core Velocity Profiles (EB RST)

48

Flow Field Analysis: Turbulent Kinetic Energy

Figures 34 and 35 illustrate the TKE flow field for the nonrotating no shower head hole

model. The TKE flow field for the Lag EB K-Epsilon model shows maximum TKE at the stagnation

region. While for the EB RST model TKE values at stagnation are approximately zero. The TKE

profile plots for the free jet are shown in Figures 36 and 37. The Lag EB K-Epsilon model

illustrates zero TKE throughout the potential core until $h/z = 5/6$, where the potential core has

completely collapsed. The EB RST model shows zero TKE in the potential core throughout the

entire free jet region. Both turbulence models illustrate shear layer growth, while the growth for

the Lag EB K-Epsilon model is slightly greater.

The higher TKE levels in the shear layer for the Lag EB K-Epsilon model can be explained

by the expected under prediction of dissipation, resulting in an overprediction for TKE. The

slightly greater increase in shear layer growth, for the Lag EB K-Epsilon model, is assumed to be

due to the overprediction in TKE. The high TKE values at stagnation for the Lag EB K-Epsilon

model, in comparison to the EB RST model, can be explained by a combination of factors. First

being that the potential core has completely collapsed before making impingement, which is due

to the assumed overprediction of shear layer growth. The second being that dissipation may be

underpredicted at the wall in comparison the EB RST model. Lastly the EB RST model applies the

Generalized Gradient Diffusion Hypothesis which is assumed to play a role in the TKE levels at

stagnation

Figure 34: Nonrotating No SH Hole Jet TKE Flow Field (Lag EB K-Epsilon)
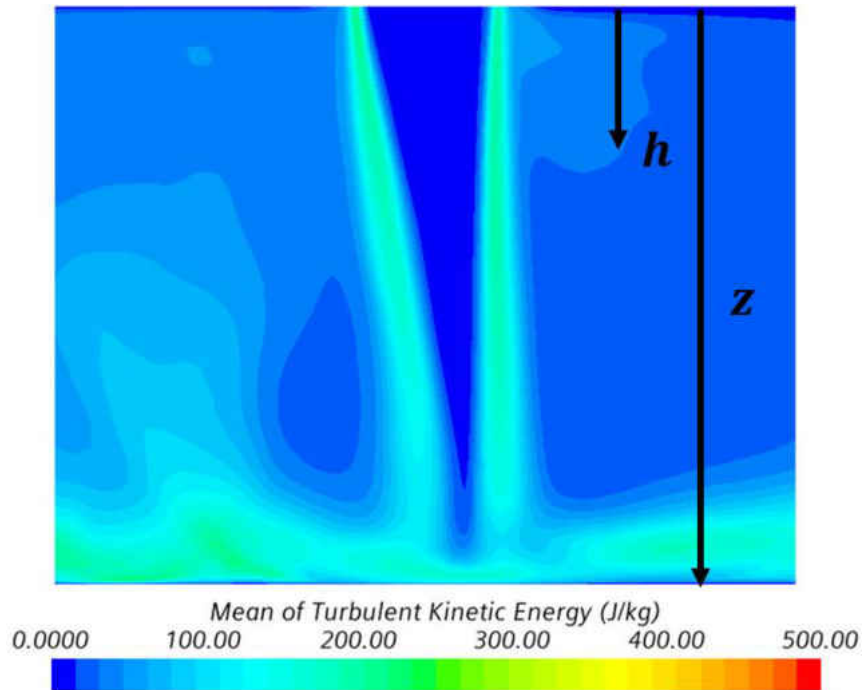
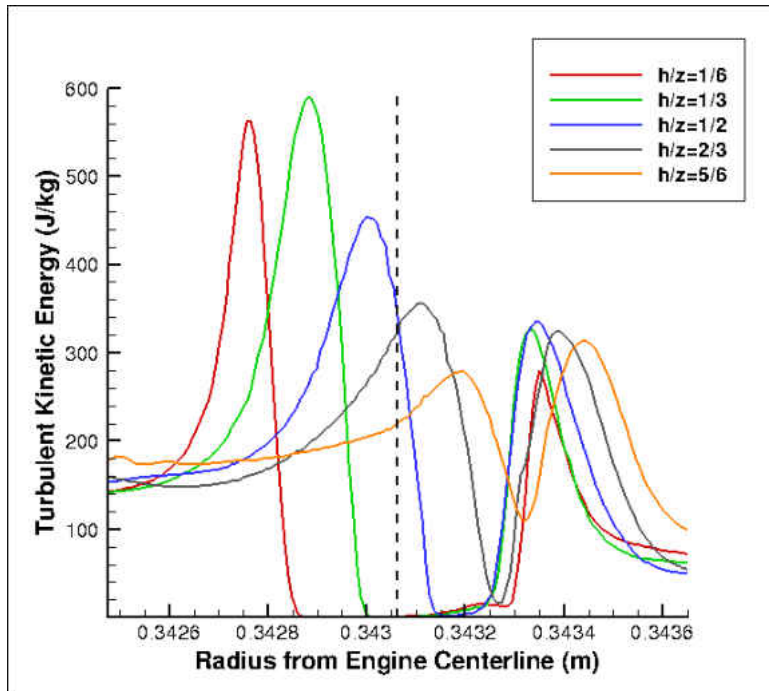*Figure 35: Nonrotating No SH Hole Jet TKE Flow Field (EB RST)*

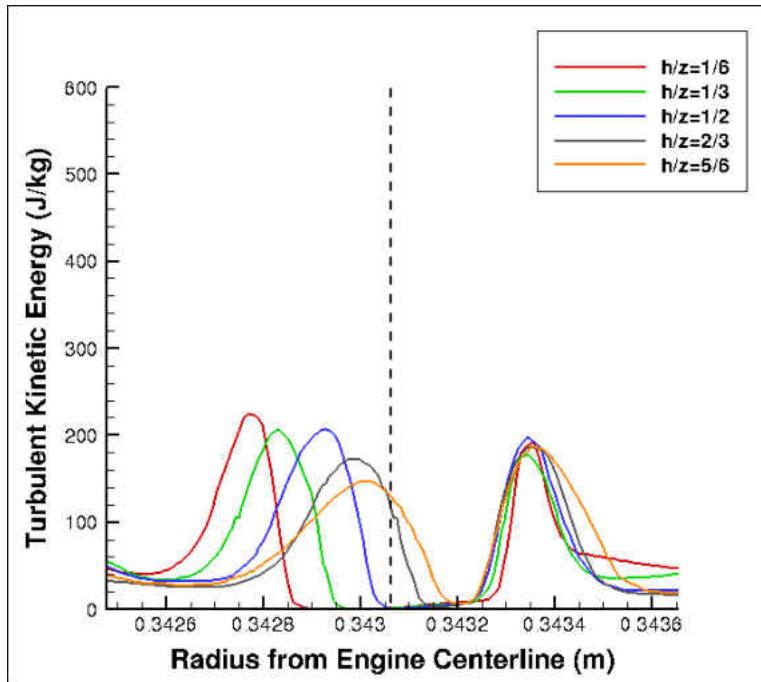*Figure 36: Nonrotating No SH Hole Jet TKE Profiles (Lag EB K-Epsilon)*

Figure 37: Nonrotating No SH Hole Jet TKE Profiles (EB RST)

Heat Transfer Analysis: Nusselt Number

The Nusselt Number contour plots for the nonrotating no shower head hole model is illustrated in Figures 38 and 39. Both turbulence models illustrate an elongated Nusselt Number distribution, which is due to the potential core deformation caused by the jet interaction with the upstream fountain. The location of maximum Nusselt Number for both models is towards the suction side of the impingement surface. This is possibly due to the suction side surface having slightly less curvature than the pressure side surface.

Figure 40 illustrates the spanwise distribution through Nusselt Number maximum, for both turbulence models. Both turbulence models are in fair agreement with one another, with respect to trend. For the Lag EB K-Epsilon model the maximum Nusselt Number is approximately 20% greater than that of the EB RST model. The maximum Nusselt Number, for the Lag EB K-Epsilon model, is also slightly offset from that of the EB RST model. The Wall Y+ values for impingement surface are illustrated in Figures 41 and 42. For both turbulence models, Wall Y+ was held to the optimal value for STAR-CCM+, $y+\sim 1$.
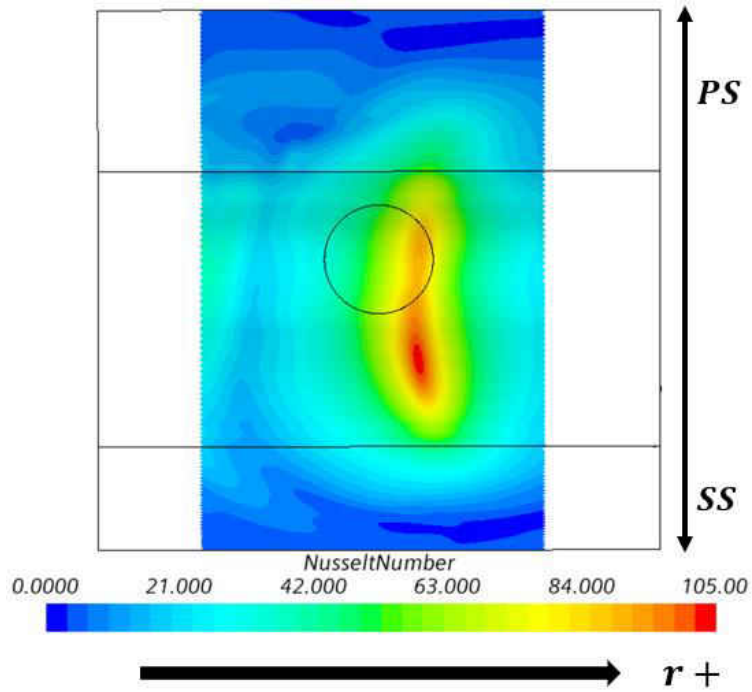
Figure 38: Nonrotating No SH Hole Nusselt Number (Lag EB K-Epsilon)
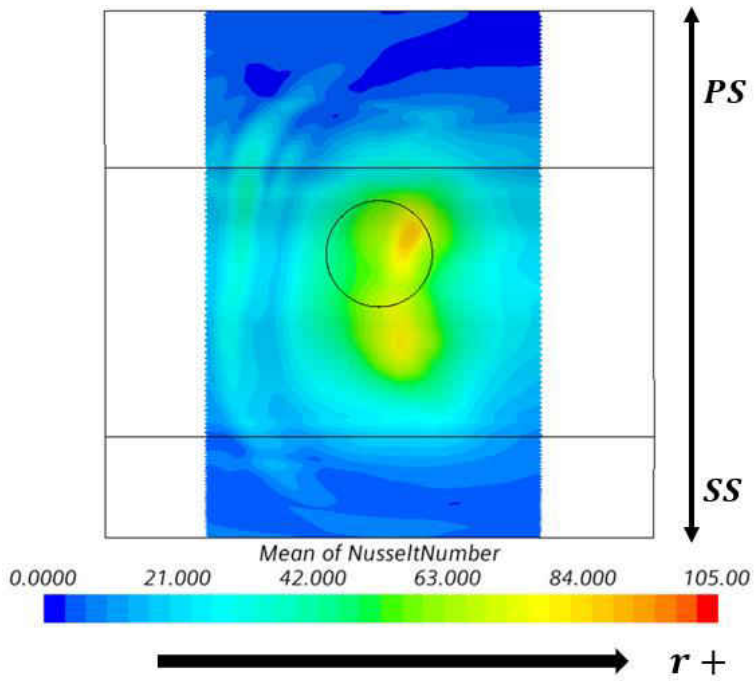
Figure 39: Nonrotating No SH Hole Nusselt Number (EB RST)
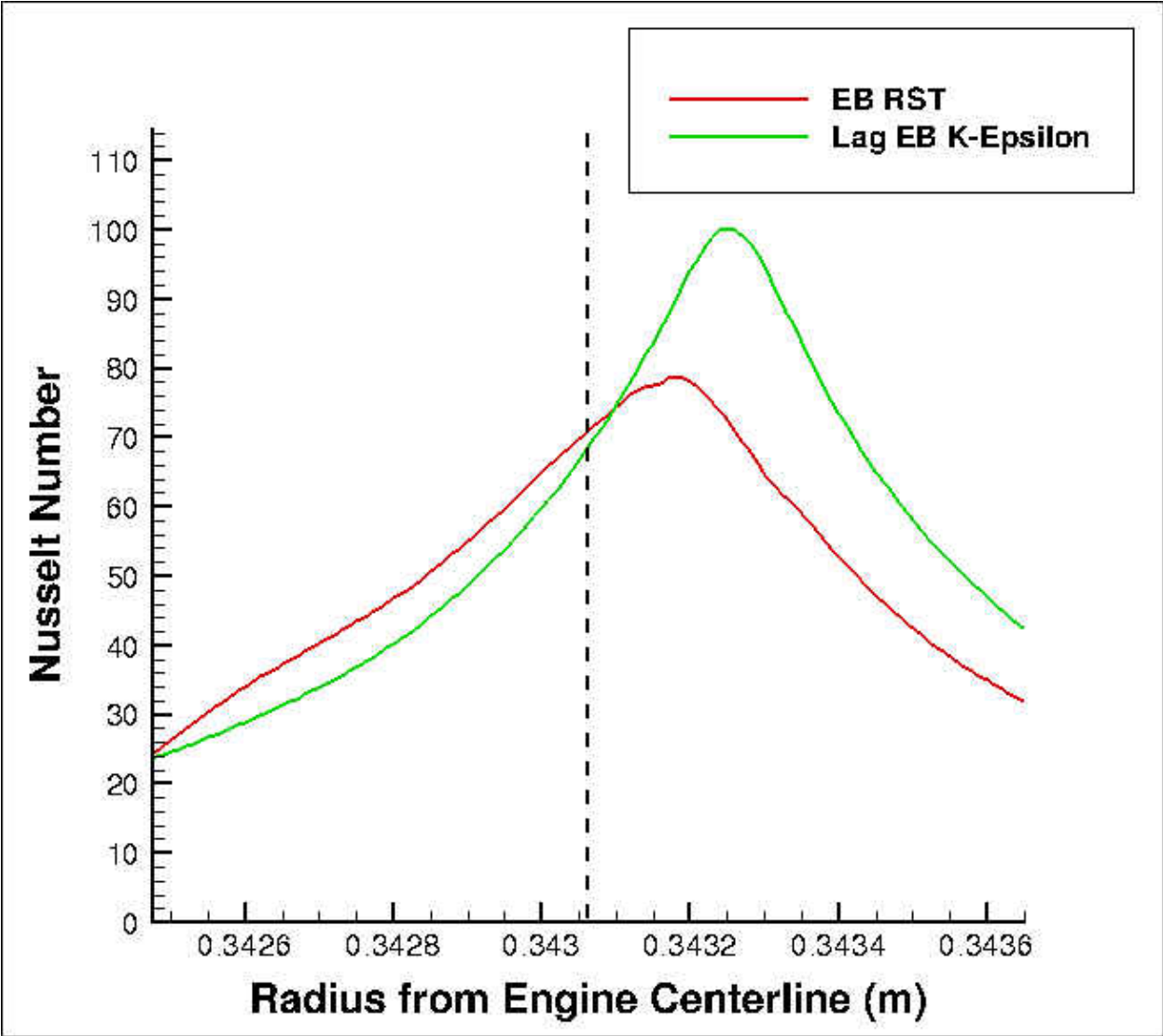
Figure 40: Nonrotating No SH Hole Spanwise Nusselt Distribution
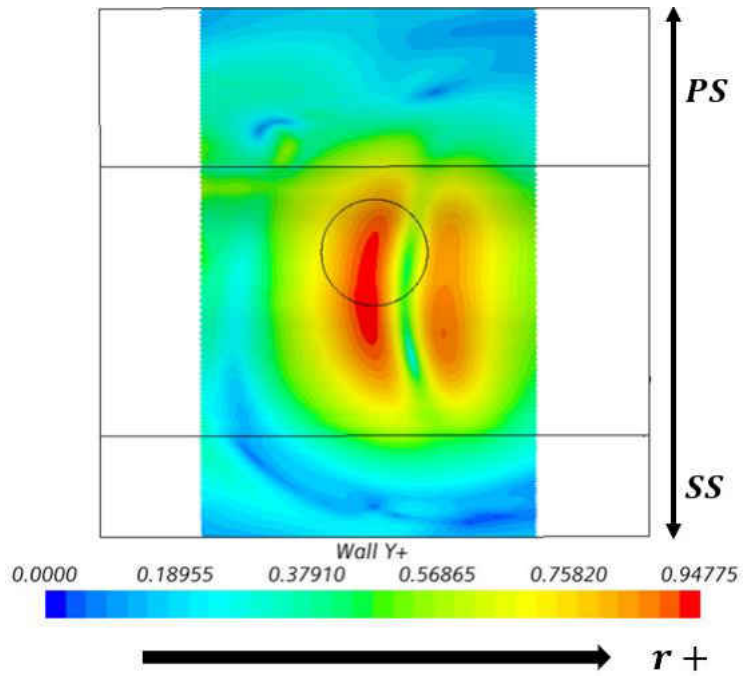
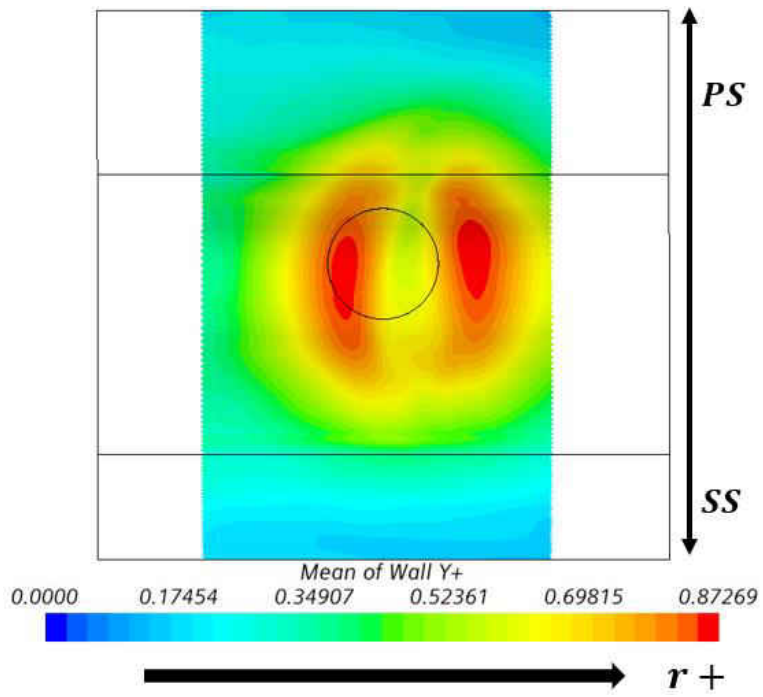*Figure 41: Nonrotating No SH Hole Impingement Wall Y+ (Lag EB K-Epsilon)*

Figure 42: Nonrotating No SH Hole Impingement Wall Y+ (EB RST)

External Blade Temperature

The external blade temperature profiles for both turbulence models is shown in Figure 43. Both models illustrate an almost identical trend with approximately equivalent values for minimum temperature. The only difference being that the curves are offset from each other. Wall Y+ values for external blade surface were within the optimal range, as shown in Figures 44 and 45.
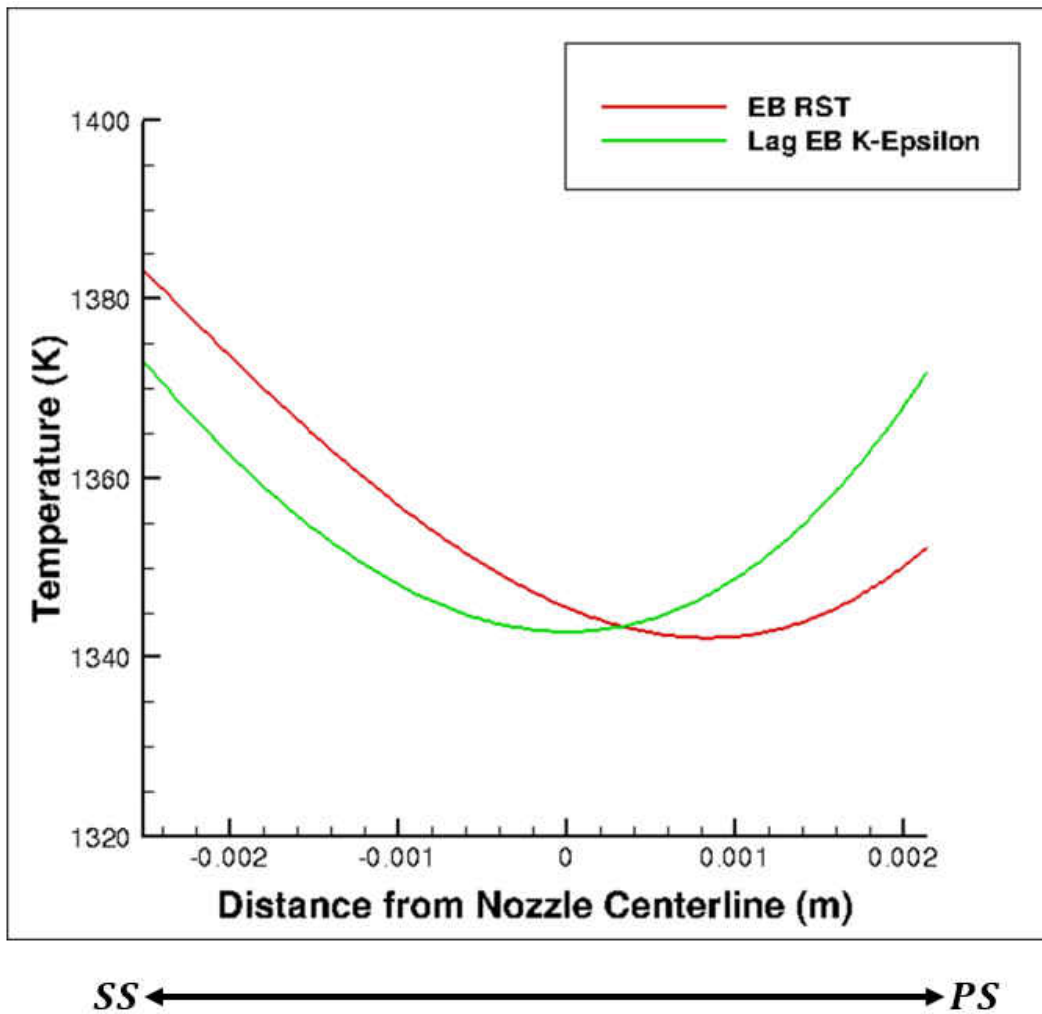
Figure 43: Nonrotating No SH Hole External Blade Temperature Profile

Wall Y+

| 0.0000 | 0.17729 | 0.35458 | 0.53187 | 0.70915 | 0.88644 |
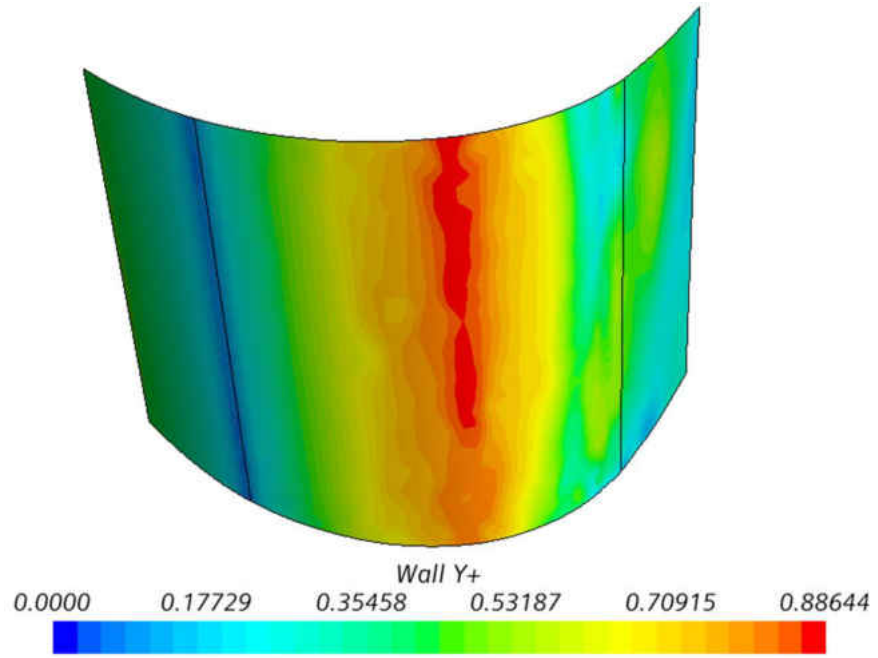
Figure 44: Nonrotating No SH Hole External Blade Surface Wall Y+ (Lag EB K-Epsilon)

Wall Y+

| 0.0000 | 0.17200 | 0.34401 | 0.51601 | 0.68802 | 0.86002 |
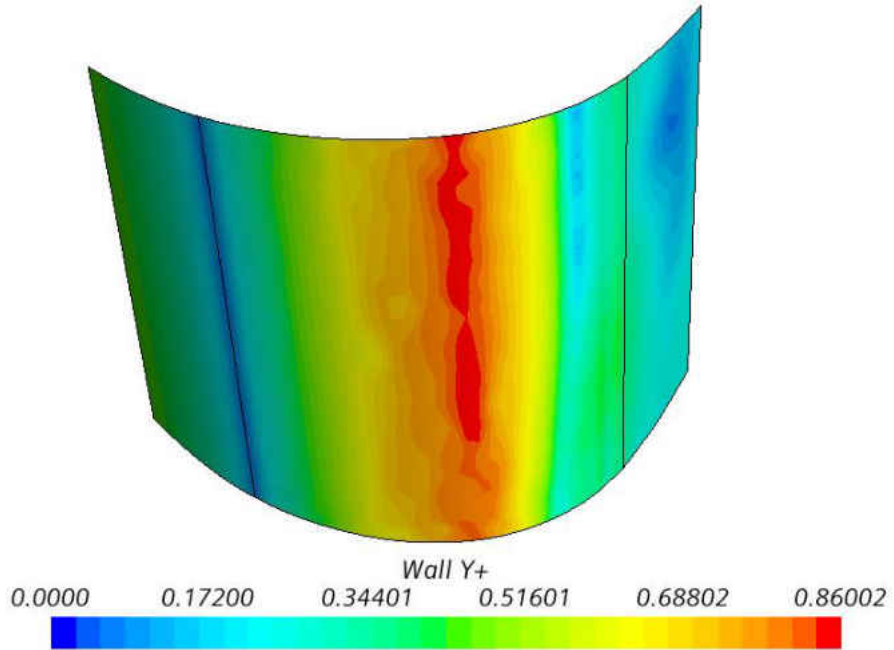
Figure 45: Nonrotating No SH Hole External Blade Surface Wall Y+ (EB RST)

Rotating without Shower Head Holes

Flow Field Analysis: Velocity

The domain velocity flow field for the rotating no shower head hole model is illustrated in Figures 46 and 47. The most apparent difference from this flow field, and the nonrotating one, is the intensity of the upstream fountain. For the rotating case the up-wash effect is less significant which is due to a reduced velocity in wall jets.

Figures 48 and 49 illustrate the jet velocity flow fields. The potential core velocity profiles are shown in Figures 50 and 51. Both models illustrate a uniform velocity profile at nozzle exit, with an increase in parabolicity in profile accompanied by a decrease in magnitude. These results agree with findings from studies conducted by Lamont et al. [3]. Lamont et al. [3] concluded that rotational forces influence the developing length of the potential core. The degree of parabolicity and decrease in magnitude is greater for the Lag EB K-Epsilon model than that of the EB RST model.
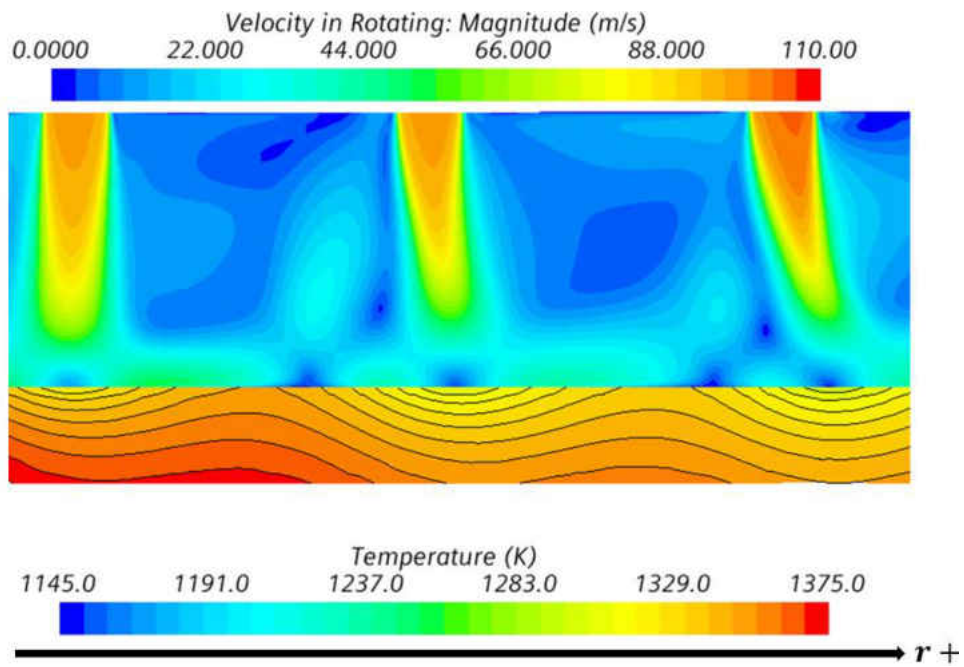
Figure 46: Rotating No SH Hole Domain Flow Field (Lag EB K-Epsilon)
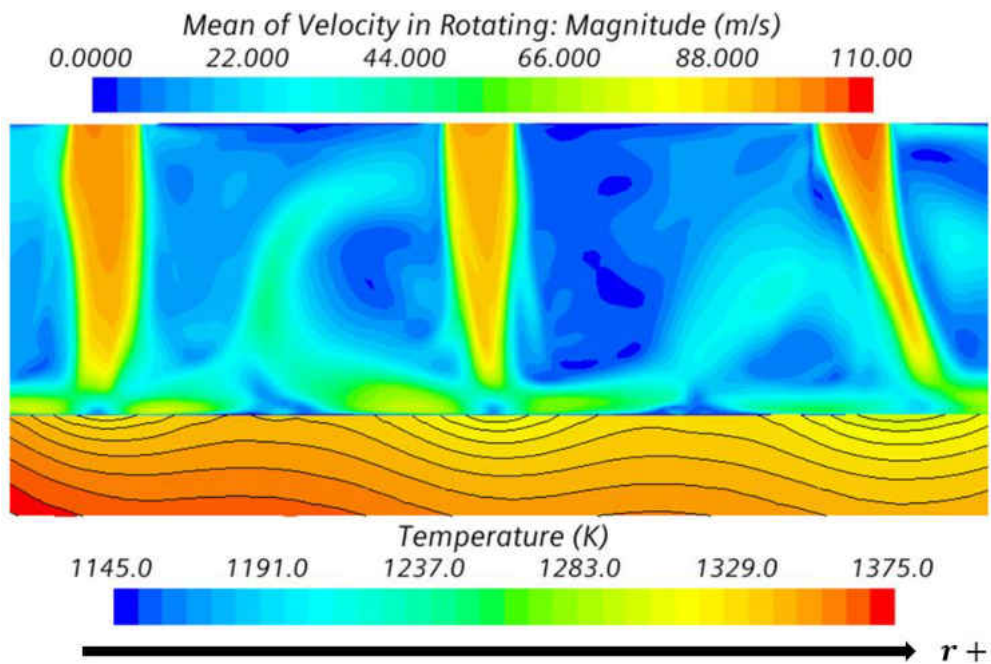
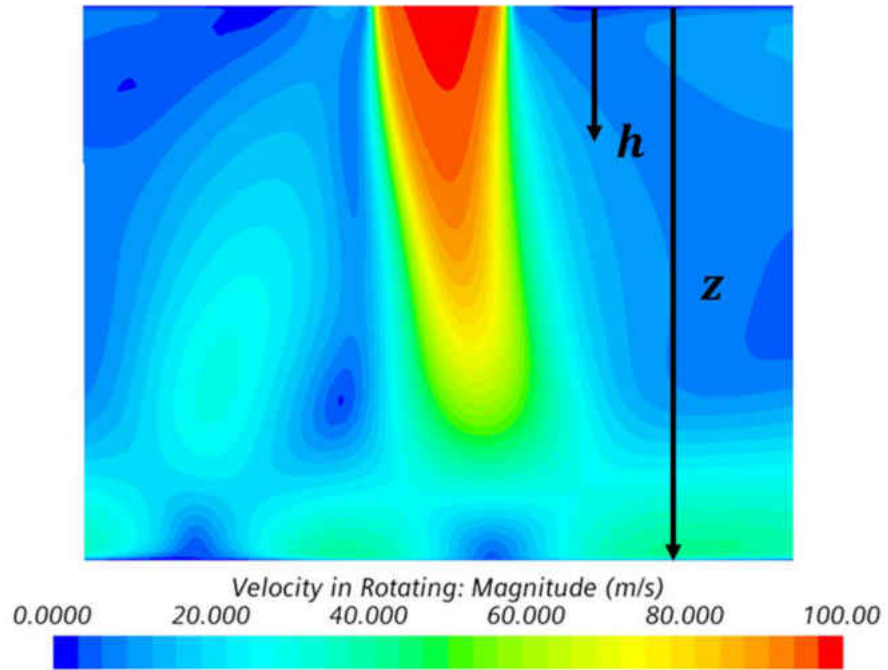

Figure 47: Rotating No SH Hole Domain Flow Field (EB RST)

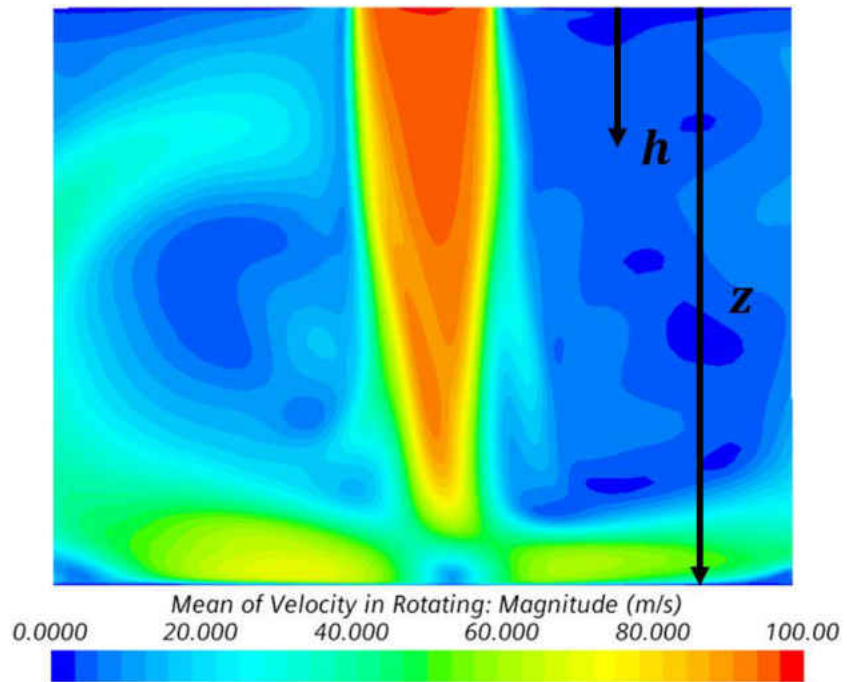*Figure 48: Rotating No SH Hole Jet Velocity Flow Field (Lag EB K-Epsilon)*

Figure 49: Rotating No SH Hole Jet Velocity Flow Field (EB RST)
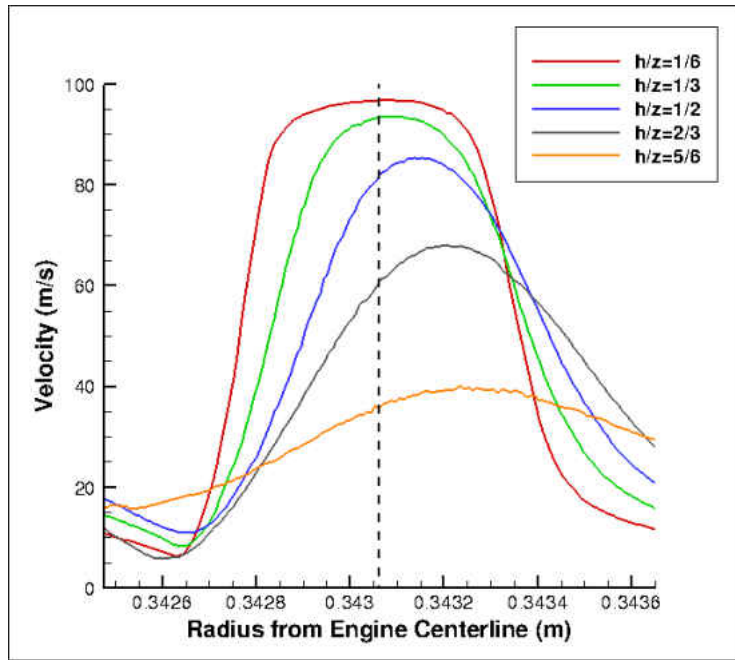
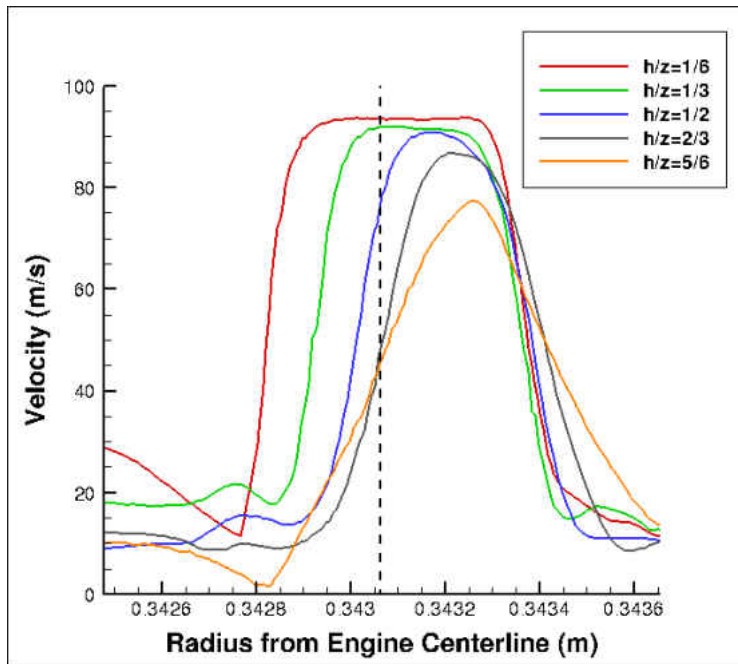*Figure 50: Rotating No SH Hole Potential Core Velocity Profiles (Lag EB K-Epsilon)*

Figure 51: Rotating No SH Hole Potential Core Velocity Profiles (EB RST)

Flow Field Analysis: Turbulent Kinetic Energy

The turbulent kinetic energy flow fields for the rotating no shower head hole model are shown in Figures 52 and 53. Analysis of the flow field illustrates maximum TKE at the stagnation region, for the Lag EB K-Epsilon model. The sources of the high TKE at stagnation are the same as was for the nonrotating case, plus an addition source. The additional source being that the vorticity tensor is being calculated at the wall, for the Lag EB K-Epsilon model, and far-away-from the wall for the EB RST model.

The TKE profile plots are given by Figures 54 and 55. Both turbulence models show that there is no region within the free jet that has zero TKE. In comparison to the nonrotating case were the potential core had zero TKE, it is assumed that rotational forces, which act perpendicular to the pressure force driving the jet, will cause the fluid elements within the potential core to rotate. In return increasing vorticity and TKE, which results in the decrease of jet velocity seen in the velocity flow field study.

The differences in magnitude of TKE for the entire free jet can be explained by the expected underprediction of turbulent dissipation for the Lag EB K-Epsilon model. The turbulence models show an opposite trend for magnitudes of TKE within the potential core. For the Lag EB K-Epsilon model, TKE within the core is at a minimum furthest away from the wall and maximum closest to the wall. The opposite holds true for the EB RST model. This behavior can be explained by the application of the vorticity tensor for each model. For the Lag EB K-Epsilon model as $\alpha \longrightarrow 0, f_w$ becomes the dominant term in the reduced stress transport equation. For

the EB RST model as $\alpha \longrightarrow 0, \phi_{ij}^h - \varepsilon_{ij}^h \longrightarrow 0$. Referring to the physics continua section which

stated that for the Lag EB K-Epsilon model the vorticity tensor is directly applied to the f_w

function and for the EB RST the vorticity tensor is directly applied ϕ_{ij}^h term. Therefore, the

effects of rotation will be more significant approaching the wall, for the Lag EB K-Epsilon model,

and less significant when approaching the wall for the EB RST model.
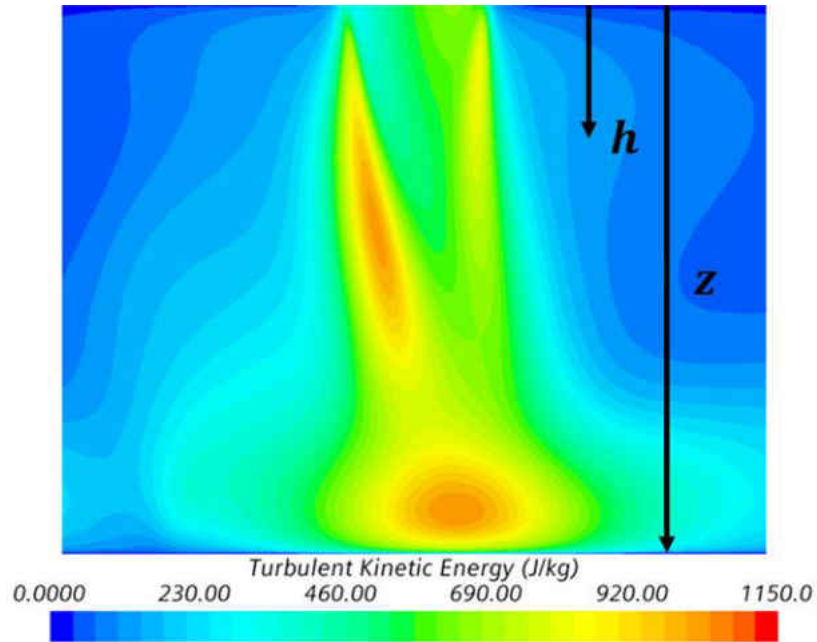
Figure 52: Rotating No SH Hole Jet TKE Flow Field (Lag EB K-Epsilon)
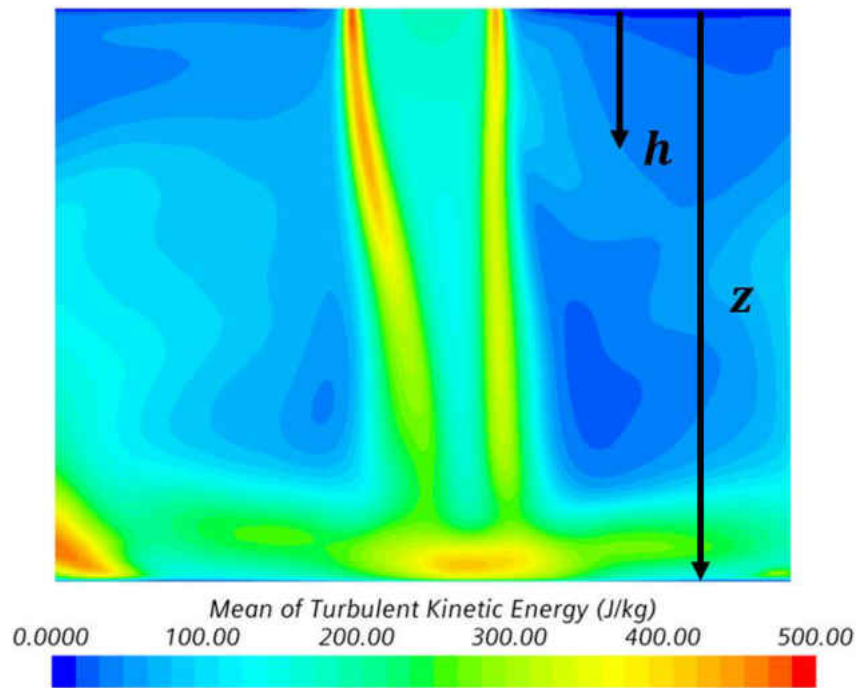
Figure 53: Rotating No SH Hole Jet TKE Flow Field (EB RST)
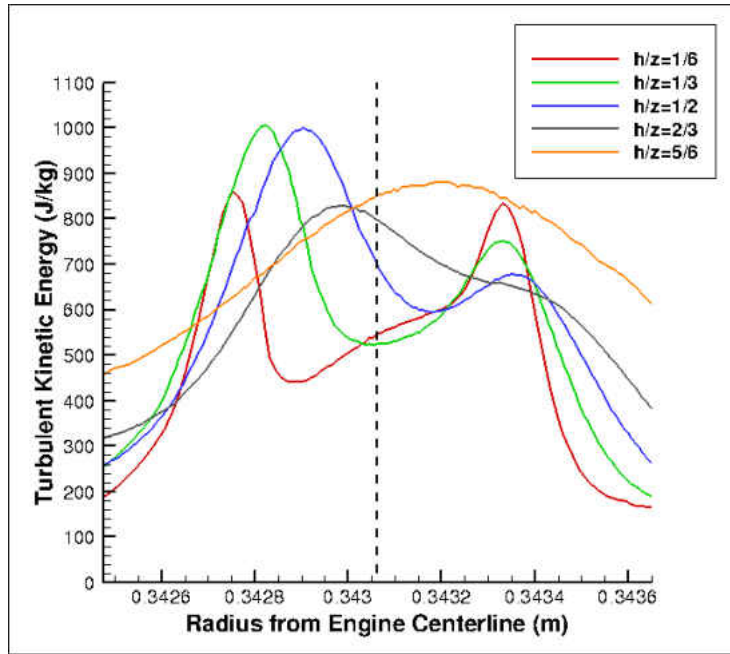
Figure 54: Rotating No SH Hole Jet TKE Profiles (Lag EB K-Epsilon)
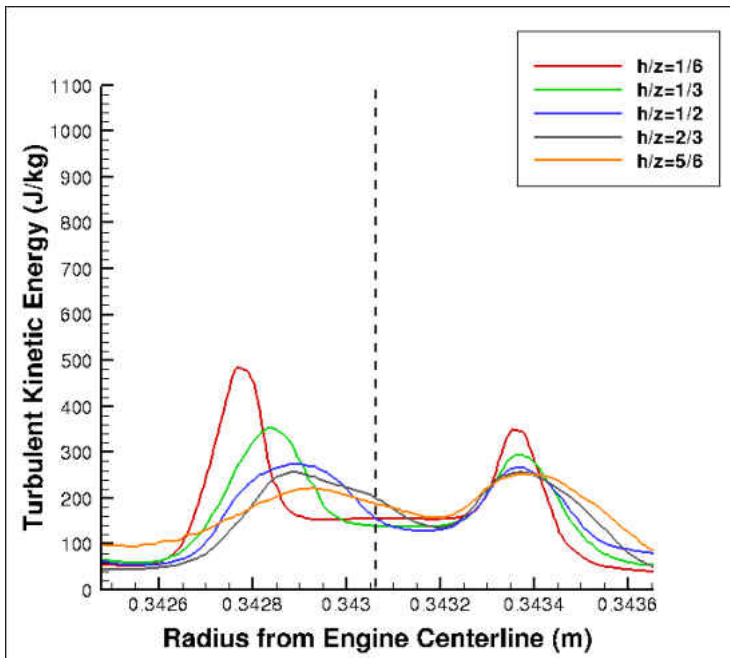
Figure 55: Rotating No SH Hole Jet TKE Profiles (EB RST)

Heat Transfer Analysis: Nusselt Number

Nusselt Number contour plots for the rotating no shower head hole model are illustrated in Figures 56 and 57. Inspection of the plots illustrates a significant decrease in magnitude, in comparison to the nonrotating cases, for both turbulence models. These findings agree with results of studies conducted by Iacovides et al. [4]. Iacovides et al. [4] concluded that rotational effects reduce maximum Nusselt Number peaks. This is due to decrease in incoming jet velocity, resulting in a decrease in impingement effectiveness. The Lag EB K-Epsilon model shows a similar elongated distribution, in comparison to the nonrotating case. The EB RST model shows a Nusselt Number maximum in three different locations, one towards the pressure side, one directly in line with the nozzle centerline and one towards the suction side. This is possibly due to the application of the Generalized Gradient Diffusion Hypothesis.

The spanwise Nusselt Number distribution through peak Nusselt Number is shown in Figure 58. Both turbulence models show an almost identical trend. With the only difference being that the Lag EB K-Epsilon model being shifted slightly radially outward. The magnitudes of maximum Nusselt Numbers were almost identical. Wall Y+ values for impingement surface were at optimal values and are illustrated in Figures 59 and 60.
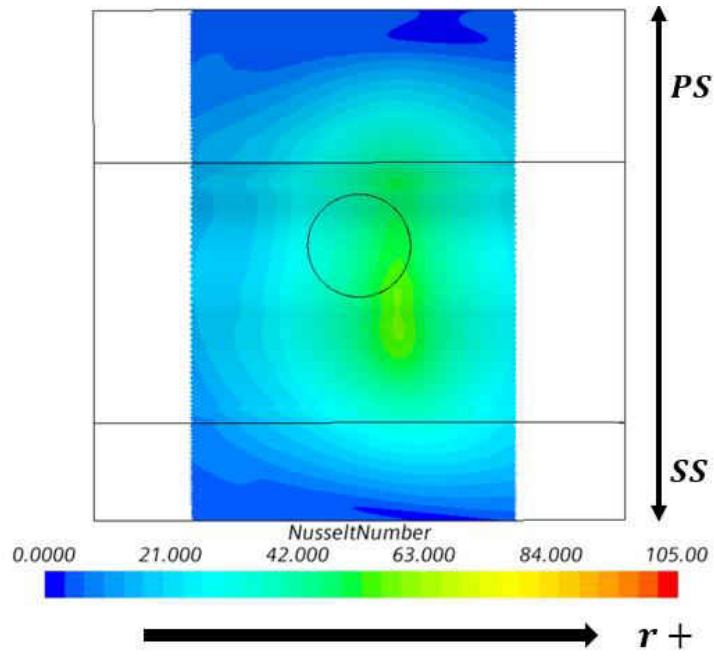
.

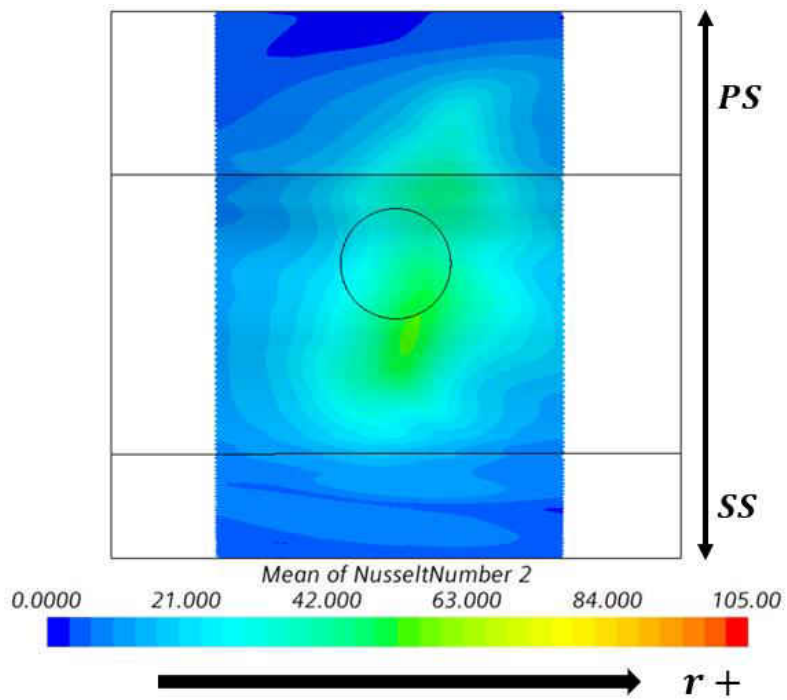*Figure 56: Rotating No SH Hole Nusselt Number (Lag EB K-Epsilon)*

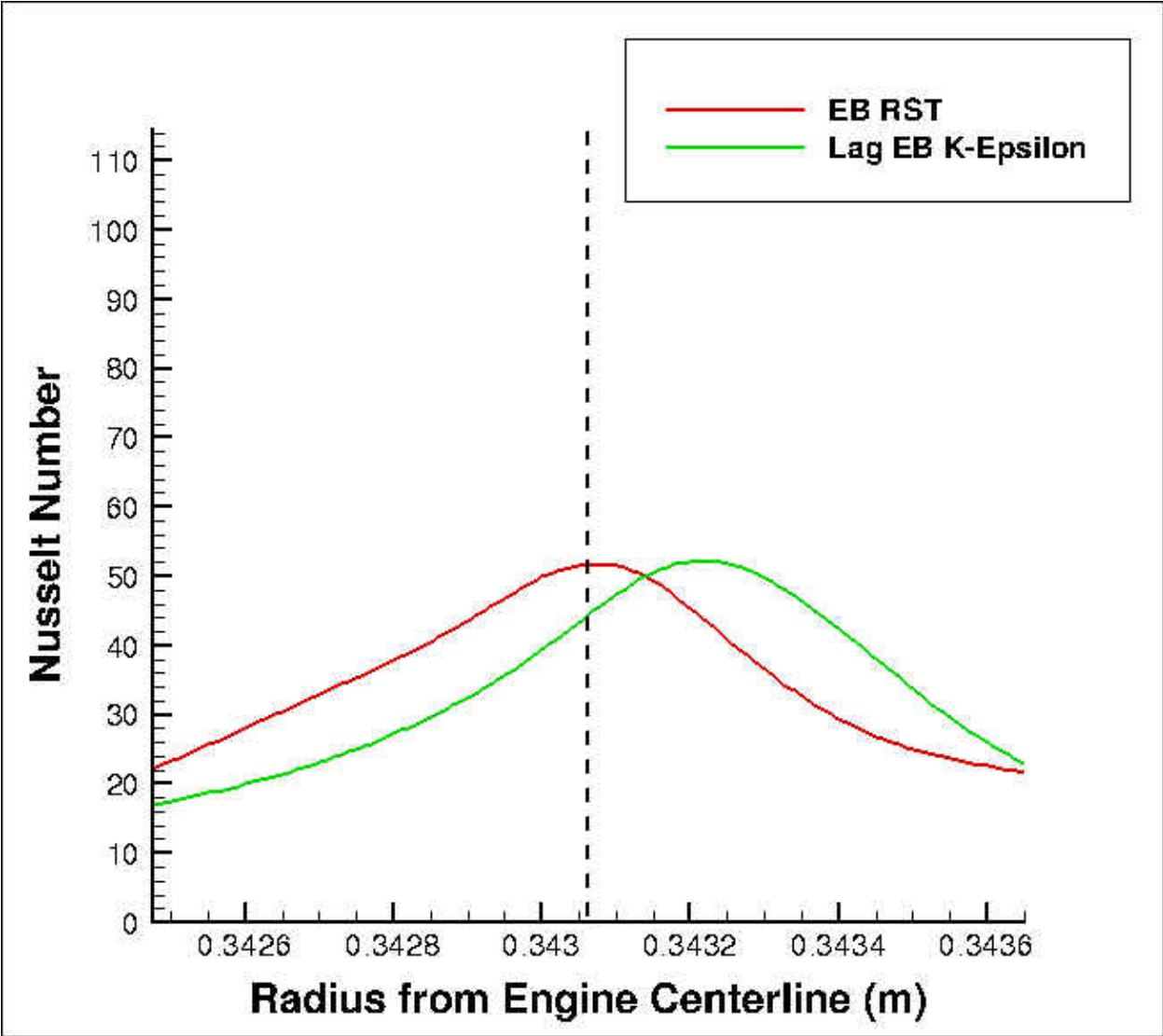*Figure 57: Rotating No SH Hole Nusselt Number (EB RST)*

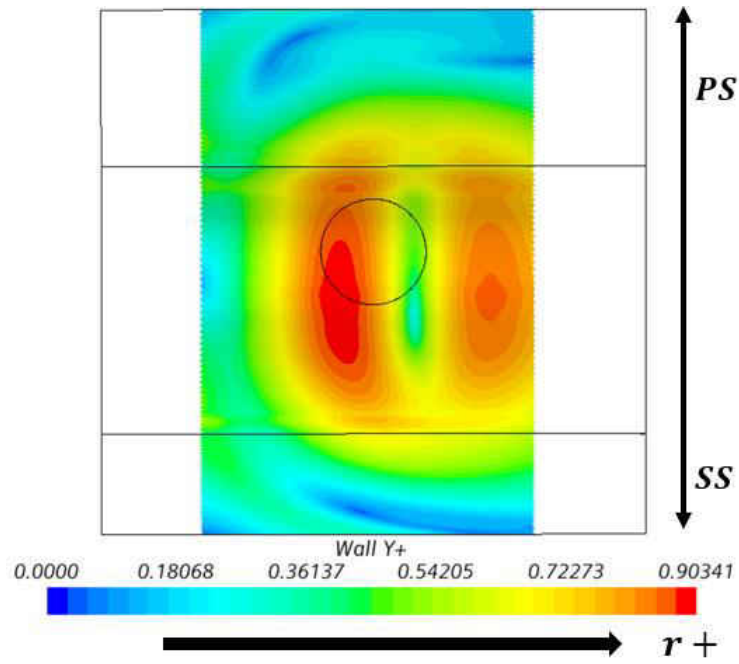*Figure 58: Rotating No SH Hole Spanwise Nusselt Distribution*

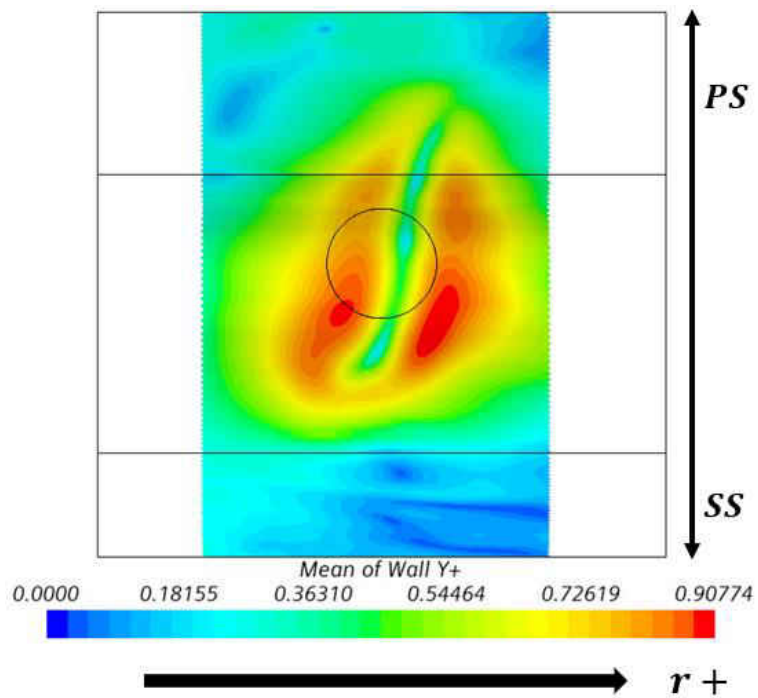*Figure 59: Rotating No SH Hole Impingement Wall Y+ (Lag Eb K-Epsilon)*

Figure 60: Rotating No SH Hole Impingement Wall Y+ (EB RST)

69

External Blade Temperature

The external blade surface temperature profiles are illustrated in Figure 61. The temperature profiles for each turbulence model are significantly different. The EB RST model shows a maximum temperature towards the suction side and a minimum temperature towards the pressure side. While the Lag EB K-Epsilon model shows an almost constant temperature across the entire leading-edge surface. A flow field study on the external surface of the blade is required to understand the differences in temperature profiles. External blade surface Wall Y+ was at optimal values, Figures 62 and 63.
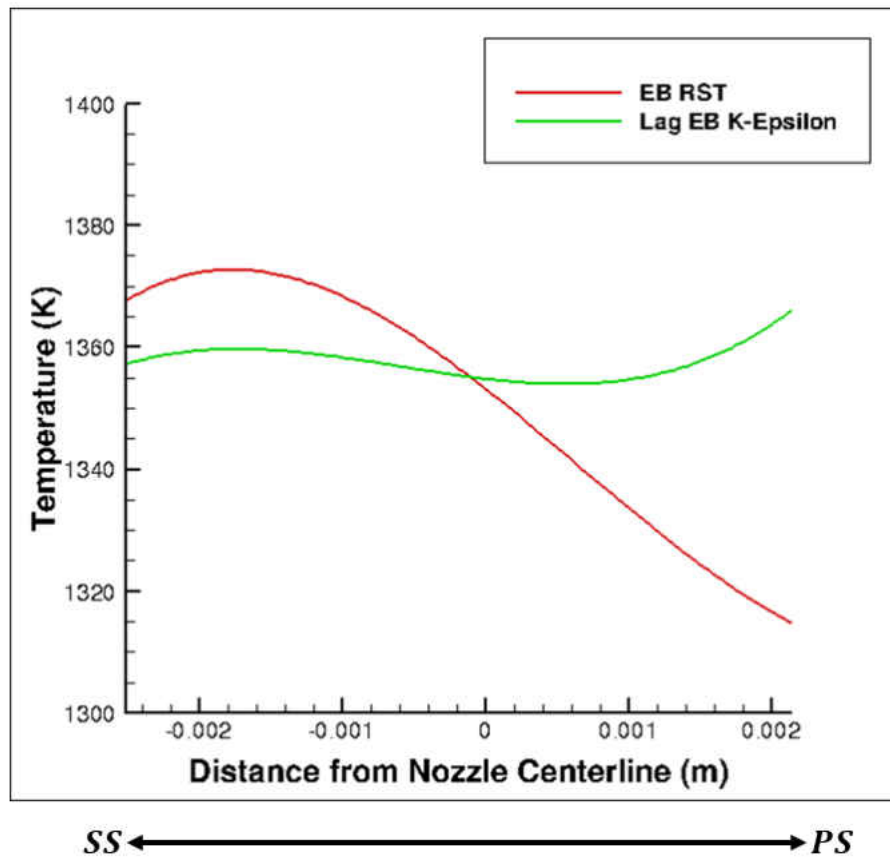

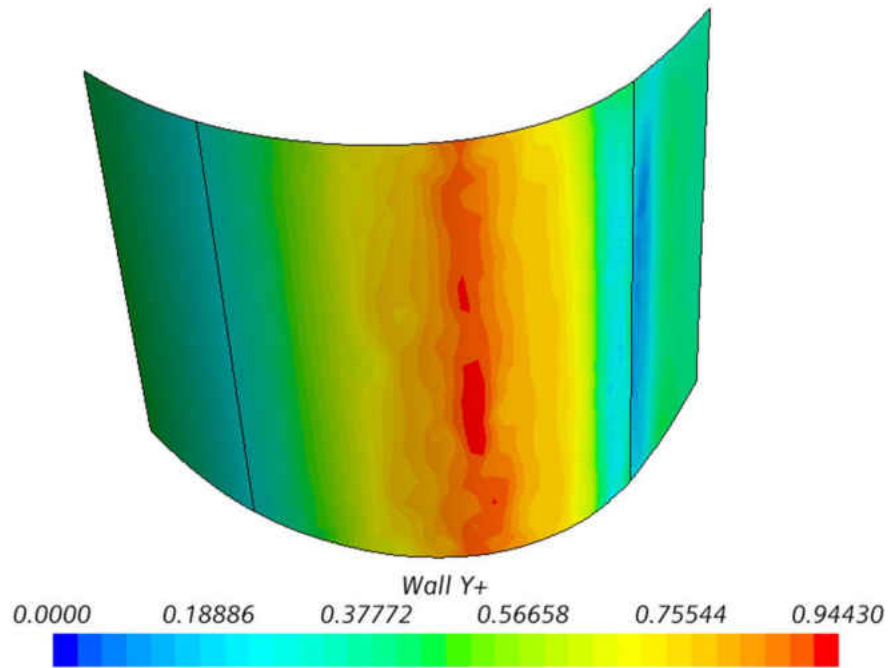*Figure 61: Rotating No SH Hole External Blade Temperature Profile*

70

Wall Y+

0.0000   0.18886   0.37772   0.56658   0.75544   0.94430

Figure 62: Rotating No SH Hole External Blade Surface Wall Y+ (Lag EB K-Epsilon)

Wall Y+

0.0000   0.17750   0.35500   0.53250   0.71000   0.88750
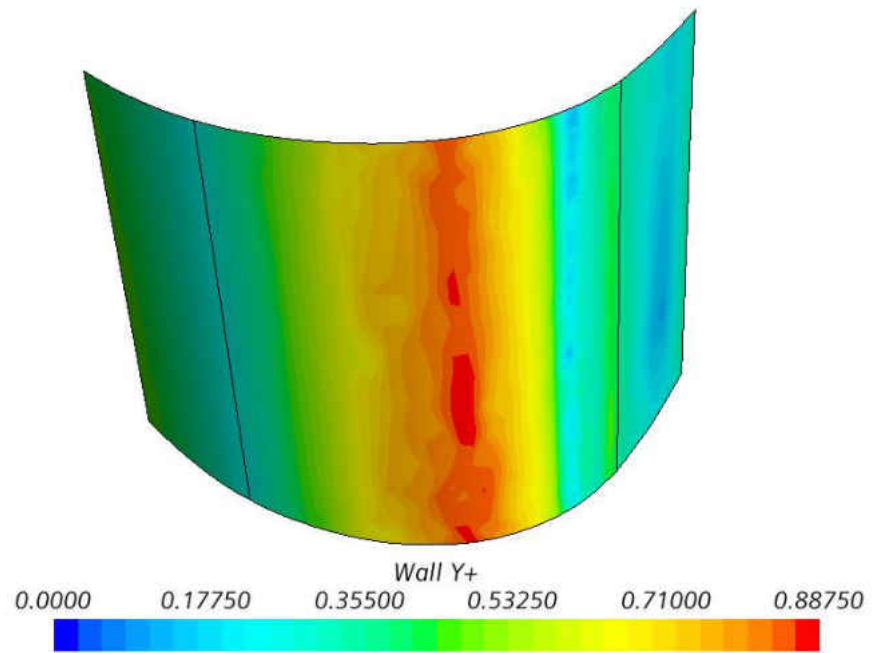
Figure 63: Rotating No SH Hole External Blade Surface Wall Y+ (EB RST)

71

<u>Nonrotating with Shower Head Holes</u>

Flow Field Analysis: Velocity

Figures 64 and 65 illustrate the domain velocity flow field for the nonrotating shower head hole model. Both turbulence models illustrate almost identical flow fields. The jets are completely undisturbed due to the extraction of wall jets through the shower head holes. Figures 66 and 67 show the jet velocity flow field. The EB RST model shows some slight deformation of the jet. An inspection from a view perpendicular to the spanwise view is used to explain this behavior, Figures 68 and 69. The dashed line represents to nozzle axis.

From analysis of the top view it is seen that the jet is influenced towards the suction side for both models, while the EB RST model is affected more. The influence on the jet's trajectory can be explained by the pressure gradient on the external surface of the blade. The suction side has a lower pressure. Therefore, the jet will tend to impinge towards the suction side because the pressure gradient is greater towards this side of the impingement surface.

Figures 70 and 71 illustrate the potential core velocity profiles in the spanwise view and Figure 72 illustrates the velocity profile in the perpendicular plane, chordwise view. Chordwise plane velocity profiles were not analyzed for the Lag EB K-Epsilon model because this model showed less jet deformation. The spanwise plane potential core velocity profiles for the Lag EB K-Epsilon model illustrate a uniform profile with constant magnitude up until $h/z = 5/6$, where a slight decrease in velocity is observed. The decrease in velocity is due to the jet making its

entrance into the stagnation region. The jet is also symmetric about the nozzle axis in the spanwise direction.

The chordwise plane velocity profile, for the EB RST model, shows identical behavior as that of the spanwise plane velocity profile, for the Lag EB K-Epsilon model, besides the shift towards the suction side. The profiles illustrate the same uniform profile with constant magnitude up until $h/z = 5/6$. The decrease in magnitude at $h/z = 5/6$ is also the same.
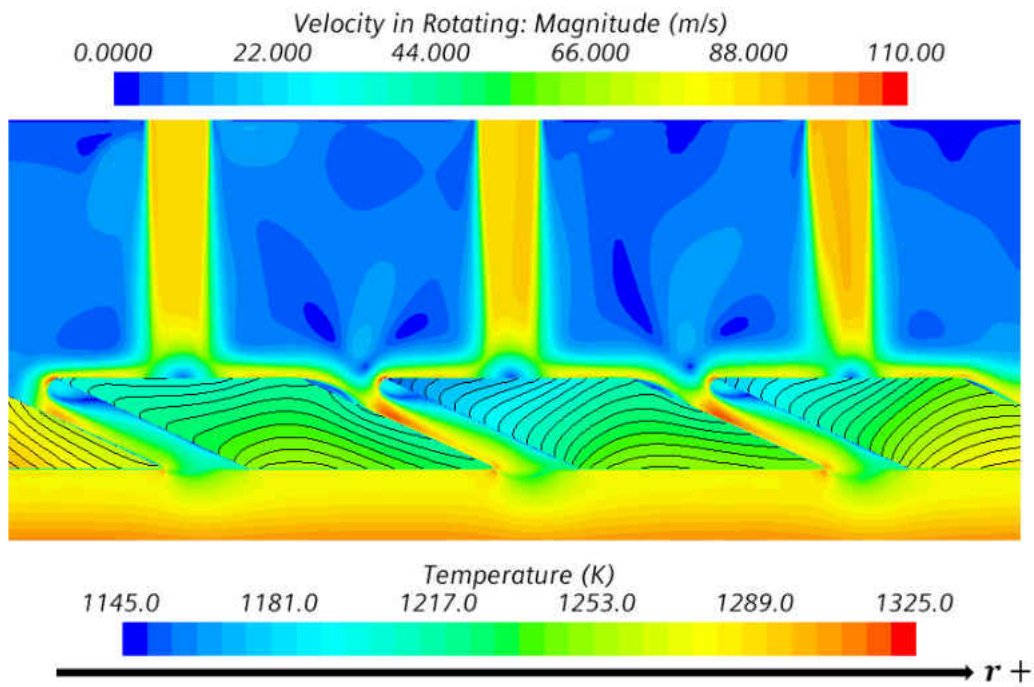
Figure 64: Nonrotating SH Hole Domain Flow Field (Lag EB K-Epsilon)
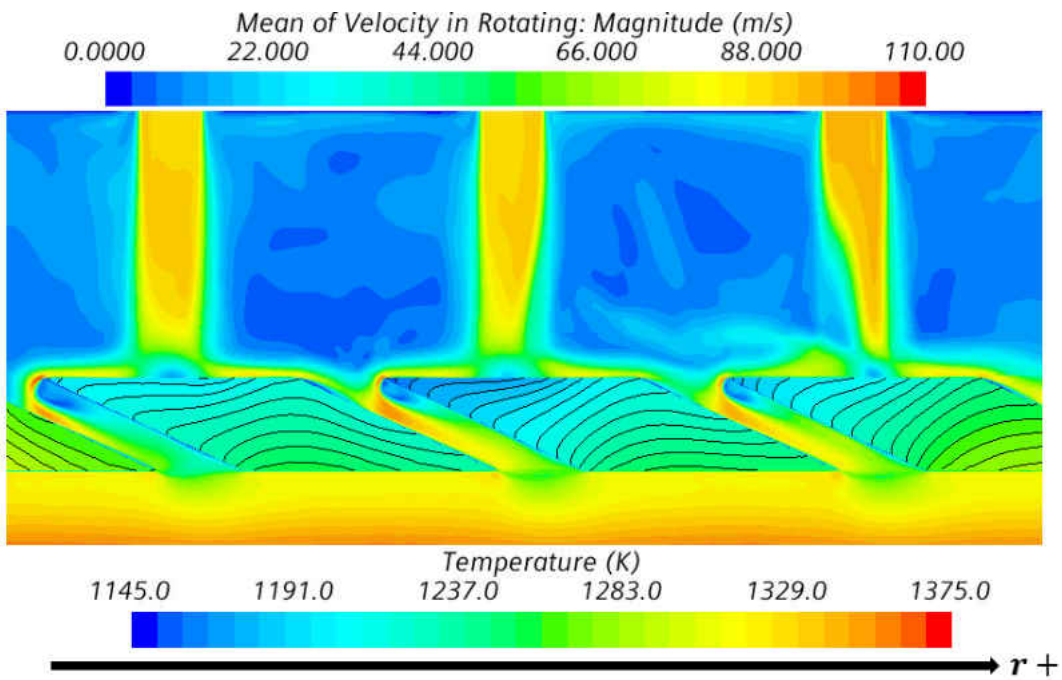
Figure 65: Nonrotating SH Hole Domain Flow Field (EB RST)
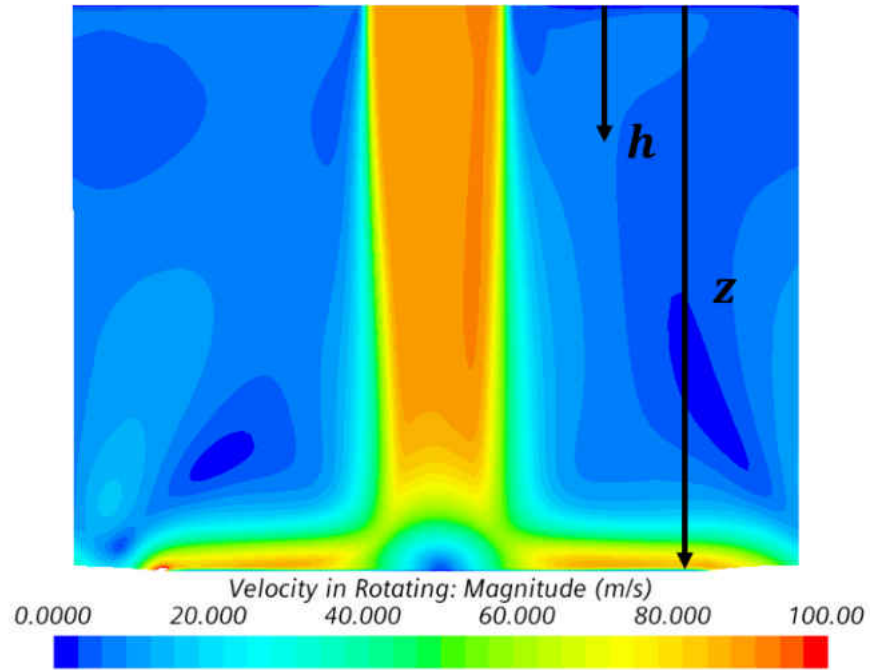
Figure 66: Nonrotating SH Hole Jet Flow Field (Lag EB K-Epsilon)
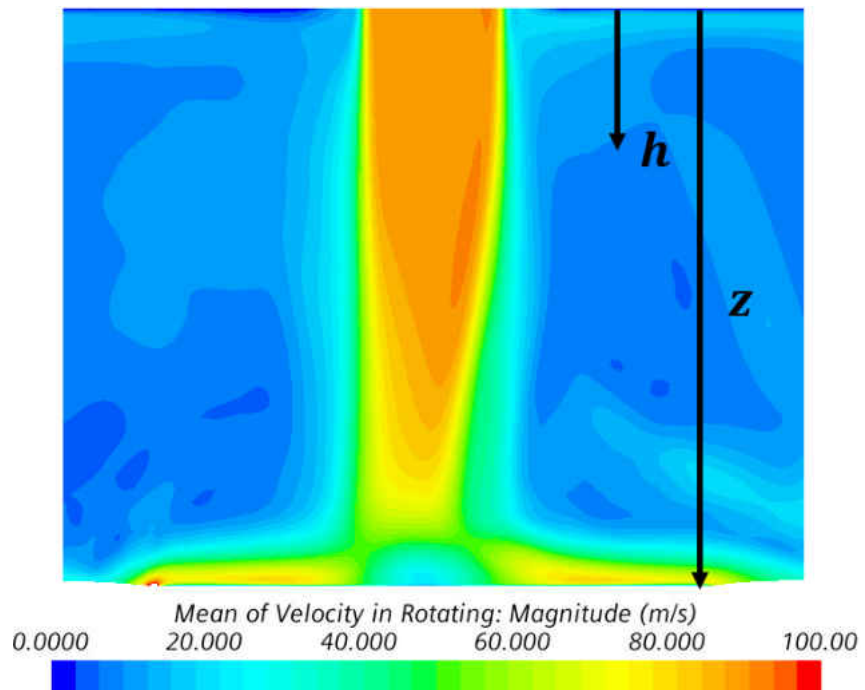

Figure 67: Nonrotating SH Hole Jet Flow Field (EB RST)
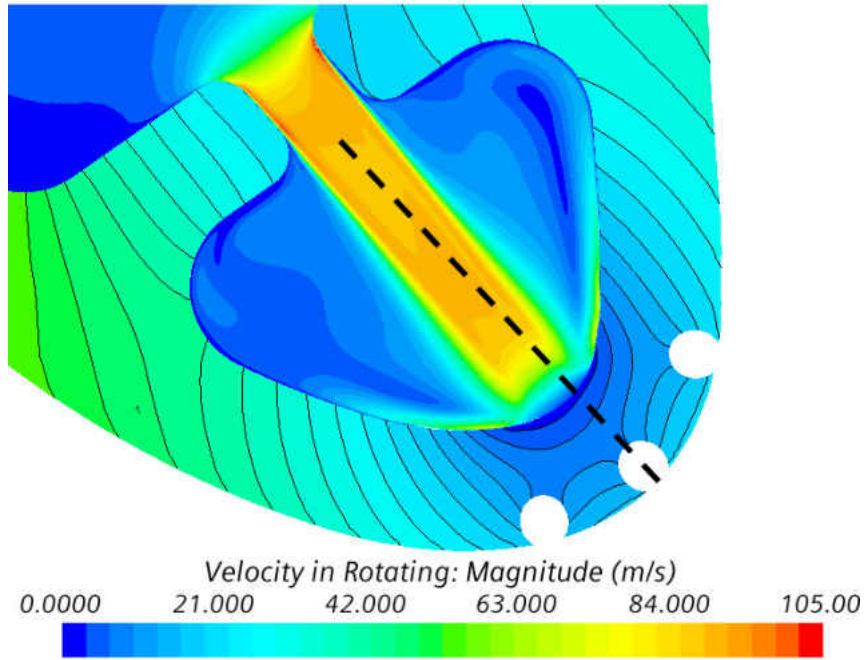
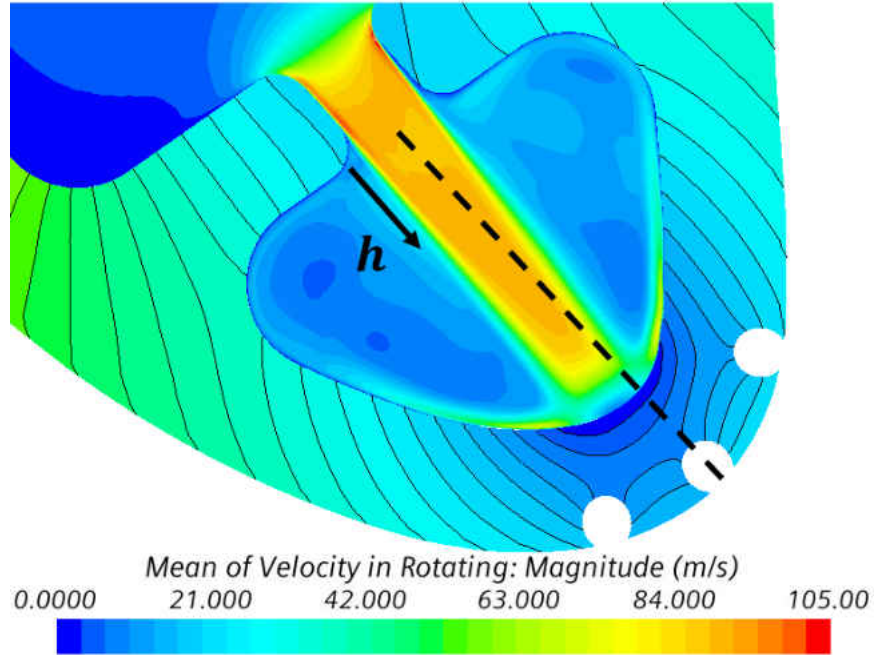*Figure 68: Nonrotating SH Hole Chordwise Plane Velocity Flow Field (Lag EB K-Epsilon)*

Figure 69: Nonrotating SH Hole Chordwise Plane Velocity Flow Field (EB RST)
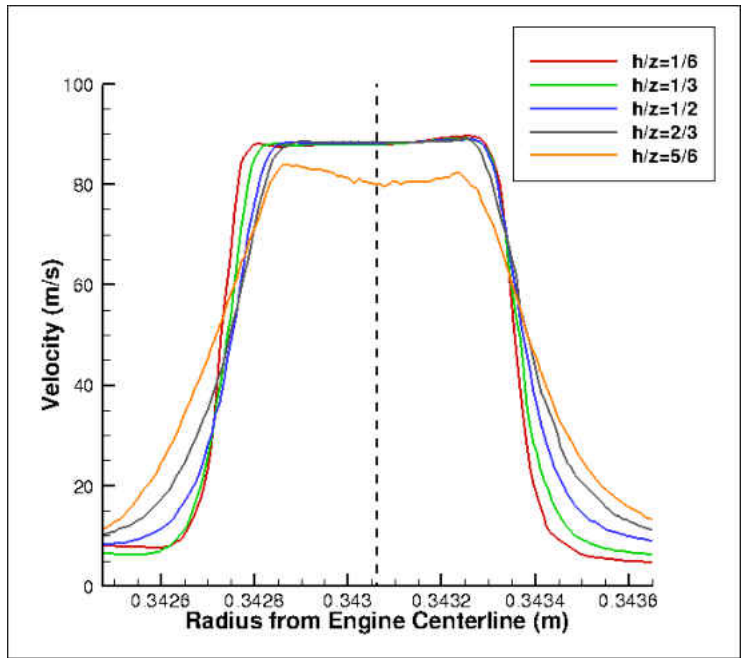
Figure 70: Nonrotating SH Hole Spanwise Plane Potential Core Velocity Profiles (Lag EB K-Epsilon)
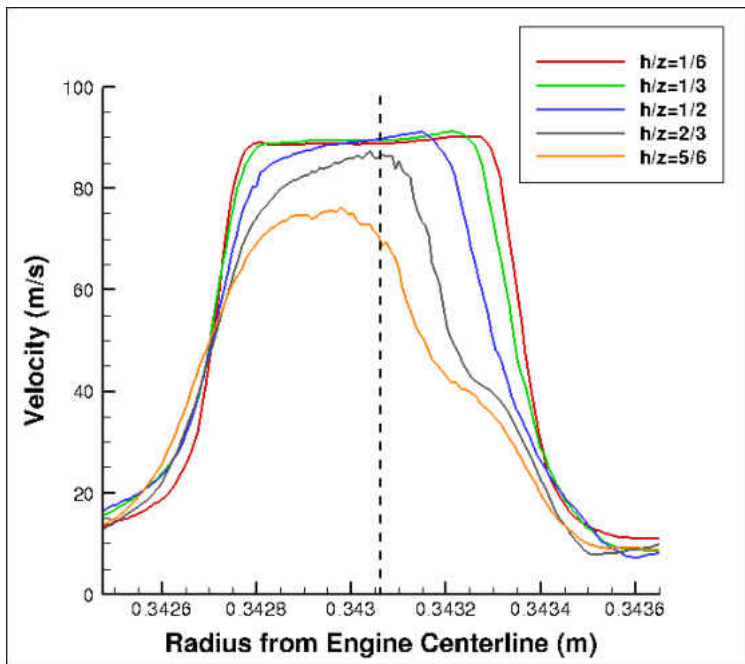

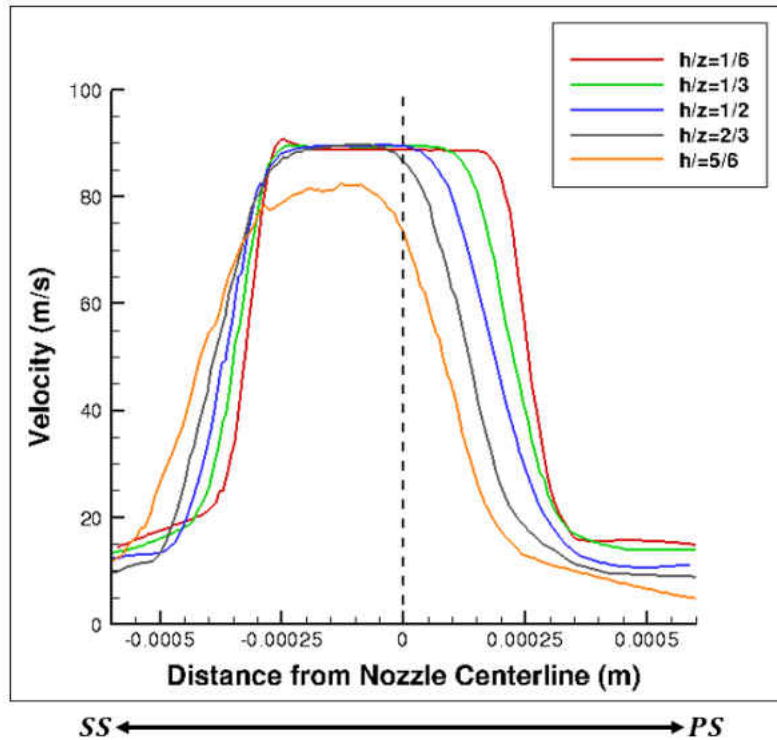*Figure 71: Nonrotating SH Hole Spanwise Plane Potential Core Velocity Profiles (EB RST)*

77

Figure 72: Nonrotating SH Hole Chordwise Plane Potential Core Velocity Profiles (EB RST)

Flow Field Analysis: Turbulent Kinetic Energy

The spanwise plane jet TKE flow field for the nonrotating shower head holes model is illustrated in Figures 73 and 74. The TKE flow field for the EB RST model shows that the shear layer, towards the impingement surface, has shifted into the spanwise plane. This is a result of the jet being influenced by the pressure gradient from the external suction side of the blade. Figures 75 and 76 show the TKE flow field in the chordwise plane. Analysis of the flow fields show that for the Lag EB K-Epsilon model the shear layer never crosses the nozzle centerline, or the alternatively the spanwise plane. The chordwise plane TKE flow field for the EB RST model

clearly illustrates the shear layer on the pressure side crossing over the nozzle centerline, or spanwise plane, as the jet approaches the impingement surface.

Figures 77 and 78 show the spanwise plane TKE profiles for the free jet region of the nonrotating shower head holes model. Figure 79 illustrates the chordwise plane TKE profiles for the EB RST model. The spanwise plane profiles for both turbulence models show identical trends, up to $h/z = 2/3$ for the EB RST model, with zero TKE within the potential core of the jet with symmetric shear layers about the nozzle axis. The chordwise plane TKE profiles for the EB RST model shows a potential core with zero TKE. The main difference between both turbulence models is in the magnitude of TKE which can be explained by the expected overprediction of TKE for the Lag EB K-Epsilon model.
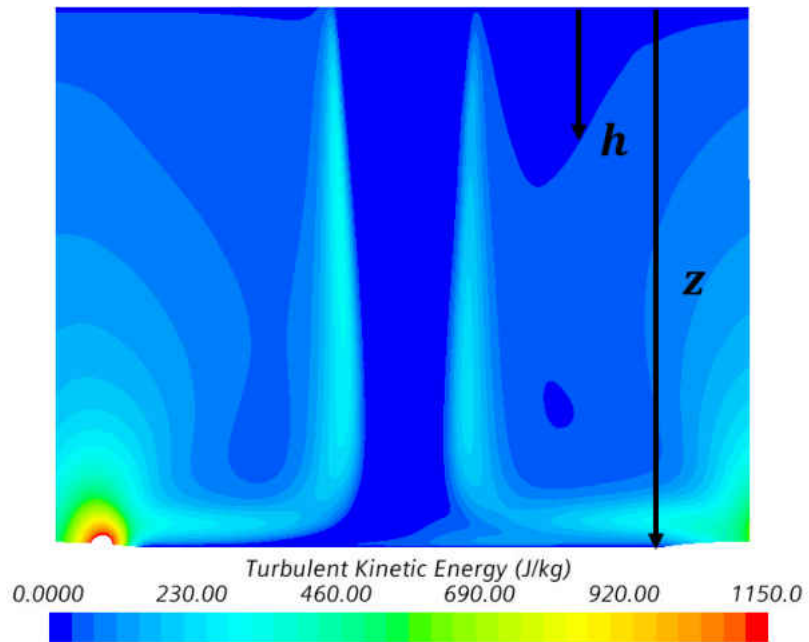
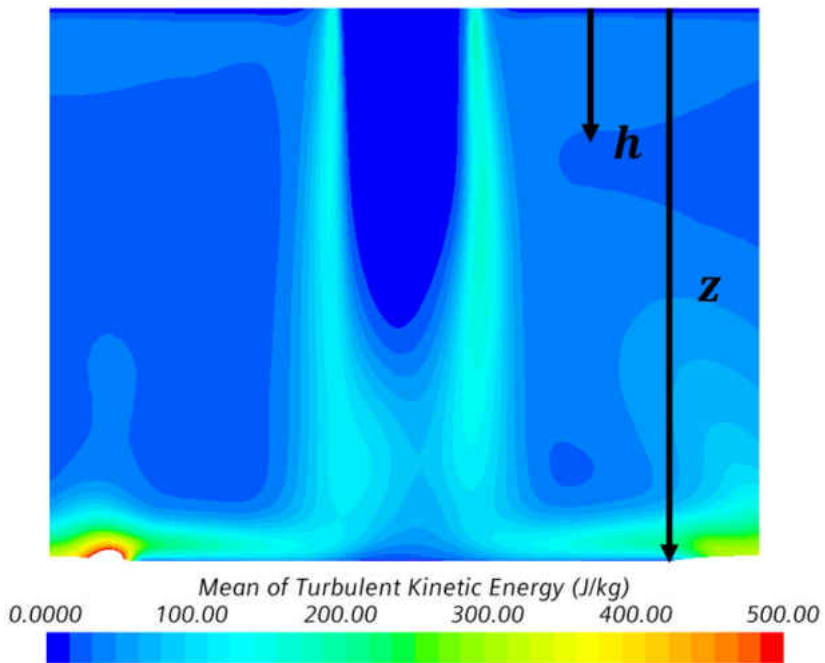*Figure 73: Nonrotating SH Hole Jet TKE Flow Field (Lag EB K-Epsilon)*

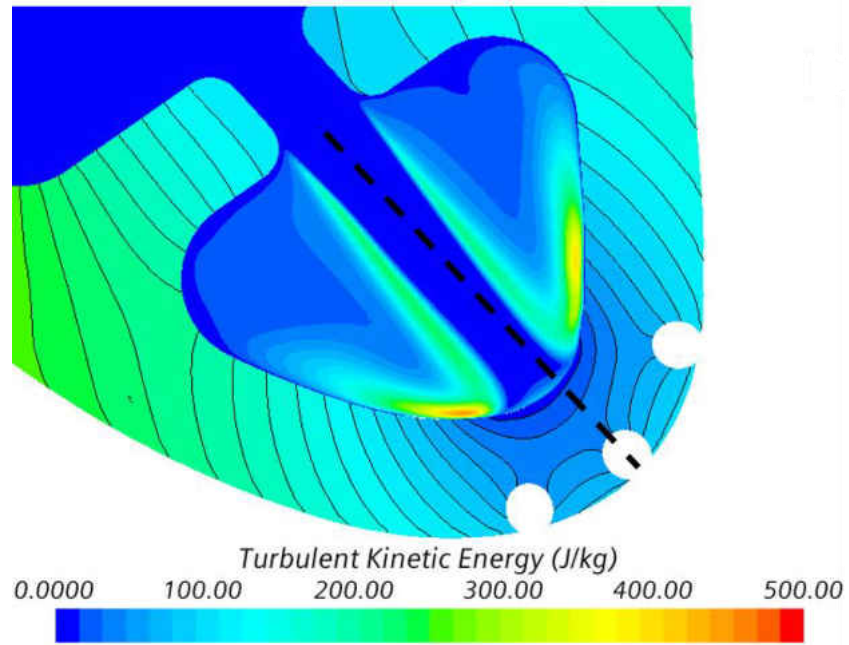*Figure 74: Nonrotating SH Hole Jet TKE Flow Field (EB RST)*

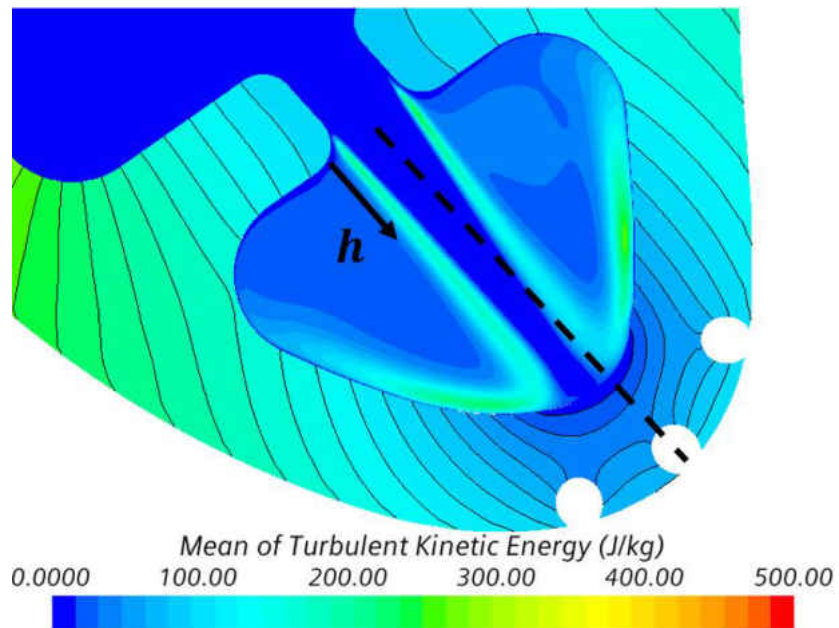*Figure 75: Nonrotating SH Hole Chordwise Plane TKE Flow Field (Lag EB K-Epsilon)*

Figure 76: Nonrotating SH Hole Chordwise Plane TKE Flow Field (EB RST)
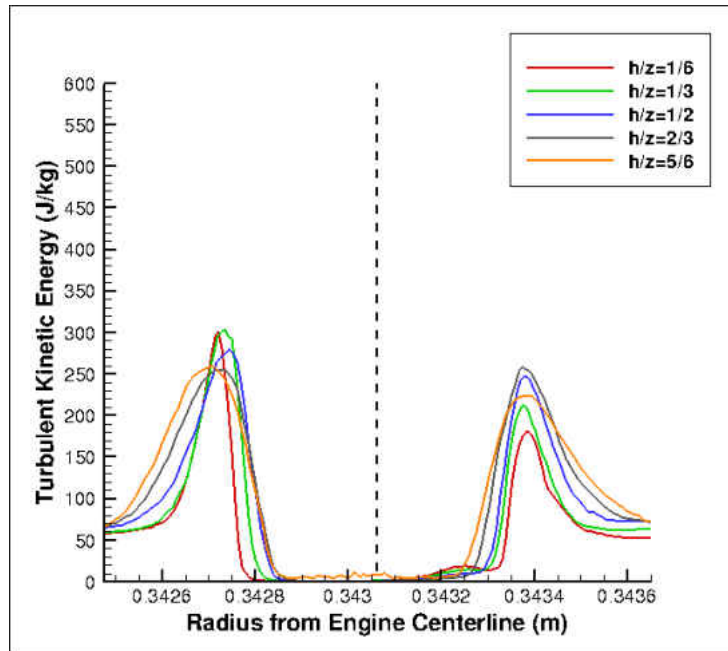
81

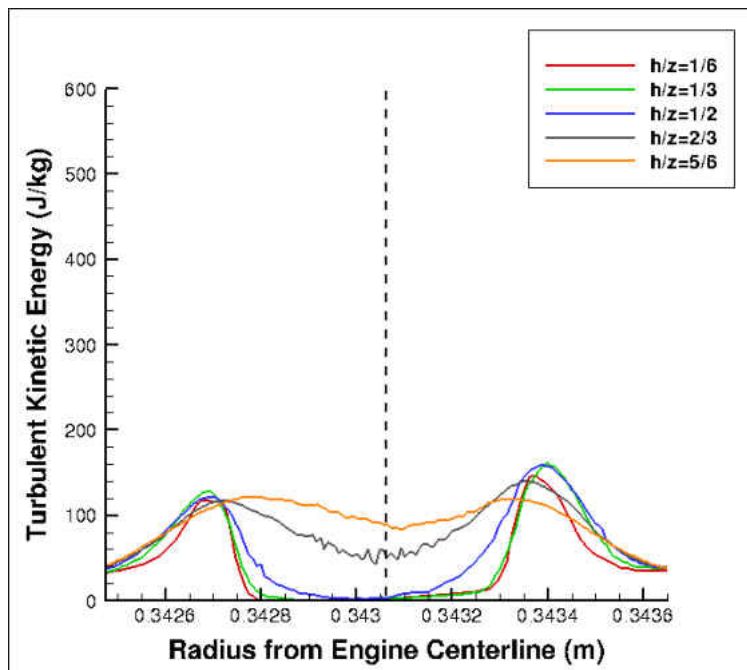*Figure 77: Nonrotating SH Hole Spanwise Plane Jet TKE Profiles (Lag EB K-Epsilon)*

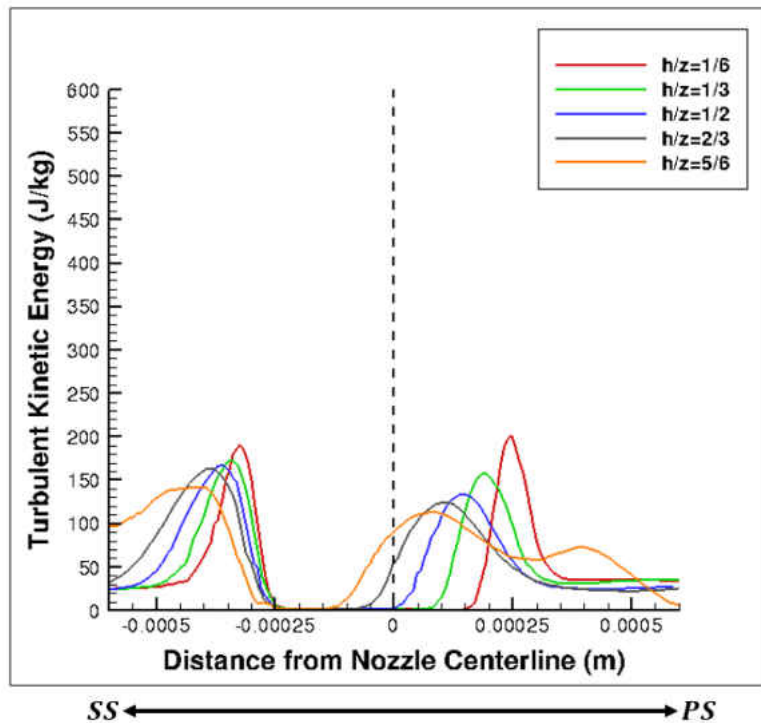*Figure 78: Nonrotating SH Hole Spanwise Plane Jet TKE Profiles (EB RST)*

Figure 79: Nonrotating SH Hole Chordwise Plane Jet TKE Profiles (EB RST)

Heat Transfer Analysis: Nusselt Number

The Nusselt Number contour plots for the nonrotating shower head holes model are illustrated in Figures 80 and 81. Both turbulence models illustrate a maximum Nusselt Number towards the suction side of the impingement surface. This can be explained by the suction side pressure gradient influencing the trajectory of the jet.

The spanwise Nusselt Number distribution is shown in Figure 82. The two turbulence models are in fair agreement with one another with respect to trend but are in good agreement with respect to magnitude. The EB RST model shows a Nusselt maximum which is shifted slightly further downstream than that of the Lag EB K-Epsilon model. The discrepancy in location of

maximum Nusselt Number is possibly due to the application of the Generalized Gradient

Diffusion Hypothesis for the EB RST model. The flow field analysis for both turbulence models

shows an equivalent impinging jet velocity with zero TKE at stagnation. Implying that the only

significant difference being the method of diffusion. The impingement surface Wall Y+ was held
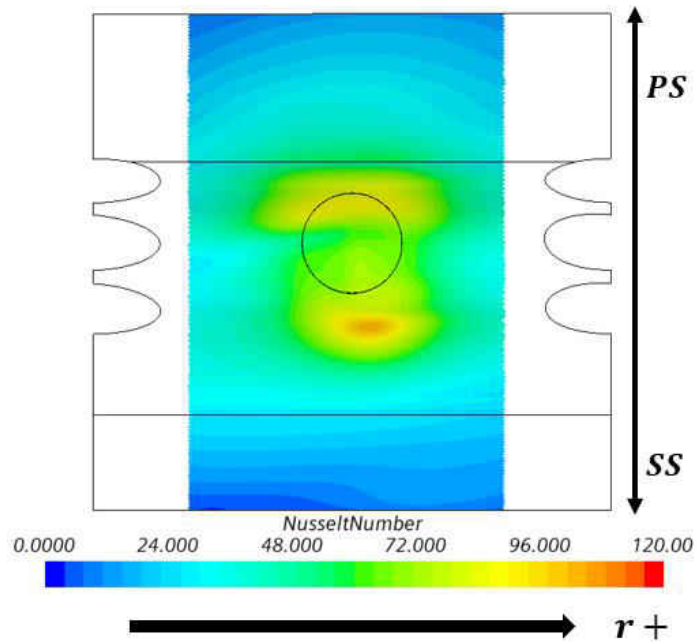
to optimal values, Figures 83 and 84.

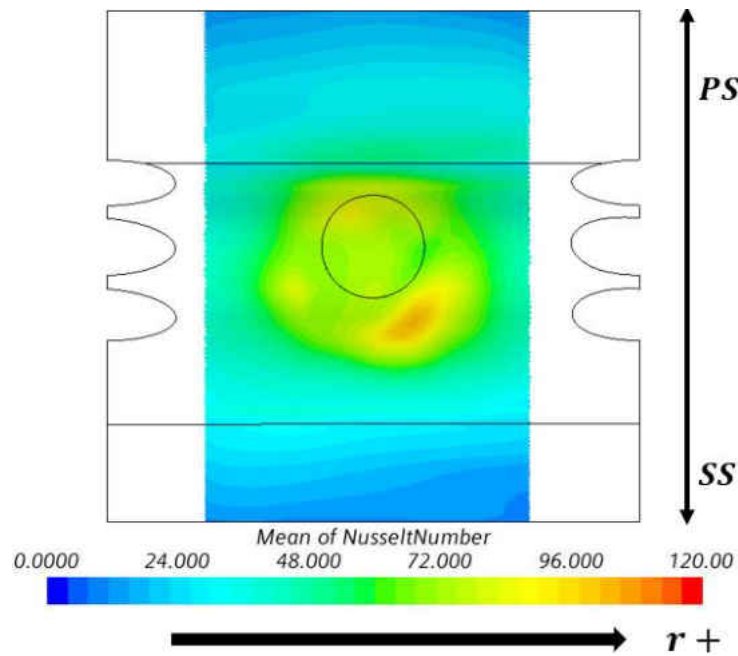*Figure 80: Nonrotating SH Hole Nusselt Number (Lag EB K-Epsilon)*

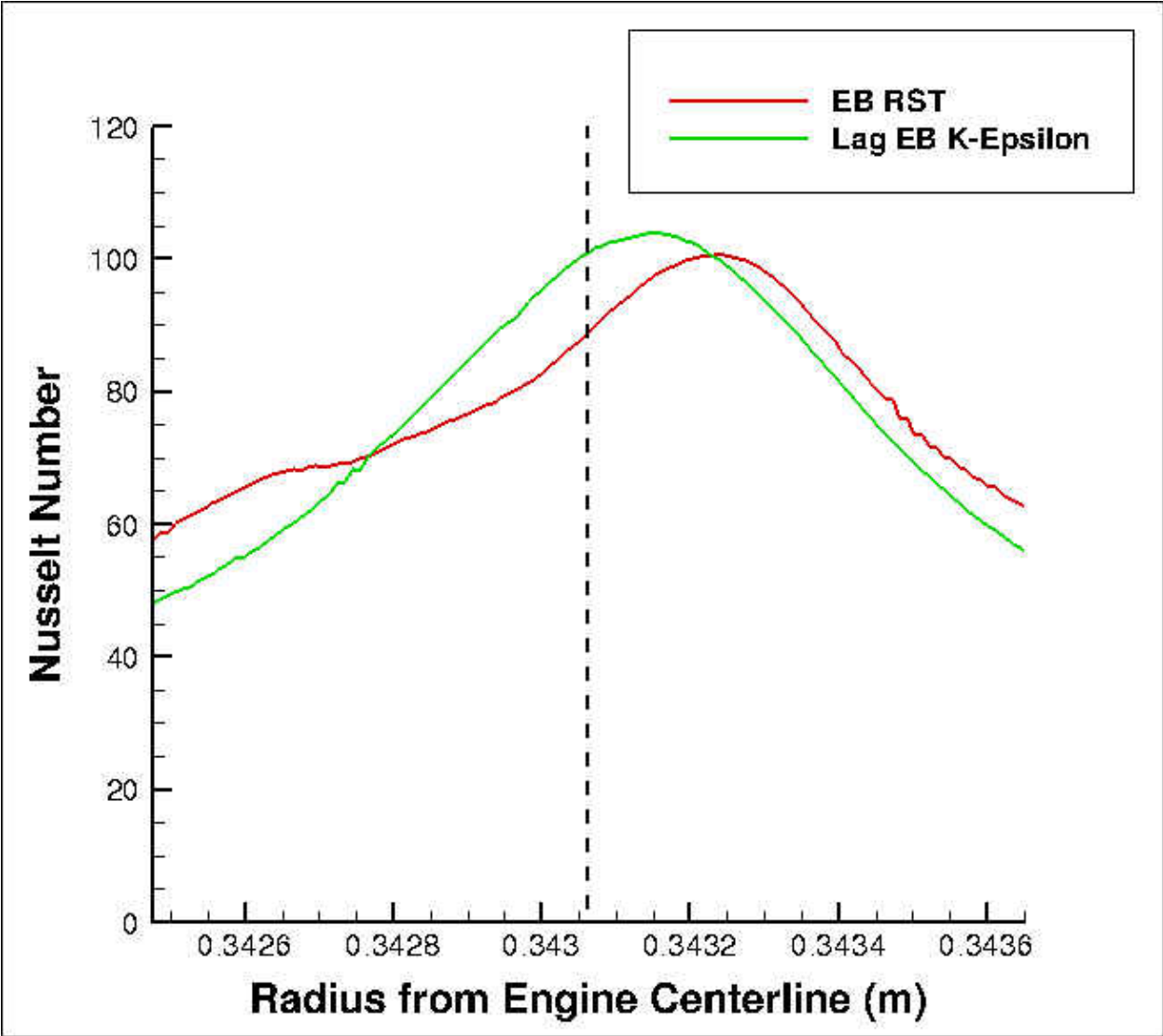*Figure 81: Nonrotating SH Hole Nusselt Number (EB RST)*

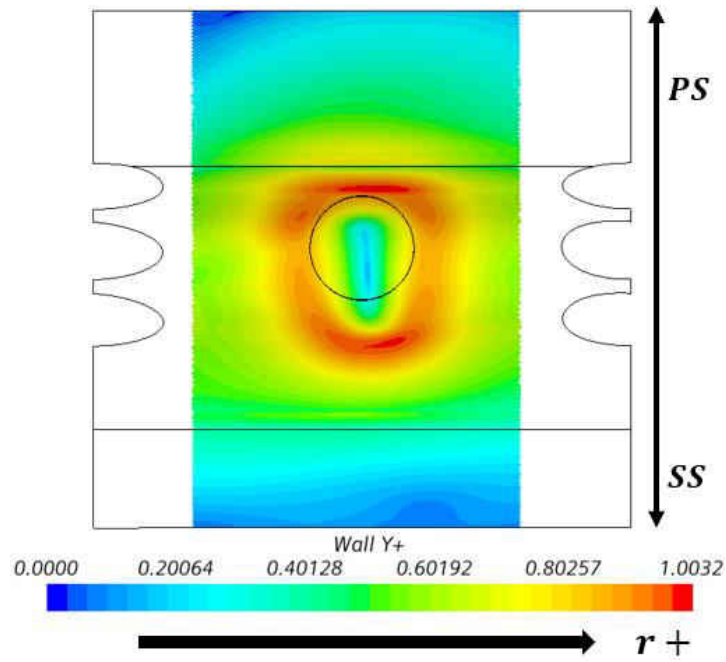*Figure 82: Nonrotating SH Hole Spanwise Nusselt Distribution*

Figure 83: Nonrotating SH Hole Impingement Wall Y+ (Lag EB K-Epsilon)
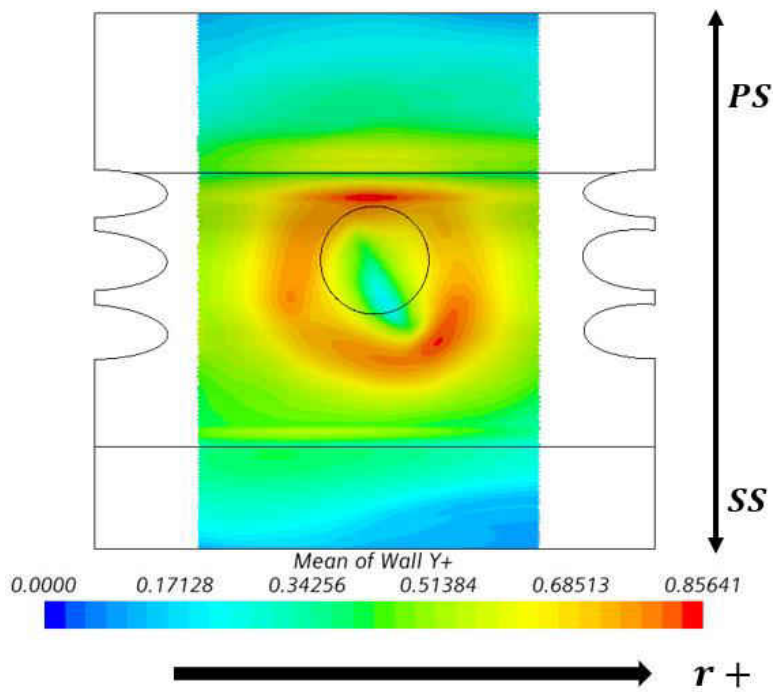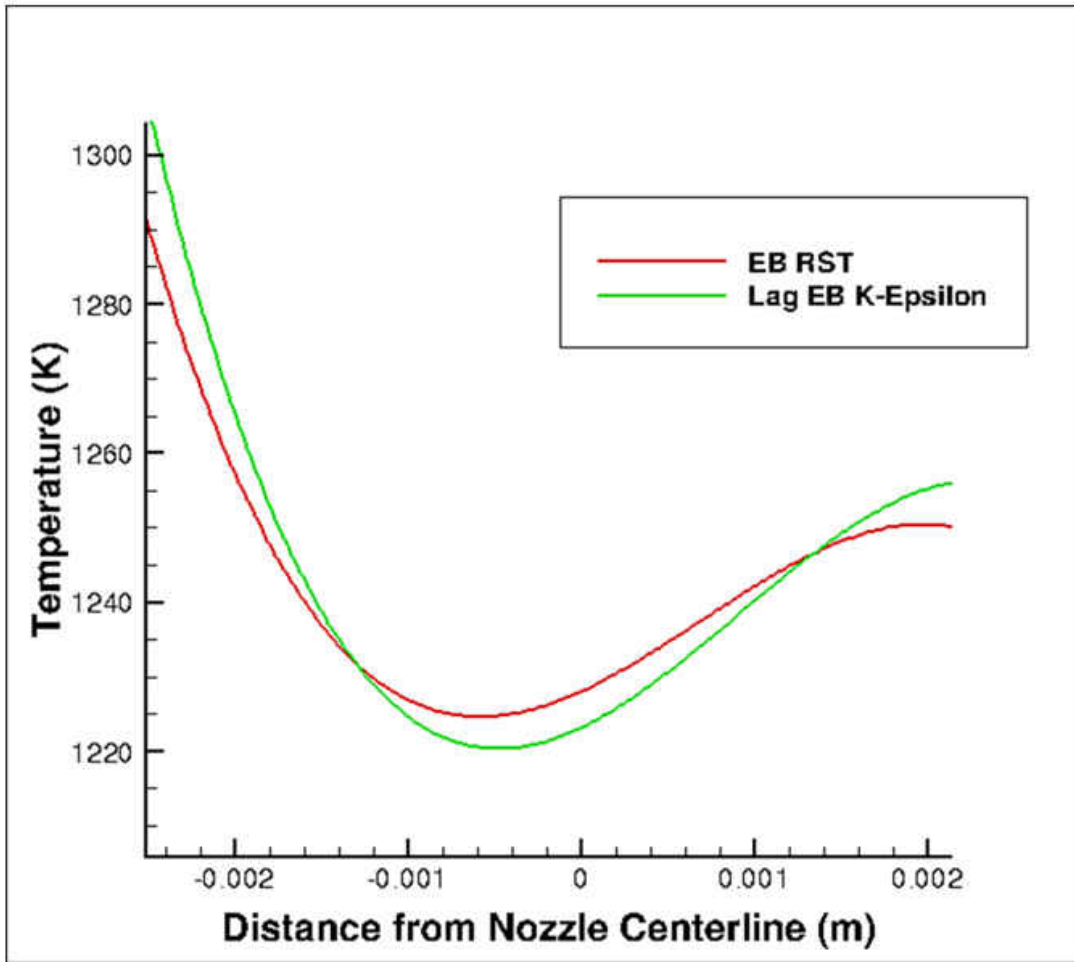

Figure 84: Nonrotating SH Hole Impingement Wall Y+ (EB RST)

External Blade Temperature

The external blade temperature profile for the nonrotating shower head hole model is illustrated in Figure 85. The temperature profiles are in good agreement with one another, illustrating similar trends. The minimum temperature, for both turbulence models, is towards the suction side, which corresponds to the maximum Nusselt Number towards the suction side on the impingement surface.

The Lag EB K-Epsilon model has a slightly lower minimum temperature, which is in agreement with the Lag EB K-Epsilon model having a higher Nusselt Number. Optimal values of Wall Y+ were maintained for shower head hole surfaces, Figures 86 and 87, and external blade surfaces, Figures 88 and 89.

Figure 85: Nonrotating SH Hole External Blade Temperature Profile
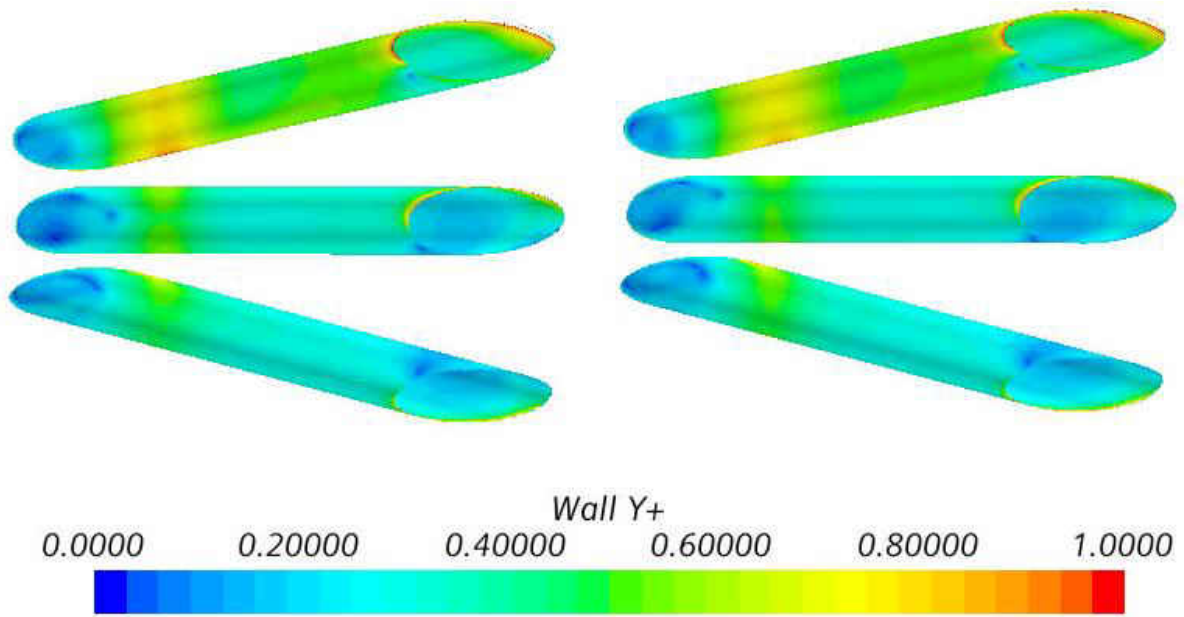
Figure 86: Nonrotating Shower Head Hole Wall Y+ (Lag EB K-Epsilon)
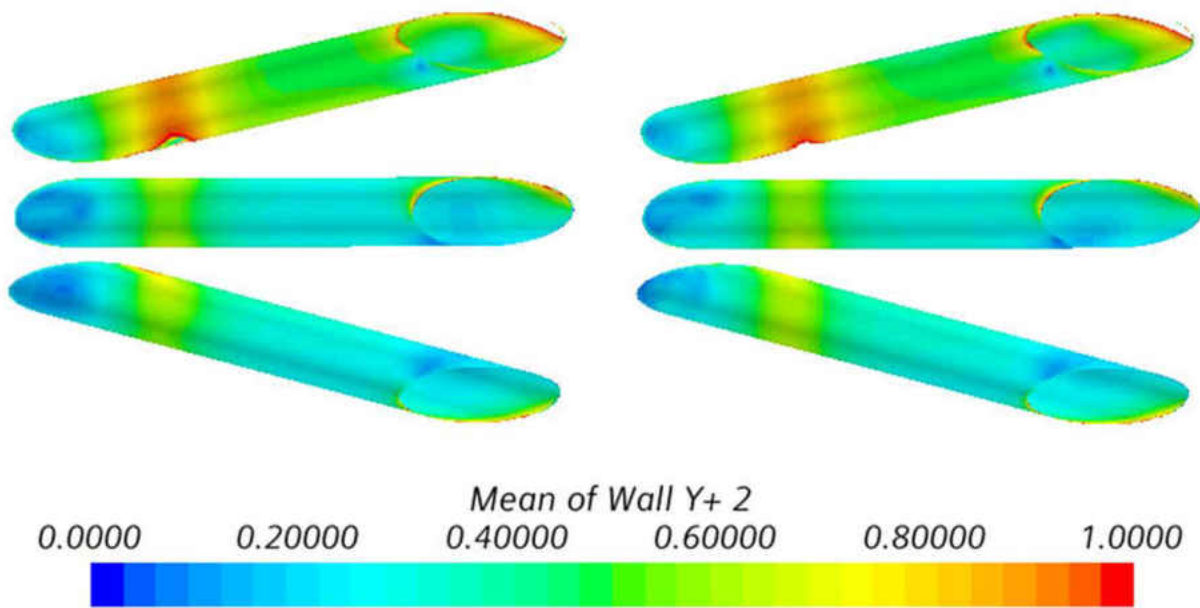
Figure 87: Nonrotating Shower Head Hole Wall Y+ (EB RST)

Wall Y+

| 0.0000 | 0.16819 | 0.33639 | 0.50458 | 0.67277 | 0.84097 |
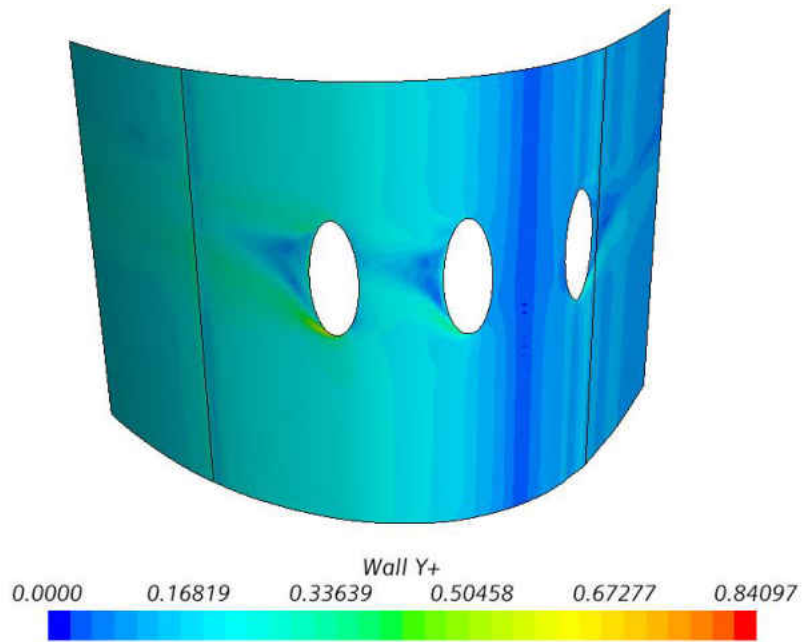
Figure 88: Nonrotating SH Hole External Blade Surface Wall Y+ (Lag EB K-Epsilon)

Mean of Wall Y+ 3

| 0.0000 | 0.20000 | 0.40000 | 0.60000 | 0.80000 | 1.0000 |

Figure 89: Nonrotating SH Hole External Blade Surface Wall Y+ (EB RST)

Rotating with Shower Head Holes

Flow Field Analysis: Velocity

The domain velocity flow field for the rotating shower head holes model is illustrated in Figures 90 and 91. No significant differences are observed between the turbulence models, besides the magnitude in wall jet velocities. The wall jet velocity for the Lag EB K-Epsilon model is considerably less than that of the EB RST model. The wall jet velocities for both turbulence models are noticeably less in comparison to the nonrotating shower head hole case studies.

The jet velocity flow fields are illustrated in Figures 92 and 93 and potential core velocity profiles are shown in Figures 94 and 95. The potential core velocity profiles show similar trends for both turbulence models. Both models illustrate a uniform profile at nozzle exit which gradually becomes parabolic with a decrease in magnitude. The degree of parabolicity and decrease in magnitude is more significant for the Lag EB K-Epsilon model than for the EB RST model.

Figure 90: Rotating SH Hole Domain Flow Field (Lag EB K-Epsilon)

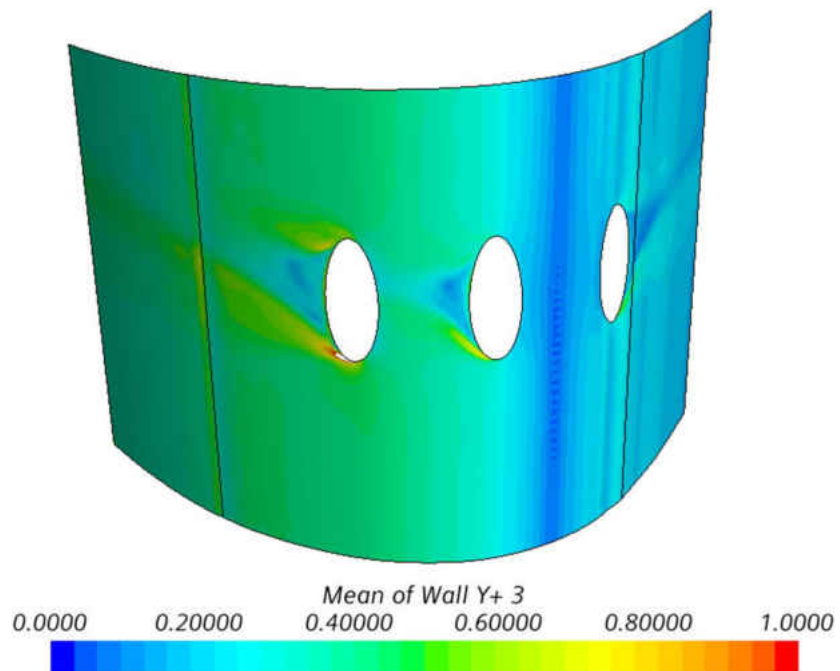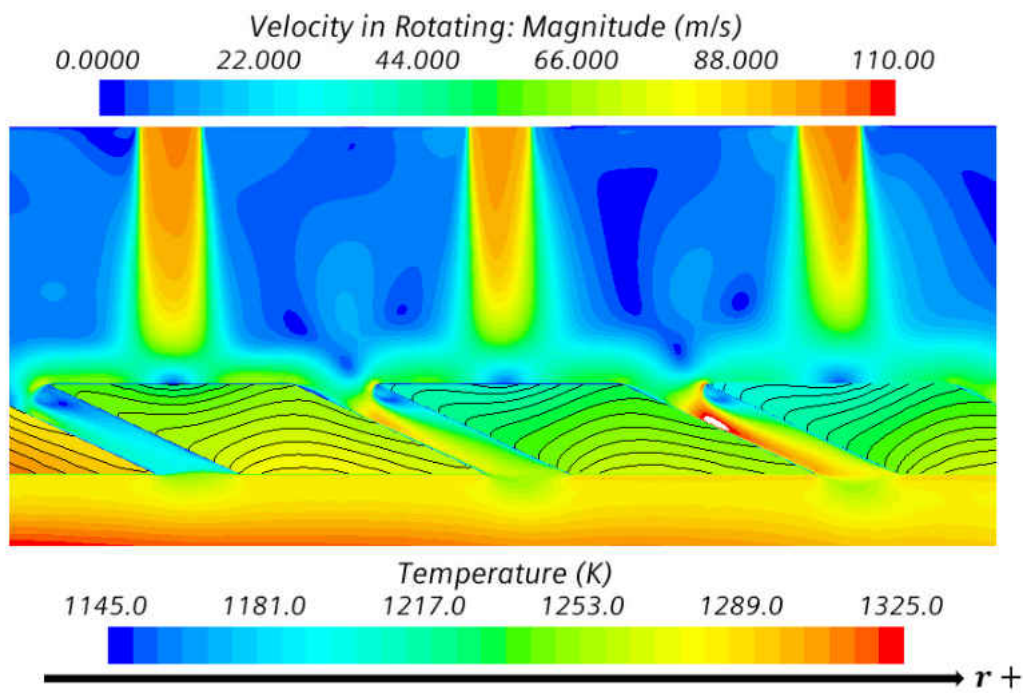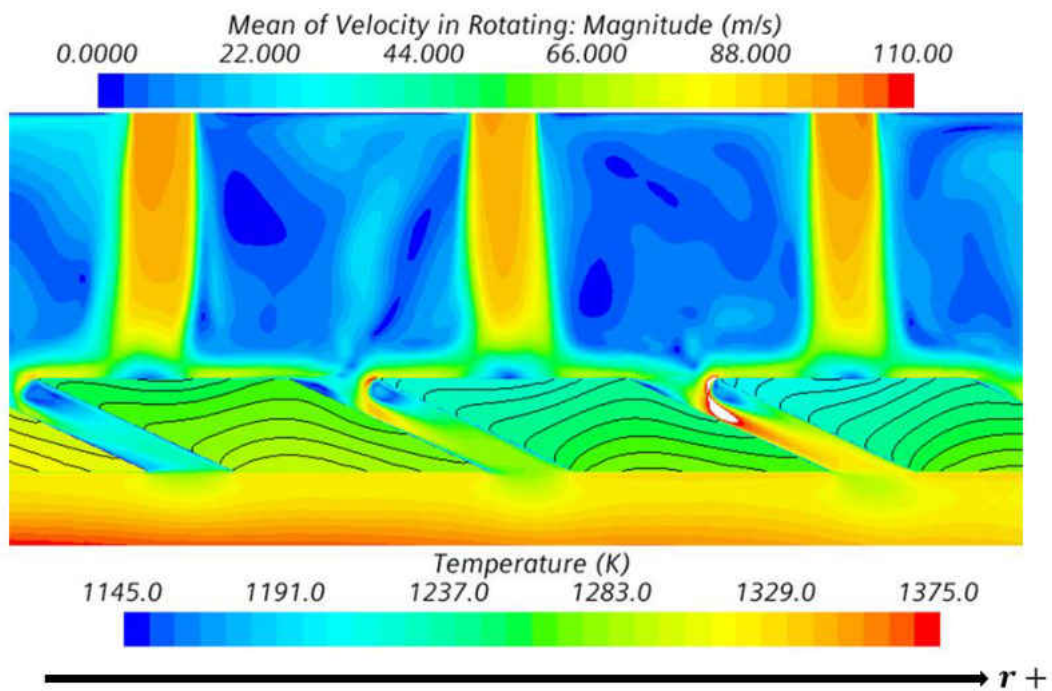*Figure 91: Rotating SH Hole Domain Flow Field (EB RST)*
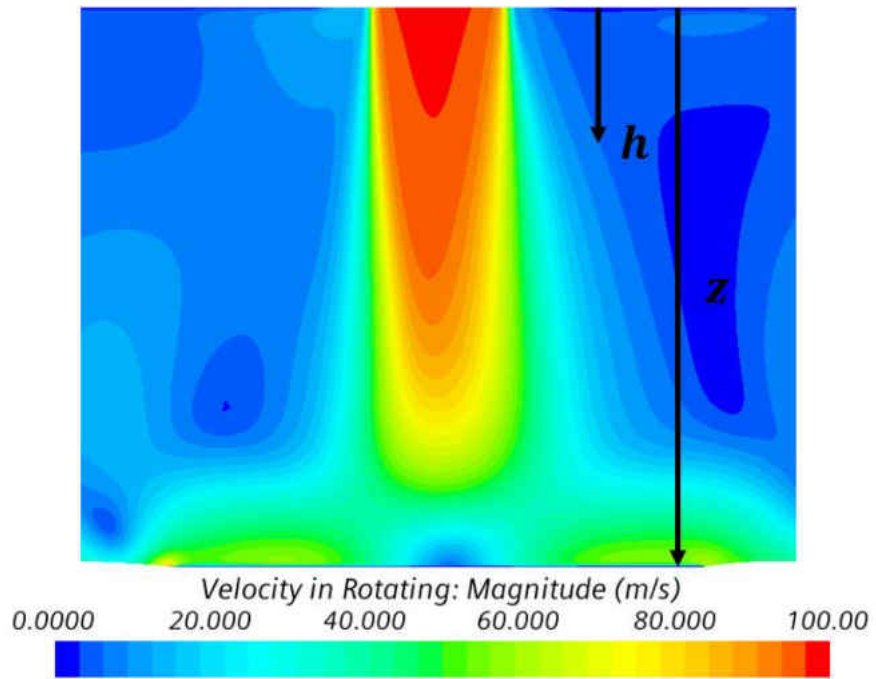
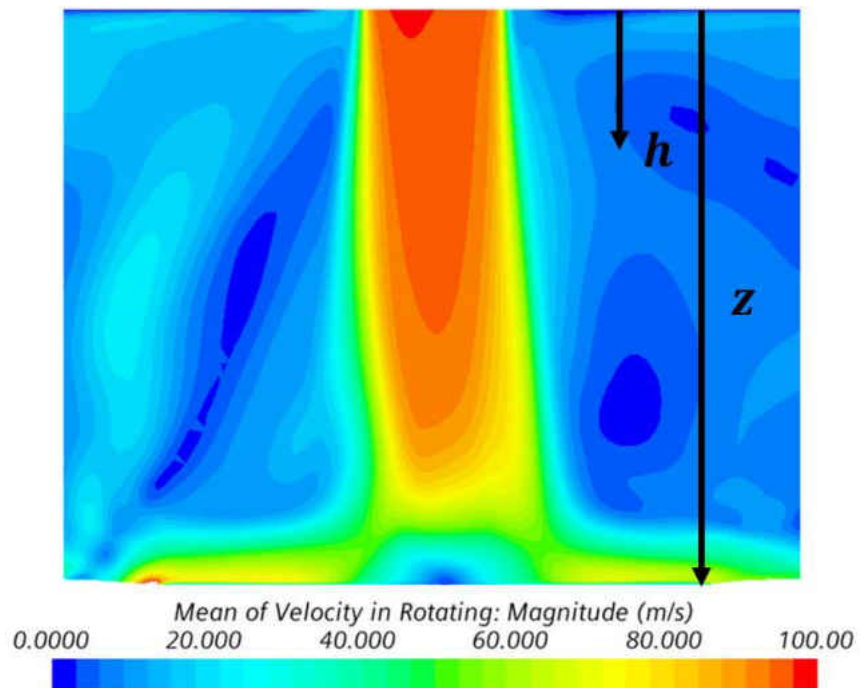*Figure 92: Rotating SH Hole Jet Flow Field (Lag EB K-Epsilon)*

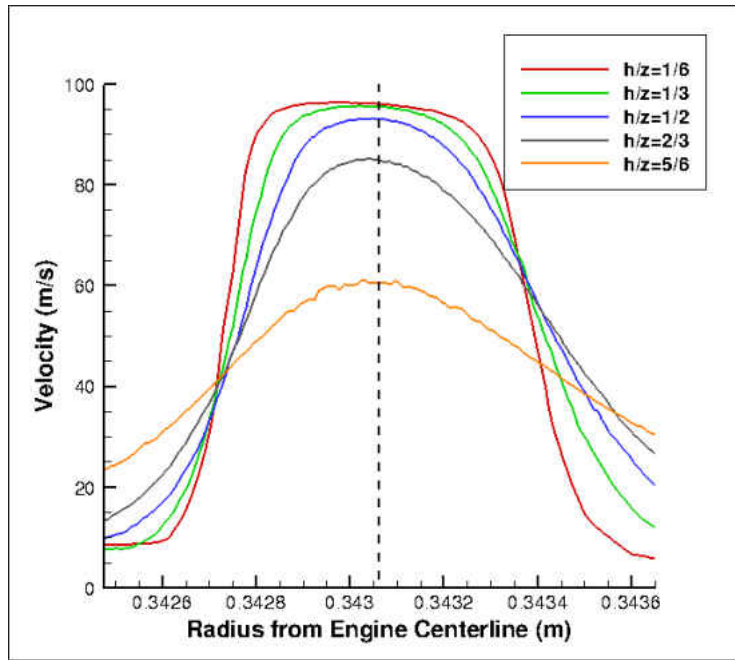*Figure 93: Rotating SH Hole Jet Flow Field (EB RST)*

Figure 94: Rotating SH Hole Potential Core Velocity Profiles (Lag EB K-Epsilon)
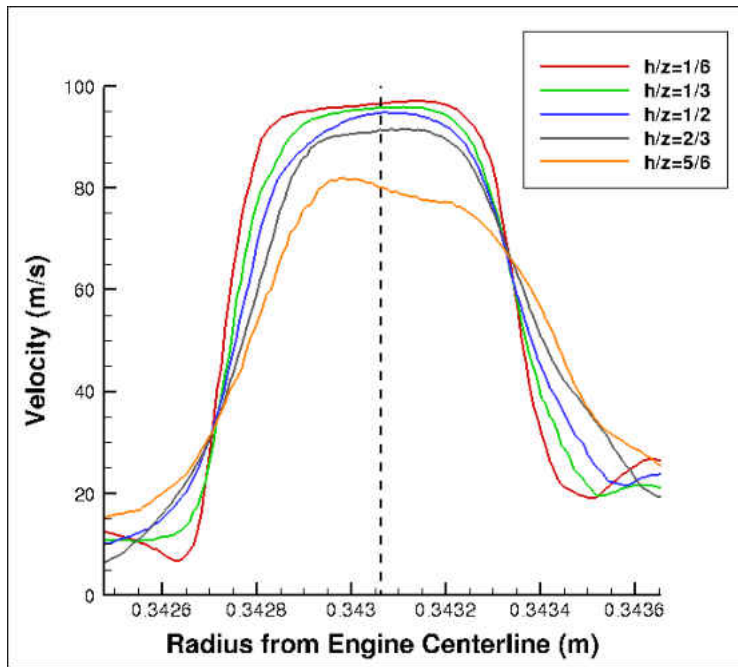

Figure 95: Rotating SH Hole Potential Core Velocity Profiles (EB RST)

Flow Field Analysis: Turbulent Kinetic Energy

The free jet TKE flow field is illustrated in Figures 96 and 97. The Lag EB K-Epsilon model shows maximum TKE at the stagnation region. While the EB RST model shows a stagnation region with high TKE, its maximum is at the shear layer close to the nozzle exit. The differences in location of maximum TKE can be explained by the application of the vorticity tensor within the transport equations for each model. For the Lag EB K-Epsilon model the vorticity tensor is applied in the f_w term of the reduced stress transport equation. Therefore as $\alpha \longrightarrow 0$, at the wall, the f_w term will be dominant. Which results in the effects of rotation being more significant at the wall. For the EB RST model the vorticity tensor is applied to the ϕ_{ij}^h term in the Reynolds Stresses transport equations. Therefore as $\alpha \longrightarrow 1$ the $\phi_{ij}^h - \varepsilon_{ij}^h$ will be dominant. This results in the effects of rotation being more significant away from the wall.

The TKE profile plot for the rotating shower head holes model is illustrated in Figures 98 and 99. Both turbulence models show potential cores with TKE. This implies that the rotational forces, which act perpendicular to the pressure force driving the jet, cause rotation of the fluid elements and thus increasing TKE within the potential core of the jet. The difference in magnitudes of TKE for the free jet region is due to the expected underprediction in turbulent dissipation for the Lag EB K-Epsilon model, thus resulting in overprediction of TKE, in comparison to the EB RST model. The EB RST model shows maximum TKE of the potential core at the nozzle exit and a reduction in TKE as the jet approaches the wall. The Lag EB K-Epsilon model illustrates just the opposite. This behavior can also be explained by the application of the vorticity tensor

within each models' transport equations. For the EB RST model the effects of rotation will be more significant away from the wall and vice versa for the Lag EB K-Epsilon model.
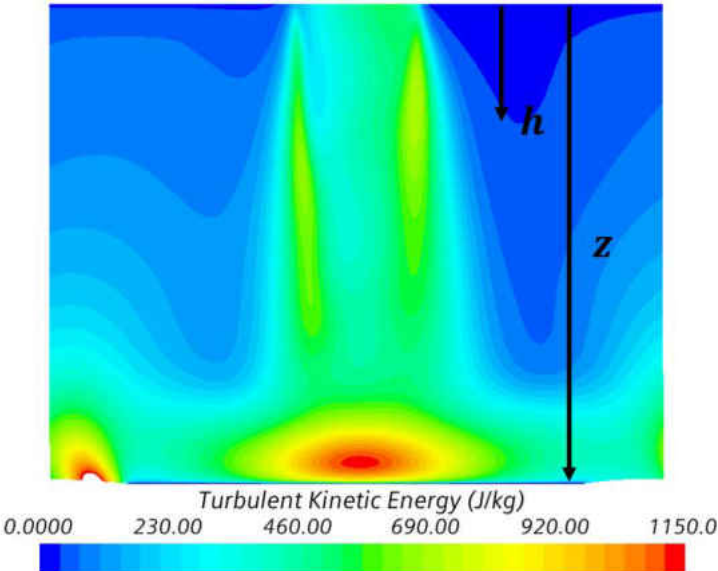

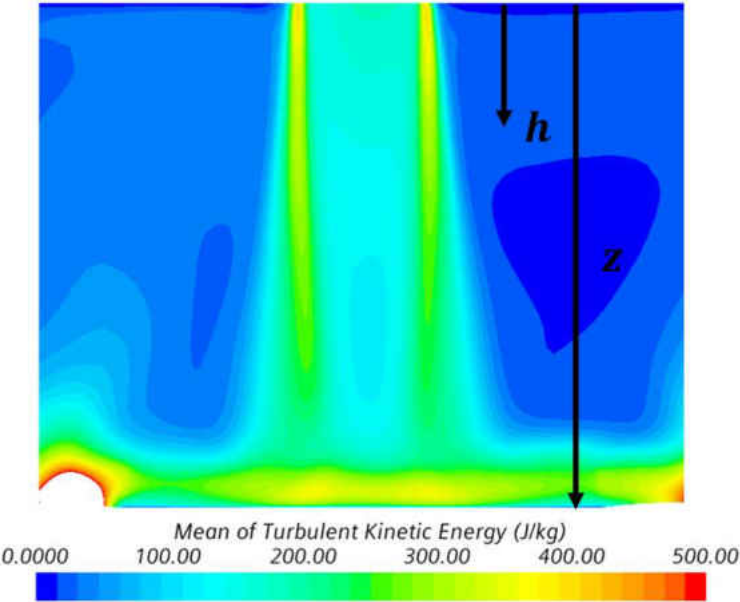*Figure 96: Rotating SH Hole Jet TKE Flow Field (Lag Eb K-Epsilon)*
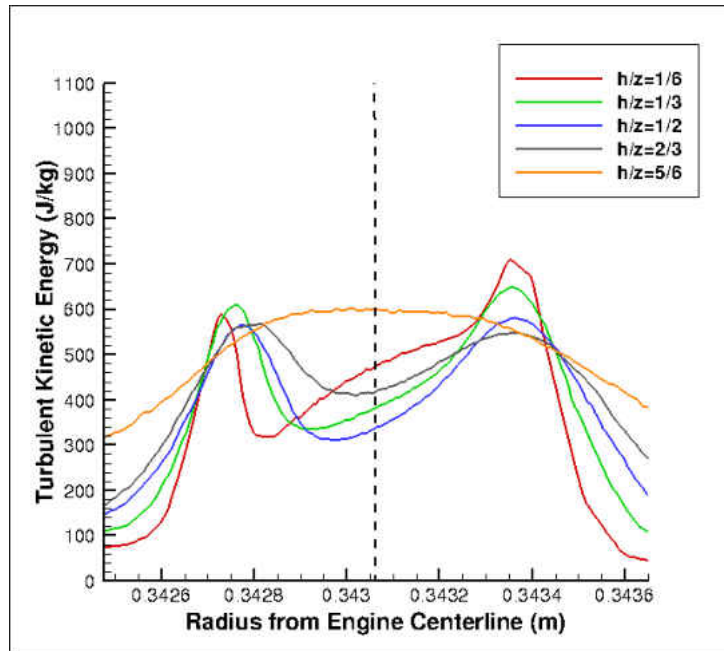

Figure 97: Rotating SH Hole Jet TKE Flow Field (EB RST)

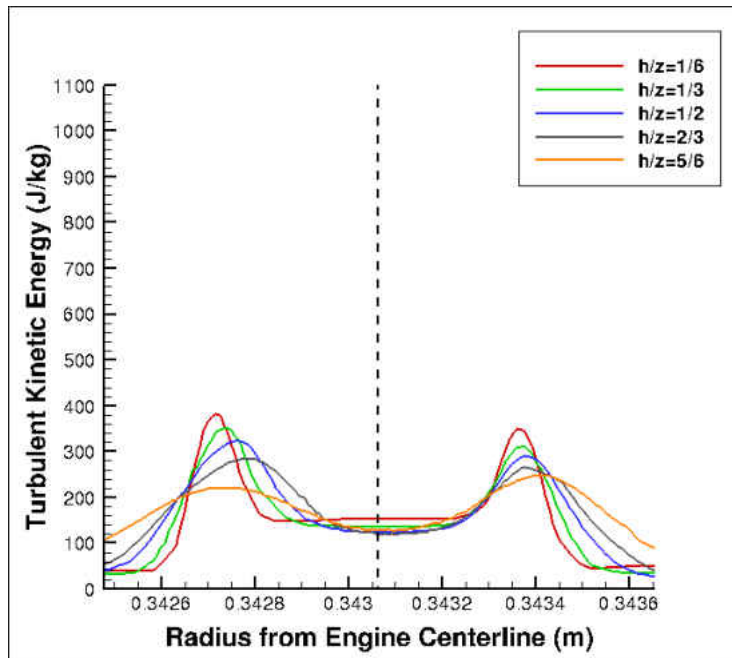*Figure 98: Rotating SH Hole Jet TKE Profiles (Lag EB K-Epsilon)*

Figure 99: Rotating SH Hole Jet TKE Profiles (EB RST)

Heat Transfer Analysis: Nusselt Number

Nusselt Number contour plots, for the rotating shower head holes model, are illustrated in Figures 100 and 101. The magnitudes of maximum Nusselt Number is considerably less, due to the reduction in incoming jet velocity. The location of maximum Nusselt Number is in line with the nozzle centerline, in comparison to the nonrotating case studies, which illustrated maximum Nusselt Number towards the suction side of the impingement surface. A possible explanation for this behavior is that rotational forces cause an increase in TKE within the potential core, in return reducing incoming jet velocity and hence reducing wall jet velocity. The reduced wall jet velocity results in an increase in pressure, thus reducing the larger pressure gradient in the suction side shower head holes.

The spanwise Nusselt Number distribution is shown in Figure 102. The Nusselt Number distributions, for both turbulence models, are in fair agreement with one another. The main difference being the magnitude of maximum Nusselt Number. The Lag EB K-Epsilon model shows a higher maximum Nusselt Number. The disagreement in magnitude of maximum Nusselt Number, between the two turbulence models, is assumed to be due to the method of diffusion. The EB RST model uses the Generalized Gradient Diffusion Hypothesis. Since the potential core velocity profiles and magnitudes were almost identical, for both turbulence models, it is assumed that the discrepancy lies with the method of diffusion. Wall Y+ values were optimal for impingement surfaces, Figures 103 and 104.
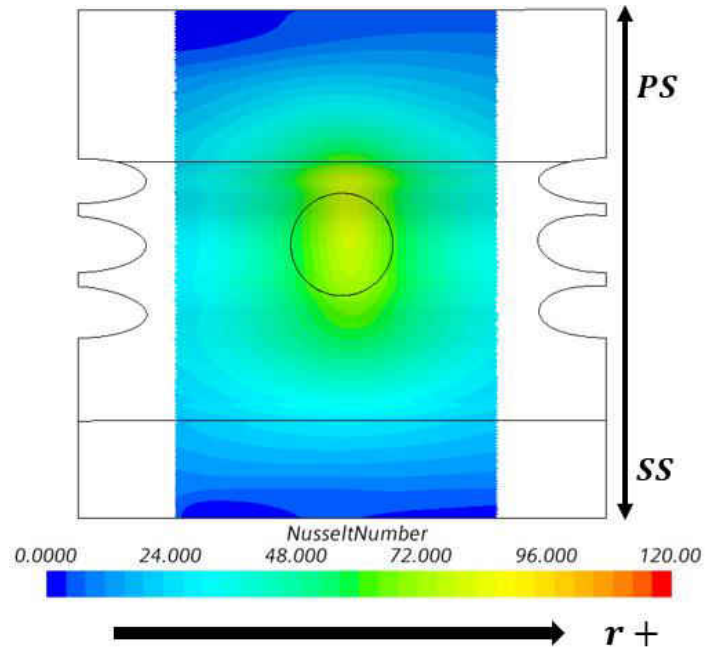
Figure 100: Rotating SH Hole Nusselt Number (Lag Eb K-Epsilon)
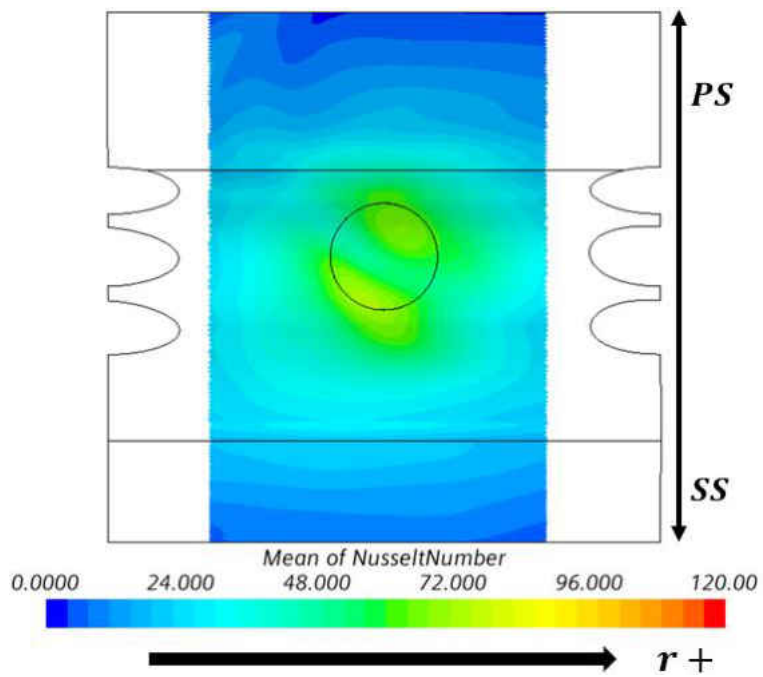
Figure 101: Rotating SH Hole Nusselt Number (EB RST)
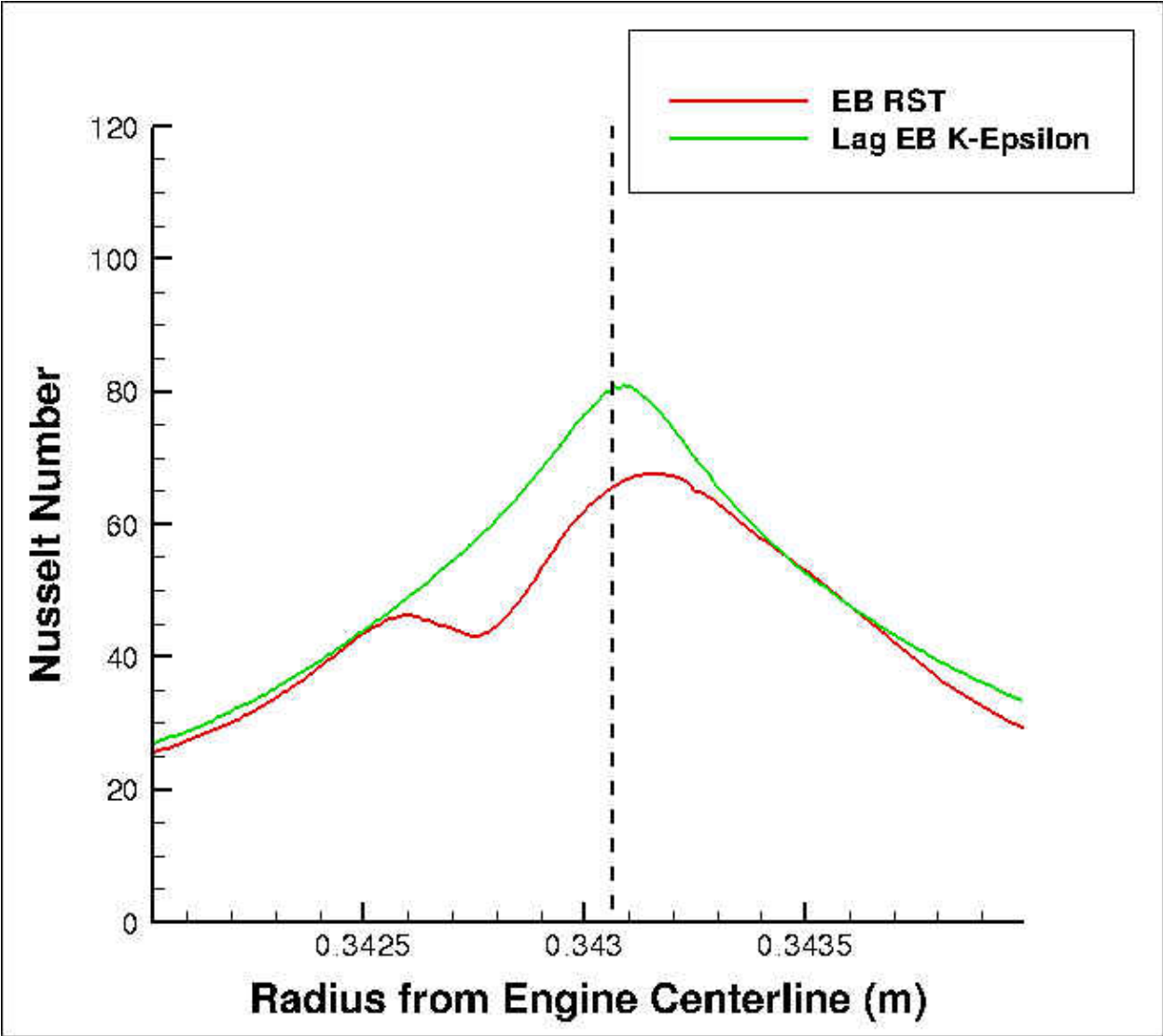
Figure 102: Rotating SH Hole Spanwise Nusselt Distribution
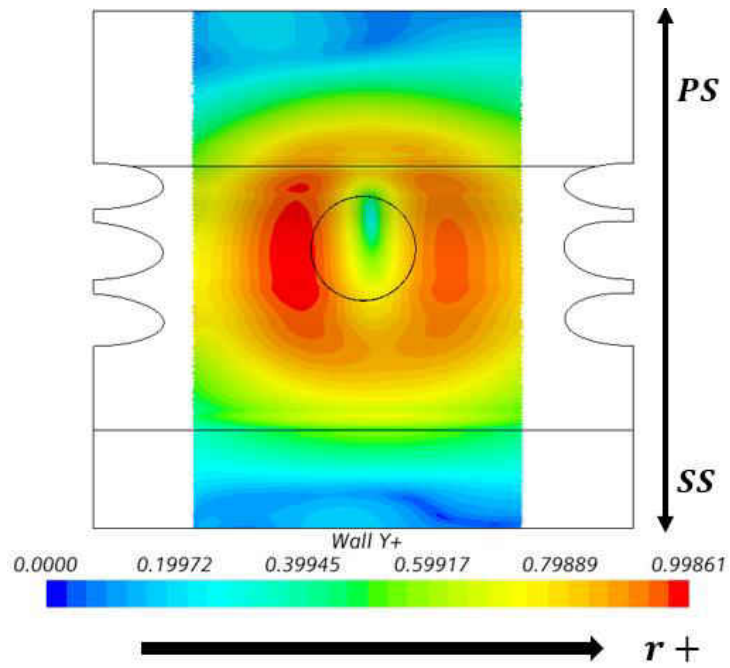
Figure 103: Rotating SH Hole Impingement Wall Y+ (Lag EB K-Epsilon)
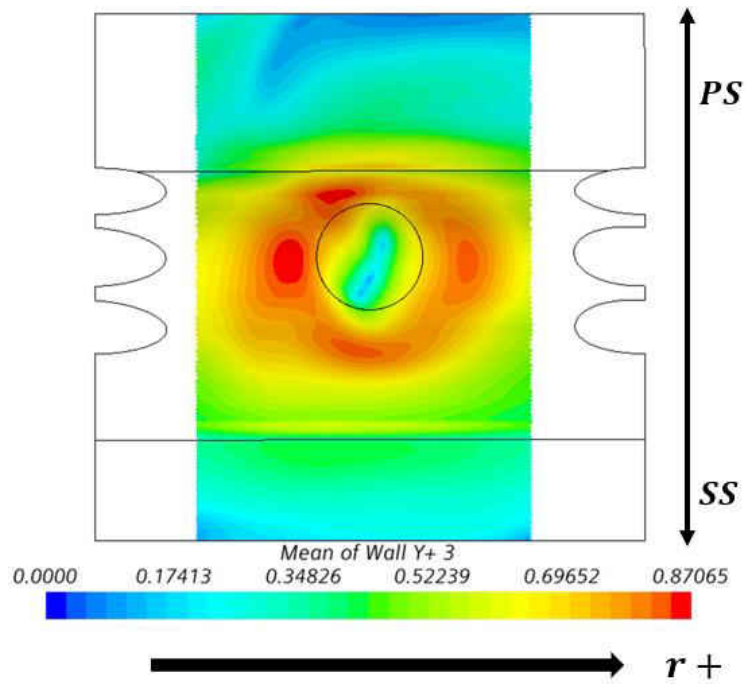
Figure 104: Rotating SH Hole Impingement Wall Y+ (EB RST)

External Blade Temperature

The external blade temperature profiles plot is shown in Figure 105. The temperature profiles are in good agreement with one another, with respect to trend. The Lag EB K-Epsilon profile shows approximately a $10°$ cooler temperature for most of the external blade surface. The Wall Y+ for shower head hole surfaces, Figures 106 and 107, and external blade surfaces, Figures 108 and 109, where maintained within optimal values.
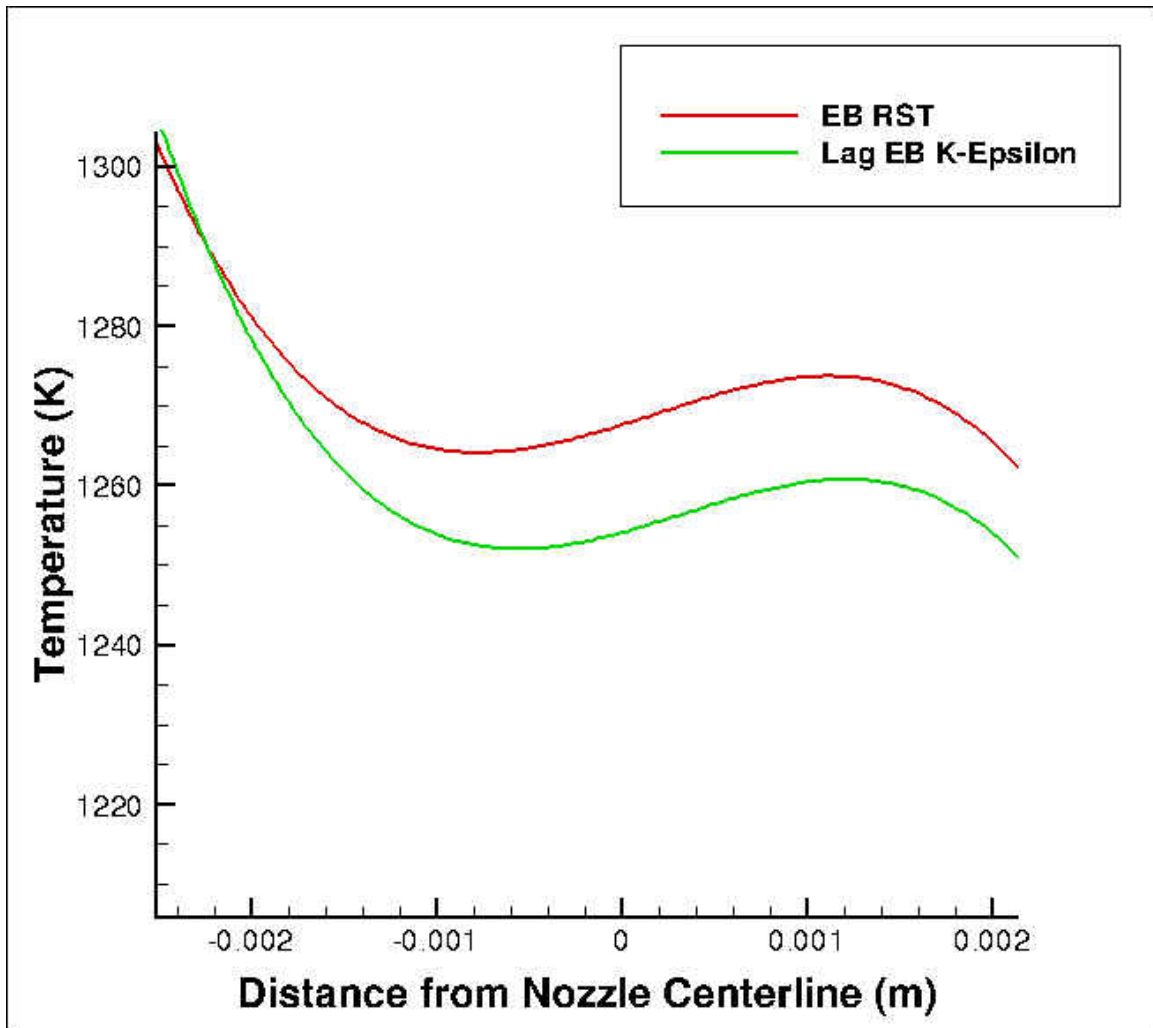
Figure 105: Rotating SH Hole External Blade Temperature Profile
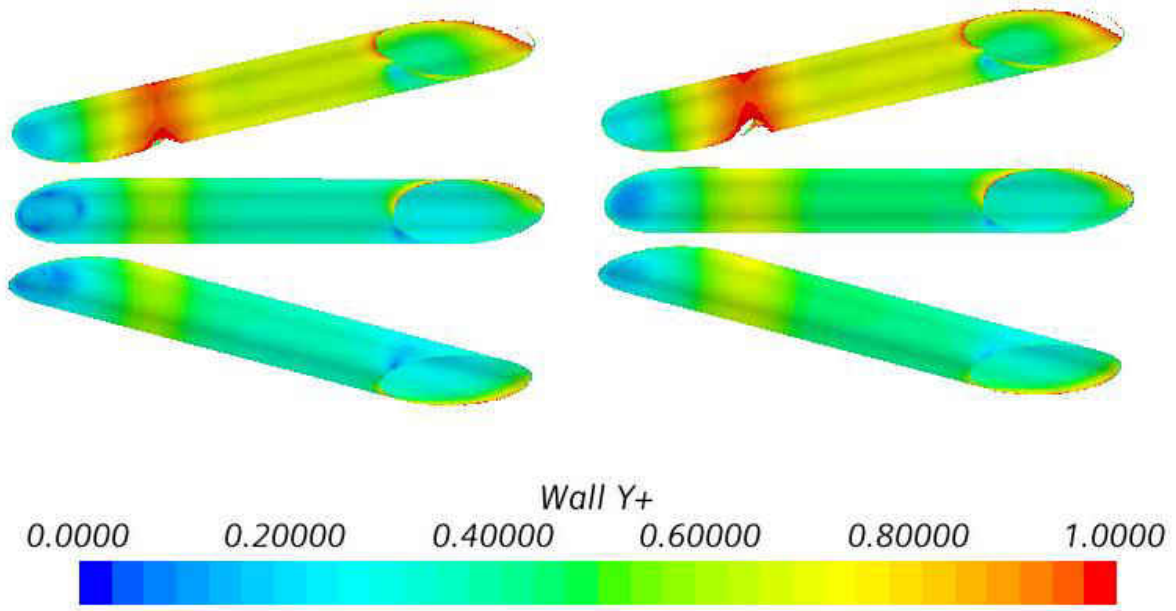
Figure 106: Rotating SH Hole Wall Y+ (Lag EB K-Epsilon)
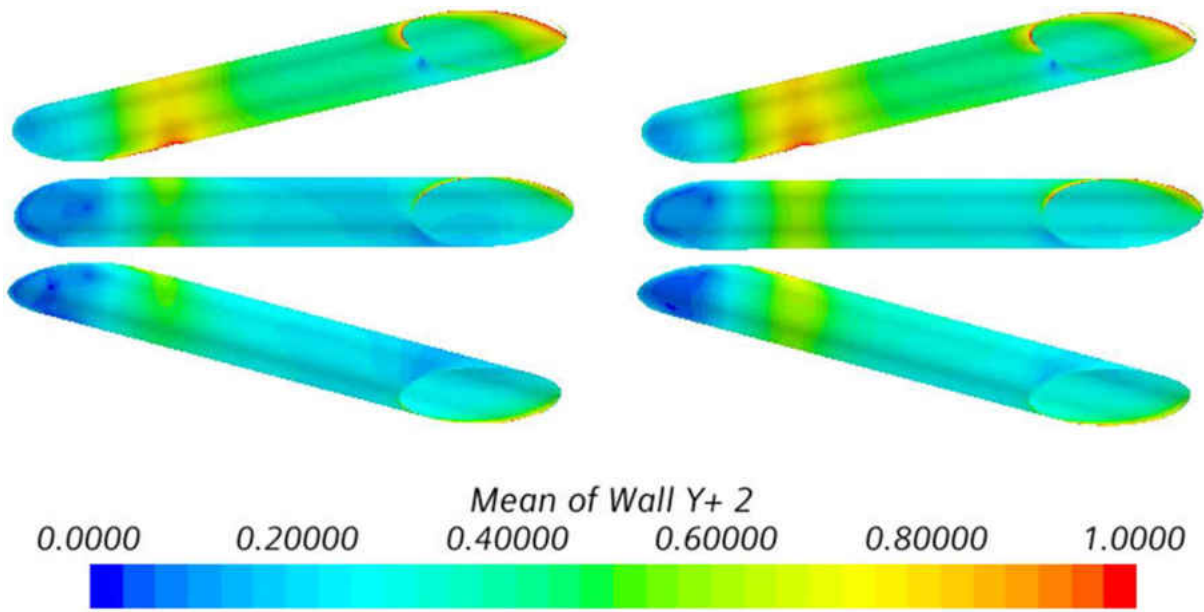
Figure 107: Rotating SH Hole Wall Y+ (EB RST)

Wall Y+

0.0000   0.16749   0.33498   0.50247   0.66996   0.83745
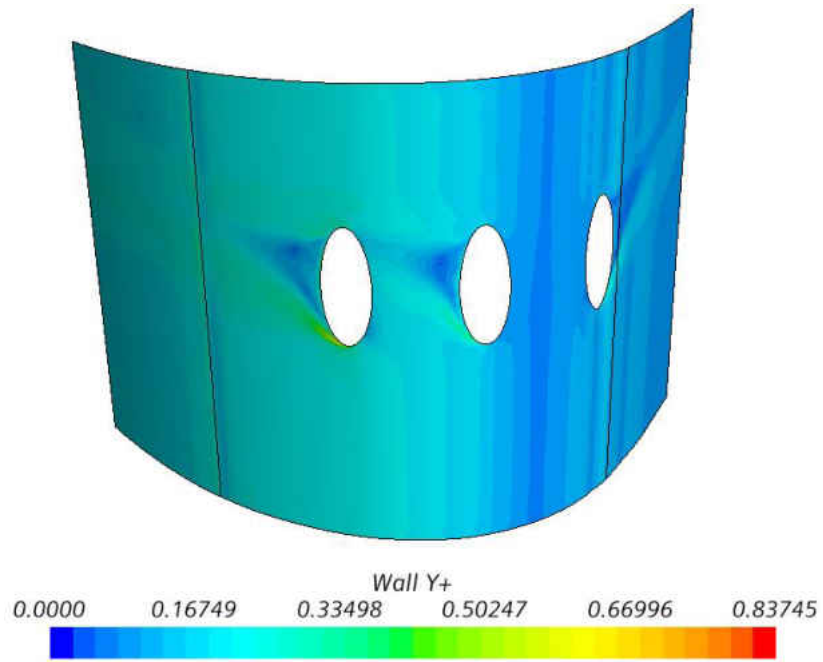
Figure 108: Rotating SH Hole External Blade Surface Wall Y+ (Lag EB K-Epsilon)

Mean of Wall Y+

0.0000   0.20000   0.40000   0.60000   0.80000   1.0000

Figure 109: Rotating SH Hole External Blade Surface Wall Y+ (EB RST)

105

CHAPTER – 5: CONCLUSION

Results from the study show, for both turbulence models, that rotational forces cause a production of TKE within the potential core of the jet. Which in return influences the potential core velocity profile to become parabolic and hence reducing incoming jet velocity. This results in a decrease in impingement effectiveness.

Resemblances in the turbulence models used consist of potential core velocity profiles, turbulent kinetic energy profile trends for nonrotating cases, Nusselt Number spanwise distribution trends and external blade temperature profiles (excluding the rotating no shower head hole case). Discrepancies in the turbulence models used consist of magnitude of turbulent kinetic energy, location of maximum turbulent kinetic energy for rotating cases, turbulent kinetic energy profile trends for rotating cases, location of maximum Nusselt Number and the external blade temperature profile for the rotating no shower head hole case.

The difference in magnitude of turbulent kinetic energy, between the two turbulence models, can be explained by the expected underpredic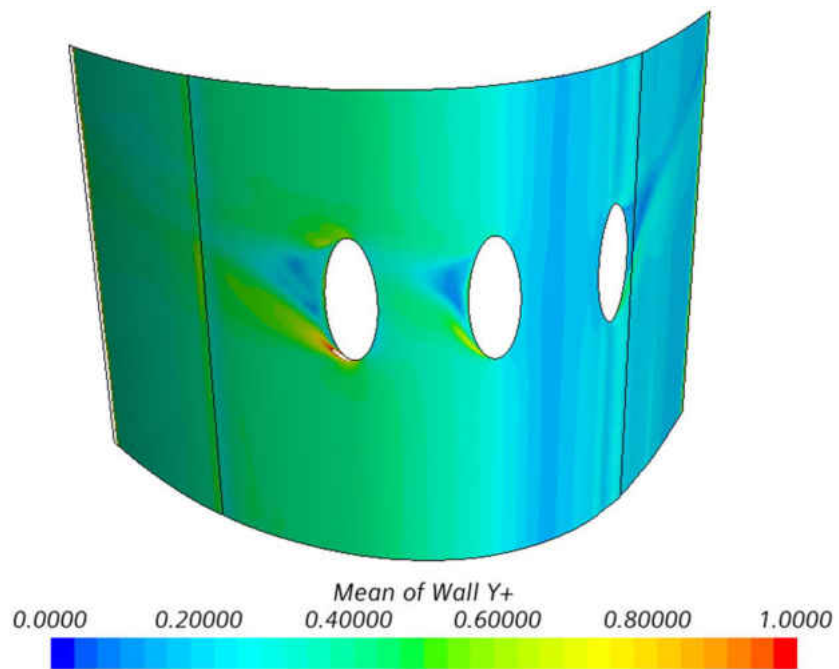tion of turbulent dissipation rate for the Lag EB K-Epsilon model, with respect to the EB RST model. Another explanation for this behavior is that the vorticity tensor for the Lag EB K-Epsilon model has an additional term, the $Spalart -$ $Shur$ tensor, which has a dependency through the reduced stress transport equation with the turbulent kinetic energy. The variance in location of maximum Nusselt Number is assumed to be due to the application of the Generalized Gradient Diffusion Hypothesis for the EB RST model. The inconsistencies in location of maximum turbulent kinetic energy and turbulent kinetic energy

profile trends for the rotating case studies is due to the location of application of the vorticity

tensor, which is a function of the rotational speed of the reference frame. For the Lag EB K-

Epsilon model the vorticity tensor is applied to the f_w term which results in the effects of

rotation being more significant near the wall. The EB RST model applies its corresponding

vorticity tensor in the ϕ_{ij}^h which results in the effects of rotation being more significant away

from the wall.

In general, both turbulence models produced almost identical results regarding profile

trends, apart from the external blade temperature profile for the rotating no shower head hole

case. The maximum external blade temperatures, excluding the rotating no shower head hole

case, had a maximum deviation of approximately 0.8% with an average deviation of

approximately 0.4%.

In consideration to number of iterations required to reach converged solution, time

required to perform each iteration, stability of solution and sensitivity to mesh quality the Lag EB

K-Epsilon turbulence model is the obvious model of choice for industrial applications. The Lag EB

K-Epsilon model reached converged solutions in a fifth of the amount of iterations required by

the EB RST model. The time required to perform each iteration was considerably less for the

three-transport equation model in comparison to the seven-transport equation one. The EB RST

model solution oscillated about a mean value, which required iteration averaging of probe

monitors to find the and match mean values within the flow fields. While the Lag EB K-Epsilon

model had little to no oscillations in its solution. The cell quality of the EB RST model required

eight optimization cycles with a cell quality threshold of 1.0 to obtain converged solutions. The

Lag EB K-Epsilon model achieved converged solutions with only one optimization cycle with a cell

quality threshold of 1.0.

REFERENCES

[1] Goldstein, R. J., Behbahani, A. I. & Kieger Heppelmann, K., Streamwise distribution of the recovery factor and the local heat transfer coefficient to an impinging circular air jet*, Int. J. Heat and Mass Transfer,* Vol. 29, No. 8, pp. 1227-1235, (1986)

[2] Florschuetz, L., Truman, C. & Metzger, D., Streamwise flow and heat transfer distributions for jet array impingement with crossflow. *ASME Journal of Heat Transfer,* Vol. 103, pp. 337-342, (1981)

[3] Lamont, J. A., Ekkad, S. V. & Alvin, M. A., Effects of rotation on heat transfer for a single row jet impingement array with crossflow. *ASME Journal of Heat Transfer,* Vol. 134, 082202, (2012)

[4] Iacovides, H., Kounadis, D., Launder, B. E., Li, J. & Xu, Z., Experimental study of the flow and thermal development of a row of cooling jets impinging on a rotating concave surface. *ASME Journal of Heat Transfer,* Vol. 127, pp. 222-229, (2005)

[5] Chiang, H. W. & Li, H. L., Jet impingement and forced convection cooling experimental study in rotating turbine blades. *ASME Turbo Expo 2009: Power for Land, Sea, and Air,* Vol. 3, pp. 679-689, (2010)

[6] Mattern, C. & Hennecke, D. K., The influence of rotation on impingement cooling. *ASME Turbo Expo Conference* Paper 96-GT-161, (1996)

[7] Gau, C. & Lee, C. C., Impingement cooling flow structure and heat transfer along rib-roughened walls. *Int. J. of Heat and Mass Transfer,* 35(11), pp. 3009-3020, (1992)

[8] Yang, L., Kan, R., Ren, J. & Jiang, H., Effect of film cooling arrangement on impingement heat transfer on turbine blade leading edge. *ASME Turbo Expo 2013: Turbine Technical Conference and Expositioin,* Vol. 3A, GT2013-95261, (2013)

[9] Taslim, M. E., Khanicheh, A., Experimental and numerical study of impingement on an airfoil leading edge with and without showerhead and gill film holes. *ASME Journal of Turbomachinery,* Vol. 128, pp. 310-320, (2006)

[10] Hussain, A.K.M.F., Coherence structure and turbulence. *Journal of Fluid Mechanics*, Vol. 173, pp. 303-356, (1986)

[11] Winant, C.D. & Browand, F.K., Vortex pairing: the mechanism of turbulent mixing layer growth at moderate Reynolds number, Vol. 63, pp. 237-255, (1974)

[12] Billard, F. and Laurence, D., A robust $k - \varepsilon - v^2/k$ elliptic blending turbulence model applied to near wall, separated and buoyant flows. *International Journal of Heat and Fluid Flow,* Vol 33 (1), pp. 45-58, (2012)

[13] Revell, A.J., Benhamadouche, S., Craft, T., Laurence, D., A stress-strain lag eddy viscosity model for unsteady mean flow, *International Journal of Heat and Fluid Flow,* Vol 27 (5), pp. 821-830 (2006)

[14] Lardeau, S., Billard, F. Development of an elliptic-blending lag model for industrial applications. *54th AIAA Aerospace Sciences Meeting,* p. 1600, (2016)

[15] Lardeau, S. and Manceau, R. Computations of complex flow configurations using a modified elliptic-blending Reynolds-Stress Model. *Proc. Of the 10th Eng. Turb. Modelling and Measurement Conf., Marbella, Spain*, (2014)

[16] Daly, B.J. and Harlow, F.H., Transport equations of turbulence. *Physics of Fluids,* Vol. 13, pp. 2634-2649, (1970)

[17] Timko, L.P., Energy efficient engine – High pressure turbine component test performance report. *National Aeronautics and Space Administration,* NASA CR-168289

[18] Halila, E. E., Lenahan, D. T. & Thomas, T.T., Energy efficient engine – High pressure turbine test hardware detailed design report. *National Aeronautics and Space Administration,* NASA CR-167955

[19] Celik, I. B., Ghia, U., Roache, P. J., Freitas, C. J., Coleman, H., Radd, P. E., Procedure for Estimation and Reporting of Uncertainty Due to Discretization in CFD Applications. *ASME Journal of Fluids Engineering*, Vol. 130, 078001, (2008)